



ADVANCES IN ENHANCED MULTI-PLANE 3D
IMAGING AND IMAGE SCANNING MICROSCOPY

SOHEIL MOJIRI

ADVANCES IN ENHANCED MULTI-PLANE 3D
IMAGING AND IMAGE SCANNING
MICROSCOPY

Dissertation

to acquire the doctoral degree in mathematics and natural science
“Doctor rerum naturalium”
at the Georg-August-Universität Göttingen

within the doctoral degree program

Physics of Biological and Complex Systems
of the Göttingen Graduate School of Neurosciences, Biophysics,
and Molecular Biosciences (GGNB)
of the Georg-August University School of Science (GAUSS)

submitted by

SOHEIL MOJIRI
from Isfahan, Iran
Göttingen, October 2020

THESIS COMMITTEE

Prof. Dr. Jörg Enderlein
Third Institute of Physics - Biophysics
Georg-August-University Göttingen

Prof. Dr. Fred S. Wouters
Institute for Neuropathology
University Medical Center Göttingen

Dr. Andreas Neef
Campus Institute for Dynamics of Biological Networks,
Georg-August University Göttingen

EXAMINATION BOARD

FIRST REFEREE: Prof. Dr. Jörg Enderlein
Third Institute of Physics - Biophysics
Georg-August-University Göttingen

SECOND REFEREE: Dr. Andreas Neef
Campus Institute for Dynamics of Biological Networks,
Georg-August University Göttingen

Prof. Dr. Fred S. Wouters
Institute for Neuropathology
University Medical Center Göttingen

OTHER MEMBERS OF THE EXAMINATION BOARD:

Prof. Dr. Holger Stark
Max Planck Institute for Biophysical Chemistry, department
Structural Dynamics
Göttingen

Prof. Dr. Timo Betz
Center for molecular biology of inflammation Westfälische
Wilhelms-Universität
Münster

Prof. Dr. Alexander Egner
Laser Laboratory
Göttingen

DATE OF ORAL EXAMINATION: 24.11.2020

"Why has not Man a microscopic eye?
For this plain reason, Man is not a Fly.
Say what the use, were finer optics given,
T'inspect a mite, not comprehend the heaven."

Alexander Pope , 1745

ABSTRACT

High-speed 3D optical microscopy is an indispensable requirement in studying rapid processes like signaling in neuronal networks, flagellar motion, or complex motion of living and highly dynamic sub-cellular components. However, the 3D imaging capability often compromises either the acquisition speed or the complexity of the imaging system. Multi-plane imaging offers a parallelized acquisition of several focal planes at the same time, which tremendously enhances the temporal resolution. Nonetheless, most of the current multi-plane approaches are complex and require several optical elements to create multiple beams with different optical path lengths, limiting their broad application.

To address these problems, in this thesis, employing a multi-plane prism, we introduce three novel techniques that each improve the concept of rapid 3D optical microscopy in a different direction: First, we accomplish a multi-plane detection for a phase-contrast microscope resulting in a 3D, label-free and non-complex imaging system with a $\sim 4\text{ms}$ of temporal resolution. We applied this system in real-time studying isolated bare axonemes of *Chlamydomonas* beating in the vicinity of a surface. This enabled us to observe their non-zero torsional motion where the torsion sign slowly changes from negative at the basal end toward positive at the distal end of flagella.

Second, straightforwardly, we combine an experimental spectral un-mixing setup with the multi-plane detection and obtain an instant 3-color 3D microscope with a minimal axial color aberration of 140 nm in a $\sim 2.5\text{ }\mu\text{m}$ axial range. The performance of such a microscope is verified in volumetric imaging of three different subcellular components in fixed COS-7 cells.

Third, a single-color multi-plane fluorescence microscope has been employed as a rapid 3D particle tracking velocimetry method in micro-scale to study single particles tracing the so-called *Marangoni* flow. Using that, besides the velocity fields of single particles, we achieve a localization precision of $\sim 60\text{ nm}$ in the lateral and $\sim 300\text{ nm}$ in the axial direction over a $120 \times 120 \times 13\text{ }\mu\text{m}^3$ field of view. Altogether, using these three techniques, we extend the temporal resolution, throughput, and applicability of 3D optical microscopy.

In another project, we implemented image scanning microscopy simultaneously in two colors on a conventional wide-field microscope by applying an LED light source and a digital micro-mirror device. This permits us to realize an inexpensive, speckle noise-free, and easy-to-implement super-resolution add-on for a conventional epifluorescence microscope.

Keywords: Optical microscopy, 3D imaging, Multi-plane imaging, Phase-contrast microscopy, *Chlamydomonas* flagella, Spectral unmixing, Micro-scale particle imaging velocimetry, *Marangoni* flow, Image scanning microscopy.

AFFIDAVIT

Hereby, I declare that the presented thesis has been written independently and with no other sources and aids than quoted.

Parts of this thesis and some figures have been submitted and provided in the manuscripts listed below.

LIST OF RELATED PUBLICATIONS

Soheil Mojiri, Sebastian Isbaner, Steffen Mühle, Hongje Jang, Albert J. Bae, Ingo Gregor, Azam Gholami, and Jörg Enderlein. "Three-dimensional beating dynamics of *Chlamydomonas flagella*", bioRxiv (2020), DOI: (<https://doi.org/10.1101/2020.07.20.212159>).

Soheil Mojiri, Ingo Gregor, Eugenia Butkevich, and Jörg Enderlein. "Instant three-color multi-plane fluorescence imaging" (In preparation).

Göttingen, October 2020

To my parents Mohsen and Ezzat, and
my wife Samira

CONTENTS

Bibliography	i
1 INTRODUCTION	1
1.1 Structure of this thesis	4
2 FUNDAMENTALS AND GENERAL CONCEPTS	5
2.1 Optical microscopy	5
2.1.1 Axial magnification	7
2.1.2 Imaging resolution	8
2.1.3 Köhler illumination	9
2.2 Advanced transmitted optical microscopy	9
2.3 Fluorescence microscopy	14
2.3.1 Fluorescence	15
2.3.2 Epi-fluorescence and confocal laser scanning microscopy	17
2.4 Multi-plane imaging	20
2.4.1 Multi-plane imaging approaches	24
2.5 Super resolution microscopy	27
2.5.1 Principles of optics-based SRM	28
2.5.2 Image Scanning microscopy	29
3 MULTI-PLANE 3D MICROSCOPY	33
3.1 Characterization and alignment for a multi-plane prism	34
3.2 Observation of beating <i>Chlamydomonas</i> flagella with multi-plane phase-contrast imaging	41
3.2.1 Introduction	42
3.2.2 Methods	46
3.2.3 Results	57
3.2.4 Conclusion and Discussion	64
3.3 3D μ -particle tracking velocimetry (μ -PTV)	68
3.3.1 Introduction	68
3.3.2 Methods	70
3.3.3 Results	75
3.3.4 Discussion	79
3.4 3-color multi-plane microscopy	81
3.4.1 Introduction	81
3.4.2 Methods	82
3.4.3 Design of the spectral unmixing block	82
3.4.4 Results	90
3.4.5 Discussion	91
4 DUAL COLOR EPI-FLUORESCENCE LED IMAGE SCANNING MICROSCOPY	93

CONTENTS

4.1	Introduction	93
4.2	Methods	96
4.2.1	DMD-based incoherent ISM setup	96
4.2.2	Chromatic aberration check	97
4.2.3	Image acquisition	98
4.2.4	Image reconstruction	99
4.2.5	Preparation of fixed <i>vero</i> cells	100
4.3	Results	101
4.3.1	Example 1: fluorescent beads	101
4.3.2	Example 2: Argo SIM pattern 'E'	104
4.3.3	Example 3: fixed cells from the <i>vero</i> cell line	105
4.4	Conclusion	105
5	CONCLUSION	107
A	OTHER CONTRIBUTION	109
A.1	Axial drift correction using infra-red based focus stabilizer for MIET	109
A.1.1	Some points about running the Auto-focus system	111
A.2	dynaMIET	113
B	APPENDIX	115
B.1	Alignment of Köhler illumination	115
B.2	Specifications of multi-plane phase-contrast microscope components	116
B.3	Hardware configuration of multi-plane phase-contrast microscope	117
B.4	Specifications of 3-color multi-plane microscope components	117
B.5	LED-ISM setup specifications	119
	BIBLIOGRAPHY	121

LIST OF FIGURES

Figure 2.1	Principle of the earliest compound optical microscope	6	
Figure 2.2	axialMagnification	7	
Figure 2.3	Numerical aperture	8	
Figure 2.4	Illumination and detection of a wide-field optical microscope	10	
Figure 2.5	BrightField versus phase contrast microscopy		12
Figure 2.6	BrightField and phase contrast images of flagella	13	
Figure 2.7	DIC microscopy	15	
Figure 2.8	Fluorescence	16	
Figure 2.9	Epi-fluorescence versus confocal laser scanning microscope	18	
Figure 2.10	PSF and OTF of a wide-field and a confocal microscope	19	
Figure 2.11	Concept of bi-plane imaging	21	
Figure 2.12	Detection path of a typical multi-plane wide-field microscope	23	
Figure 2.13	Inter-plane distance versus objectiv's magnification	24	
Figure 2.14	Axial resolution versus objectiv's NA	25	
Figure 2.15	Multi-plane imaging with different approaches		26
Figure 2.16	Resolution improvement obtained by scanning sample via structured excitation patterns	28	
Figure 2.17	ISM working principle	30	
Figure 2.18	OTF comparison of wide-field and wide-field based ISM	31	
Figure 3.1	Multi-plane prism design	35	
Figure 3.2	Tube lens focal plane of a IX71 microscope		38
Figure 3.3	Adjustment of realy lenses	39	
Figure 3.4	Adjustment of the multi-plane prism	39	
Figure 3.5	Alignment of the field aperture	40	
Figure 3.6	Grid array for alignment	40	
Figure 3.7	Axonemal inner structure	42	
Figure 3.8	DIC images of uni-flagellate sperm cells of several species with the same magnification	43	
Figure 3.9	<i>Chlamydomonas</i>	44	
Figure 3.10	Schematic of the multi-plane phase-contrast microscope	47	
Figure 3.11	Inter-plane distance and brightness calibration		48
Figure 3.12	Relative shift of focal plane position in water with respect to oil	49	

LIST OF FIGURES

Figure 3.13	spatial resolution of multi-plane phase-contrast imaging system	50
Figure 3.14	Acquisition of multi-plane phase-contrast image frames	52
Figure 3.15	brightness balance, conversion, filtering and background subtraction	53
Figure 3.16	Shear correction	54
Figure 3.17	Image sharpening by 3D deconvolution	55
Figure 3.18	3D tracking of axonemal motion	56
Figure 3.19	Effect of contour padding on calculated curvature and torsion	58
Figure 3.20	Three-dimensional recording of axoneme motion	59
Figure 3.21	Distributions of standard deviations between discretized and fitted position values	60
Figure 3.22	Analysis of axonemal motion	61
Figure 3.23	3D swimming trajectories	62
Figure 3.24	Axial position of different axonemal segments	63
Figure 3.25	Table of mean values and standard deviations of the height distribution for basal end, midpoint, and distal end for the two axonemes	64
Figure 3.26	Frequency of absolute difference value between extrema of axonemal height from surface	64
Figure 3.27	beat frequency	65
Figure 3.28	Twist of an axonemal structure	66
Figure 3.29	Multi-plane interlaced fluorescence setup for imaging of flow tracing single particles in 3D	72
Figure 3.30	Raw image of a single plane and processed maximum projection of image planes acquired from flow-tracing beads	73
Figure 3.31	GUI of the TNT software and the setting parameters used	74
Figure 3.32	3D tracking of single particles obtained by multi-plane fluorescence system	75
Figure 3.33	Velocity field a single flow tracing particle moving in a <i>Marangoni</i> flow before and after collision to a droplet border	76
Figure 3.34	Total velocity	77
Figure 3.35	Stream lines and contact angle	78
Figure 3.36	Three color fluorescence image of a stained fixed Vero cell	81
Figure 3.37	Spectral unmixing	84
Figure 3.38	3-color 8 planes	84
Figure 3.39	Illumination path of three color multi-plane setup	85
Figure 3.40	Schematic of 3-color multi-plane fluorescence microscope	86

Figure 3.41	Eight-plane three-color image of tetra spectral fluorescent beads at one scan position of calibration measurement	88
Figure 3.42	Brightness and inter-plane distance calibration of color channels	89
Figure 3.43	Instant 3D 3-color imaging of a fixed COS-7 cell	91
Figure 4.1	Dual-color DMD-based LED image scanning microscopy	96
Figure 4.2	Chromatic aberration	98
Figure 4.3	Periodic square illumination patterns	99
Figure 4.4	Sample intensity modulated with structured illumination	99
Figure 4.5	Reconstruction procedure of ISM image	101
Figure 4.6	LED ISM of fluorescent green and far-red emitting beads of 200 nm diameter	103
Figure 4.7	Intensity cross section of green and far-red fluorescent beads	103
Figure 4.8	LED-ISM imaging of Argo-SIM pattern 'E'	104
Figure 4.9	Comparison of dual color wide-field, LED-ISM and deconvolved LED-ISM image of alpha-tubulin and actin in a fixed cell from the <i>vero</i> cell line	106
Figure A.1	NIR total internal reflection based focus stabilizer	110
Figure A.2	Photo of the auto-focus setup	112

LIST OF TABLES

Table B.1	Specifications of components incorporated into the multi-plane phase-contrast microscope	116
Table B.2	Hardware configuration devices for multi-plane imaging	117
Table B.3	Initial setting parameters of configured devices in Micro-Manager for multi-plane imaging	117
Table B.4	Specifications of components incorporated into the 3-color multi-plane fluorescence microscope	118
Table B.5	Specifications of components incorporated into the LED-ISM setup	119

ACRONYMS

ATP	Adonesine Tri Phosphate
CCW	Counter Clock Wise
CSDISM	Confocal Spinning Disk Image Scanning Microscopy
CT	Centering Telescope
CW	Clock Wise
DIC	Differential Interference Contrast
DMD	Digital Micro-mirror Device
dSTORM	direct Stochastic Optical Reconstruction Microscopy
FITC	Fluorescein IsoThioCyanate
FLIM	Fluorescence Lifetime Imaging Microscopy
FOV	Field Of View
FPGA	Field Programmable Gate Array
FWHM	Full Width Half Maximum
GFP	Green Fluorescent Protein
GVF	Gradient Vector Flow
LED	Light Emitting Diode
LDV	Laser Doppler Velocimetry
MTD	Micro Tubule Doublet
NA	Numerical Aperture
ODA	Outer Dynein Arm
OIDL	Outer Inner Dynein Link
OPD	Optical Path Difference
OTF	Optical Transfer Function
PALM	Photo Activated Localization Microscopy
PIV	Particle Image Velocimetry
PMT	Photo Multiplier Tube
PSD	Power Spectral Density

PSF	Point Spread Function
PTV	Particle Tracking Velocimetry
QD	Quantum Dot
QPI	Quantitative Phase Imaging
ROI	Region Of Interest
sCMOS	scientific Complementary Metal–Oxide–Semiconductor
SEM	Scanning Electron Microscopy
SMLM	Single Molecule Localization Microscopy
SNR	Signal to Noise Ratio
SOFI	Super Resolution Optical Fluctuation Imaging
SPAD	Single Photon Avalanche Diode
SRM	Super Resolution Microscopy
STED	STimulated Emission Depletion
TAP	Tris Acetate Phosphate
TCSPC	Time Correlated Single Photon Counting
TEM	Transmission Electron Microscopy
TNT	Track N Trace

INTRODUCTION

Microscopy is the gateway to the invisible world of objects and mysterious creatures which are orders of magnitude smaller than the typical sizes detectable by human eye. Personally, among the most thrilling pictures I have ever closely seen has been the flow of virally-transduced Ribeye-GFP particles moving along the neural branches inside the tissue of the Corti organ in the auditory system of a mouse. Since the inception of microscopy in the middle of 17th century, when Antonie van Leeuwenhoek built one of the primary microscopes until today, the field has continuously evolved, furnishing crucial insights in various fields from fundamental physics, material physics, and geology to nanotechnology, medicine, and cellular biology.

In the simplest form, besides a magnifying lens and a detector, an illumination source is a must for microscopy. Its wavelength is inversely proportional to the microscope resolution. The electromagnetic spectrum visible to human eyes called optical light, is arguably our most vital aiding element to visualize, recognize, and discover the universe from giant celestial scales down to the microscopic world of bio-cellular structures.

Although light has been the first and mostly-used illumination source of microscopes, it is only a minor fraction of the broad spectrum exploited in microscopes today. One example that springs to mind is Ernst Ruska's microscopic design in 1930 who innovated the first electron microscope.

This development addressed the question concerning the resolution limit, i.e., the shortest distance between two adjacent point sources that a microscope is still able to resolve, which was unanswered nearly for two centuries after the introduction of the first microscopes until *Ernst Abbe* theoretically showed that resolving power of an optical microscope is diffraction-limited.

Unlike the classical resolution limit (~ 200 nm) for optical methods, the microscopes employing short electromagnetic wavelengths like X-rays and electron beams considerably bypass the optical resolution barrier resulting in images with extraordinary details (up to few angstroms of resolution). Nevertheless, these techniques exhibit some disadvantages. Firstly they are invasive and often toxic for biological specimens. Secondly, besides their high costs, they only work in a vacuum where no electron scattering occurs. Weighing the pros and cons, one concludes that electron and X-ray microscopes are currently not the first choices for live biomedical imaging.

On the contrary, optical microscopes are relatively more affordable

and handier. Moreover, they are among the least invasive tools which allow imaging and characterization of biological structures in their native states.

There exist two prominent families of conventional optical microscopes; 1- fluorescence microscopes like epi-fluorescent and laser scanning confocal microscopes serving as robust tools in various life sciences [1]. These methods can provide high sensitivity in detection down to single-molecule levels as well as specificity, which allow one to distinguish multiple species, each labeled with a particular fluorophore as different emission wavelengths. However, the acquisition time of fluorescence methods is often restricted to photobleaching, i.e., an irreversible photochemical alteration in fluorophores where they no longer fluoresce.

2- Optical phase-based microscopes like phase-contrast or Differential Interference Contrast (DIC) microscopes, which exploit the physical properties of fluorescent label-free samples like their thickness and refractive index to create a contrast image. These techniques typically lack specificity like those in the fluorescence methods, but instead, they are technically easier and, more importantly, they permit long time measurements, which makes them broadly applicable from material physics to life-sciences [2]

Despite the differences, both mentioned conventional microscopy methods have a common feature: their image is inherently two dimensional. However, it is not surprising that most of the live biomedical applications require a four-dimensional, i.e., (x,y,z,t) data set with a sufficient spatio-temporal resolution. For example, to study cellular functions, one needs a rapid three dimensional (3D) imaging to record the migration of cellular components, which generally reveal 3D motions at various time scales [3, 4]. Other examples are the rapid 3D motion of sperm cells and flagella with more than 50 Hz of beating frequency [5] or the interactions in a neuronal network [6]. Conventionally, the sample or the microscope objective is placed on a piezo scanner to serially acquire 2D images along the optical axis to provide a 3D image that trades off the imaging temporal resolution.

Considerable efforts made to address the problem of low temporal resolution in 3D imaging. Among them are computational quantitative phase imaging (QPI) [7, 8], holographic methods [9, 10] or stereo-microscopy [11] or light-field microscopy [12, 13]. However, all these techniques come at the prices of computationally expensive data processing (QPI and stereo techniques), setup instability and image reconstruction ambiguity (holographic techniques), or resolution inhomogeneity (light-field microscopy).

Recently, a new family of multi-plane microscopes has been developed, allowing one to simultaneously record several focal planes. This can be accomplished via several approaches: using dedicated chromatically-corrected diffraction gratings [14] or using cascaded beam-splitters followed by either tilted mirrors [15] or lenses with

different focal powers to adjust multiple beams with different optical path lengths [16–18].

These techniques significantly enhance the imaging temporal resolution due to their parallelized, i.e., non-scanning acquisition nature, making them promising candidates for 3D living studies. Unfavorably, the temporal resolution of these systems often trades off against the signal to noise ratio or the complexity of the imaging system. Their complexity is related to the maintenance, stability, and adjustment of these imaging systems, which might enormously restrict their broad application.

Moreover, despite the high throughput nature of multi-plane fluorescence microscopes in rendering rapid 3D imaging, they are mainly limited to single color imaging due to the already mentioned technical complications. Also, the applications of such systems are only restricted to bioimaging. In 2018, a novel multi-plane system was introduced benefiting from a single piece of a multiplexed prism, which notably reduces the complexity of such systems [19].

By implementation of such a prism, we present three techniques that develop the concept of optical 3D multi-plane microscopy each in a particular direction:

- We combine a phase-contrast microscope with the multi-plane prism and obtain a non-complex, label-free, 3D optical microscope with high temporal resolution. We apply this system in real-time investigation of the rapid 3D motion of *Chlamydomonas* flagella.
- Using spectral unmixing, we enhanced the specificity of a multi-plane fluorescence microscope. This system instantly obtains a volume image with three spectral channels. Its performance is verified by 3D imaging of three fluorescently-labeled subcellular components in fixed COS-7 cells.
- We extend the applicability of a multi-plane fluorescence microscope by its implementation as a rapid 3D particle image velocimetry method. We examine the performance of this technique in studying single particles tracing the *Marangoni* flow.

Exploiting these techniques, we expand the performance, throughput and application of multi-plane imaging to be widely used as a rapid, 3D, and robust tool in both major families of optical microscopy.

As already mentioned, one drawback of classical optical microscopes is their limited resolution compared to electron and x-ray methods. However, over the last two decades, this limit has been tremendously pushed down to a few nanometers using super-resolution

microscopy (SRM), which one can classify into single-molecule localization microscopy (SMLM) techniques such as STORM and PALM or optics-based super-resolution methods like STED, SIM, and ISM. For many applications, one does not require to push the resolution limit down to a single-molecule level but a decent resolution enhancement with an easy-to-use and inexpensive SRM method is sufficient. In a different project, we develop a SRM method for an epi-fluorescence microscope based on image scanning microscopy (ISM).

- Using a LED light source and digital micro-mirror device (DMD), we set up an incoherent ISM as an add-on to a conventional epi-fluorescence microscope. This system is easy-to-use, inexpensive, and provides simultaneous dual-color imaging. We prove the applicability of this system in super-resolution dual-color imaging of fixed Vero cells.

1.1 STRUCTURE OF THIS THESIS

This dissertation dominantly addresses the problem of low temporal resolution of 3D imaging in the two mostly-used optical microscope types: phase-contrast and wide-field epi-fluorescence.

Chapter 2 presents the fundamental principles behind the key terms and methods employed in this thesis.

Chapter 3 contains three core parts, all based on multi-plane imaging. In the **first** section, we develop a fast 3D and a label free microscope based on a phase-contrast microscope with multi-plane imaging. With this method, the rapid 3D motion of isolated flagella from an alga type *Chlamydomonas* is measured in real-time. In the **second** section, we implement multi-plane imaging on a wide-field epi-fluorescence microscope and employ it in the 3D tracking of flow-driven single particles. In the **third** section, we demonstrate an instant 3 color 3D fluorescent microscope by experimental unmixing of spectral channels in a multi-plane epi-fluorescent microscope.

In chapter 4, we introduce how to realize a dual-color ISM on an epi-fluorescent wide-field microscope employing a LED light source and a digital micro-mirror device.

In chapter 5, we summarize our achieved results and discuss the challenges and outlook ahead.

In chapter 6 (other contribution), we briefly describe how to set up and adjust a focus stabilizer employing an infra-red laser diode back-reflected from a total internal reflection.

This chapter focuses on the core concepts central to understanding this thesis including optical microscopy, multi-plane imaging, phase-contrast microscopy, conventional wide-field epi-fluorescence microscopy, and image scanning microscopy.

Depending on the wavelength range of the illumination source, microscopes are divided into different branches from electron microscopes (for example, a wavelength of 2.5 pm at the kinetic energy of 200 keV) to X-ray microscopes (0.01 – 10 nm) to optical microscopes ($\sim 400\text{--}700$ nm) and infra-red (IR) microscopes ($\sim 0.7\text{--}8$ μm for up to mid-IR range). Electron microscopes can visualize fine structures with an unprecedented resolution. For instance, high-resolution transmission electron microscopy (HRTEM) allows to determine the position of atoms in a material with a resolution better than 0.5 angstrom [20]. X-ray techniques are beneficial due to their capability in deep penetration into the sample while they exhibit an intermediate resolution between the optical and electron microscopes [21]. However, both X-ray and electron microscopy techniques come at the price of non-trivial maintenance, typically invasive sample preparation, and usually toxic to biomedical live samples. Unlike these techniques, the optical methods are typically faster, non-invasive, and more straightforward to implement particularly in living biomedical applications.

2.1 OPTICAL MICROSCOPY

Microscopes create a magnified image of small objects which cannot be seen by the unaided eye. Back in the 13th century, single pieces of convex glasses were employed to enlarge an object's image or to focus sunlight on a tiny spot to set fire. Both, the quantity and quality of employed lenses improved drastically in the progress of time. In simple words, a microscope is constructed from two essential elements: an illumination source and an imaging (detection) system, which comprises several magnifying components and a light detector like the human eye.

Back in the 17th century, primary compound optical microscopes were principally constructed from two lenses. To study the detection system in detail, let us describe how one images an object like a candle via the simplest compound optical microscope. Fig. 2.1 depicts such an imaging system.

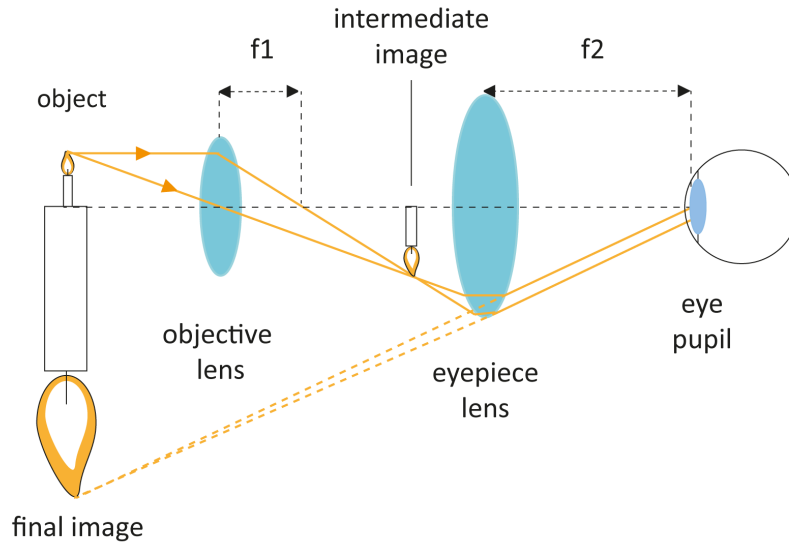


Figure 2.1: Principle of the earliest compound optical microscope. The objective lens with the focal length of f_1 and the magnification factor of M_1 collects the candle's visible radiated light rays and creates an inverted magnified intermediate image. The intermediate image is further magnified by the eyepiece lens with the focal length of f_2 and the magnification factor of M_2 and makes the final image detectable for the eye. The lateral magnification of the imaging system equals to $M_{lat} = M_1 \times M_2$.

An objective lens with a focal length of f_1 and a magnification factor of M_1 close to the candle collects the radiated visible light from it and creates a real intermediate image. By convention, an image is real when it is formed by converging rays and virtual when diverging rays create it. The second lens called the eyepiece lens, with a focal length of f_2 a magnification factor of M_2 , further magnifies the intermediate image and makes an inverted virtual image. Thus, the final image is magnified by a factor of $M_1 \times M_2$ (known as lateral magnification, M_{lat}) with respect to the object size.

Today's objectives are typically infinity corrected, meaning that they create an intermediate image in infinity. Thus, one requires a tube lens to combine it with such objectives to create a real image recordable by a camera. Therefore, incorporation of a light source associated with an infinity-corrected objective, a tube lens, and a light sensor (camera) is sufficient to set up a high magnification optical imaging system. The lateral magnification of such an infinity corrected two-lens imaging system equals to $M_{lat} = f_2 / f_1$ where here f_2 is the focal length of the tube lens.

2.1.1 Axial magnification

To derive the connection between the lateral and axial magnification M_{ax} , let us temporarily assume the objective and tube lens as a single compound lens with the focal length of f_{total} shown in Fig. 2.2.

With a paraxial approximation, one can estimate the axial magnification as the square of the lateral magnification M_{lat} . The paraxial approximation holds as long as the distances in the object plane are much smaller than the focal length of the objective. This approximation is valid, for example, when one uses a 60x NA 1.2 water objective (UPLSAPO60XW, Olympus) with a focal length of 3 mm to detect two planes 300 nm apart. The relation between the axial and lateral magnification can be derived when one calculates the shift in the position of the image plane due to a slight shift in the position of the object plane.

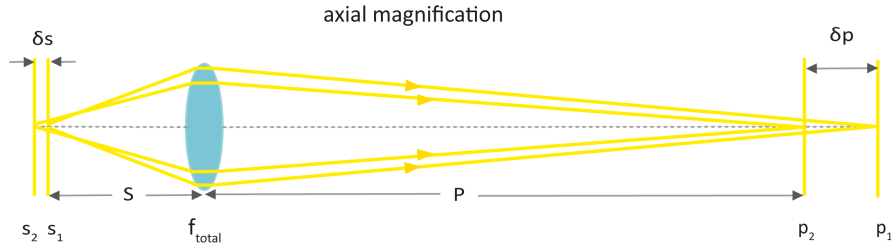


Figure 2.2: Axial magnification. An object with two planes s_1 and s_2 is in a distance of S from a compound imaging lens with a focal length of f_{total} that creates corresponding inverse images of p_1 and p_2 in the image plane where p_2 is in a distance of P from the lens and $P \gg S$. An inter-plane distance of δs in the object plane will be translated to a distance of δp in the image plane where $\delta p \sim \frac{P^2}{S^2} \delta s$.

Fig. 2.2 shows a single-lens imaging system using the already mentioned compound lens. Let us assume that the object with the distance S from the lens is initially located at the position s_1 and is imaged onto the position p_1 in the image plane with a distance P with respect to the lens. Now, let us assume that the object is slightly shifted along the optical axis with respect to the lens (from the s_1 to the s_2 equal to δs). This in turn results in displacement of the image plane from the p_1 to the p_2 equal to δp . One can write :

$$M_{lat} = \frac{P}{S} \quad (2.1)$$

$$M_{ax} = \frac{\delta p}{\delta s} \quad (2.2)$$

one can approximate δp as

$$\delta p \sim \delta s \left. \frac{dP}{dS} \right|_{s_1} \implies M_{ax} \sim \left| \frac{dP}{dS} \right| \quad (2.3)$$

where d is the total derivative operator. The constant f in the thin lens equation, i.e., $\frac{1}{S} + \frac{1}{P} = \frac{1}{f}$, implies that:

$$d\left(\frac{1}{S} + \frac{1}{P}\right) = 0 \implies \frac{dP}{dS} = -\frac{P^2}{S^2} \quad (2.4)$$

Consequently, an image is approximately magnified with square of lateral magnification along the optical axis.

$$M_{ax} \sim M_{lat}^2 \quad (2.5)$$

2.1.2 Imaging resolution

An important property of a microscope is its resolution, meaning, how far do two objects have to be, in order to appear separated from each other. This resolution is limited by the diffraction of light. For the first time in 1873, Ernst Abbe reported that this limit (in lateral dimensions ($\delta_{x,y}$)) is a function of the numerical aperture (NA) of the microscope objective and the wavelength (λ) of emission light as:

$$\delta_{x,y} = \frac{\lambda}{2NA} \quad (2.6)$$

Known as the Abbe limit stating that for the highest NA in air, i.e., $NA = 1$, the spatial resolution of the classical microscopes cannot be smaller than half the wavelength of light. Numerical aperture (NA), depicted in Fig. 2.3, exhibits the highest possible half-angle of the cone of light over which a lens like a microscope objective (serving as a compound lens) can collect or exit photons where it is defined as $NA = n \sin(\theta_{max})$. θ_{max} denotes the maximum angle of light rays collectible by the objective and n is the refractive index of the medium where the objective lens works.

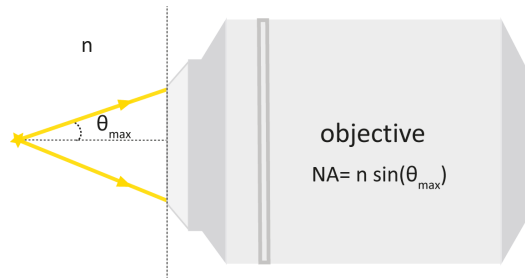


Figure 2.3: Numerical aperture of an objective.

Similarly, in the axial direction, the smallest depth resolvable is also limited, expressed as the axial resolution or often equivalently termed as the depth of field (DOF), δ_z :

$$\delta_z = \frac{\lambda}{n(1 - \cos(\theta))} \sim \frac{2n\lambda}{NA^2} \quad (2.7)$$

Equations 2.6 and 2.7 imply that the highest optical resolution obtainable at an emission wavelength of 550 nm approximately equals to 200 nm in the lateral and 500 nm in the axial direction when one uses a NA 1.49 oil immersion objective.

2.1.3 Köhler illumination

An important concept in modern optical microscopy is to illuminate the object of interest homogeneously. This is particularly relevant when one uses a white light source with a non-uniform shape, resulting in a locally uneven illumination. The classical *Köhler* illumination [22], is commonly applied to achieve an even illumination across the field of view yet to avoid the light source image's appearance in the final object's image. This is shown in Fig. 2.4. One can assume a light source as a superposition of many point sources. Compared to the critical illumination, which only exploits a condenser lens to project each light point source on the sample, the *Köhler* illumination benefits additionally from a collector lens, which focuses each point source at the back focal plane of the condenser lens (condenser diaphragm). Afterwards, the condenser lens projects the received focused light rays through the sample as parallel rays.

Fig. 2.4a displays how two light rays from such a point source at one corner of the light source arrive at the sample (object) plane. Firstly, it implies that the light source image is created neither at the object plane nor in the camera plane. Secondly, and more importantly, the point source's light rays arrive at the sample in parallel, implying an even illumination (they create the point source image in infinity). Correspondingly, Fig. 2.4b shows the imaging path, where one can observe that each point of the object receives light from all the point sources across the illumination source. Therefore, using a *Köhler* illumination, also known as wide-field illumination, one can ensure that each object's point equally receives light from each part of the light source. Also, each point source equally contributes to illumination.

2.2 ADVANCED TRANSMITTED OPTICAL MICROSCOPY

Modern optical microscopes can be classified into two prominent families: Advanced non-fluorescence methods such as phase-contrast and differential interference contrast (DIC), etc., and fluorescence methods, like wide-field epi-fluorescence and fluorescence confocal microscope. In the next sections, we present a brief review of the principles and scope of application for these techniques.

Besides the hardware required for imaging, the inherent physical properties of the object itself, including its thickness and local refractive index determine its visibility in a microscope.

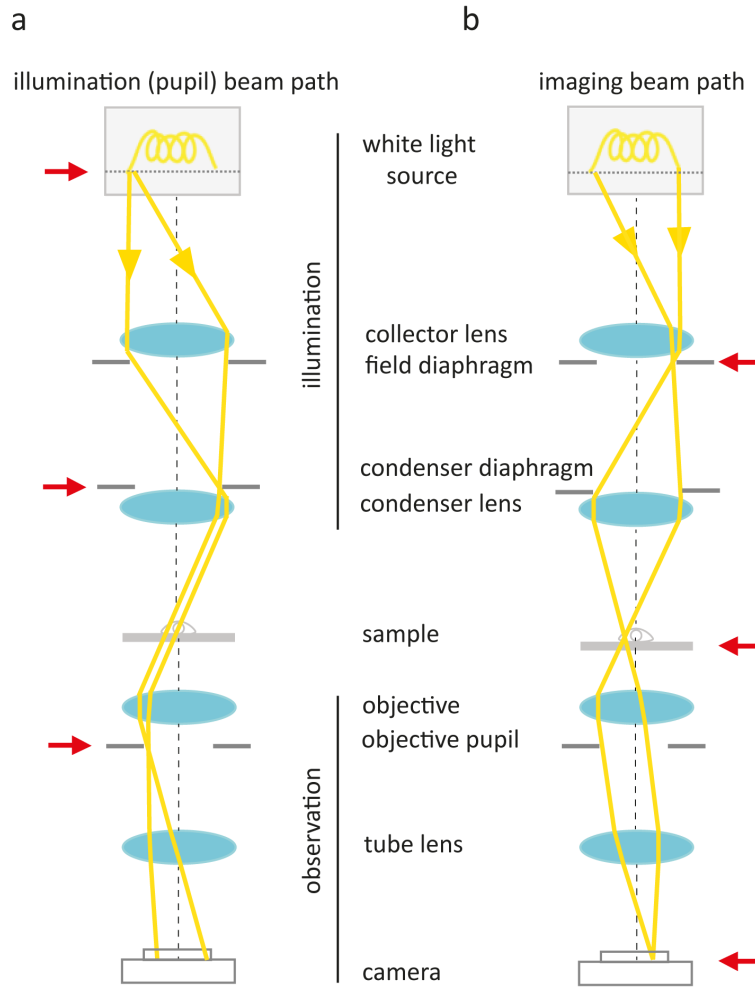


Figure 2.4: Illumination beam path (a) and imaging beam path (b) of a conventional wide-field optical microscope. Ray paths in (a) show the principle of *Köhler* illumination used for evenly lighting a sample. Red arrows highlight conjugated planes.

In detail, the optical wavefront (the geometrical location of the isophase points in a traveling electromagnetic wave) locally changes due to its absorption or retardance inside the object [23]. The magnitude and distribution of change in the wavefront are directly proportional to the distribution of the refractive index and thickness across the object. The job of a non-fluorescence microscope is to record these locally retarded wavefronts as contrast in image intensity. Therefore, it is not surprising that the non-fluorescence microscopes are typically distinguished based on their illumination approach.

In a general view, whether one collects the reflected light or the transmitted light from an object, one can classify the non-fluorescence optical microscopes. Reflected light microscopes are widely used in surface studies in metallography where the object is opaque while the transmitted light microscopes are applicable typically in case of low refractive index object transparent to optical light. Here we focus on

the transmitted light methods.

In one of the simplest forms, in bright-field microscopy, a condenser lens focuses a white light onto an object or transparent specimen for illumination shown in Fig. 2.5a. A part of the illumination light is scattered from the object or absorbed by it, which will consequently emerge as a local change in light wave's amplitude. The objective collects the remaining light, and the camera records the intensity distribution, i.e., the amplitude's square, which appears darker with respect to the background in the bright-field image. Because the transparent and thin biological samples typically make small variations in the optical path of light, it is no wonder that the bright-field microscope does not render a sufficient image contrast. Let us see how the phase-contrast and DIC methods tackle this problem.

Without a doubt, the phase-contrast microscope, invented by *Zernike* in 1930, is one of the milestones in the history of microscopes such that this work was awarded with the Nobel prize in 1953. The phase-contrast microscope benefits from a phase annulus in its illumination path passing only a ring-like cross-section, which will form a cone of light after the condenser lens. Combined with an objective with a NA smaller than the NA of the annulus, this configuration is known as dark-field microscopy. This imaging system readily enhances the image contrast because it blocks the direct illumination light from the detector. This gives high contrast images, but usually, only the circumference of the objects are recognizable.

To further improve the visibility of details, the phase-contrast microscope uses a phase objective that possesses a phase plate at its rear plane (Fig. 2.5b). This phase plate is conjugated with the phase annulus to increase the phase shift or retardation of the scattered/absorbed light with respect to the direct light by $\pi/2$ (positive phase-contrast) or $-\pi/2$ (negative phase-contrast). In the image plane, the retarded direct light interferes with the light that was scattered and diffracted by the specimen. In the case of positive phase-contrast, the direct light crosses the opaque ring, resulting in a larger phase shift with respect to the scattered light where the specimen appears dark in a bright background (biological specimens have typically higher refractive indices than their surrounding medium). In the negative phase-contrast, the dark and bright regions of the phase plate are inversed compared to those in the positive phase-contrast so that the specimen looks brighter than the image background.

All in all, in both cases, the increased phase shift between the direct light and the scattered light results in a more efficient constructive (negative phase-contrast) or destructive (positive phase-contrast) interference between these two lights giving rise to enhancement of difference between the amplitudes of the interfered and direct light (Fig. 2.5d) which appears as a higher image contrast when compared

to those in a bright-field microscope (Fig. 2.5c).

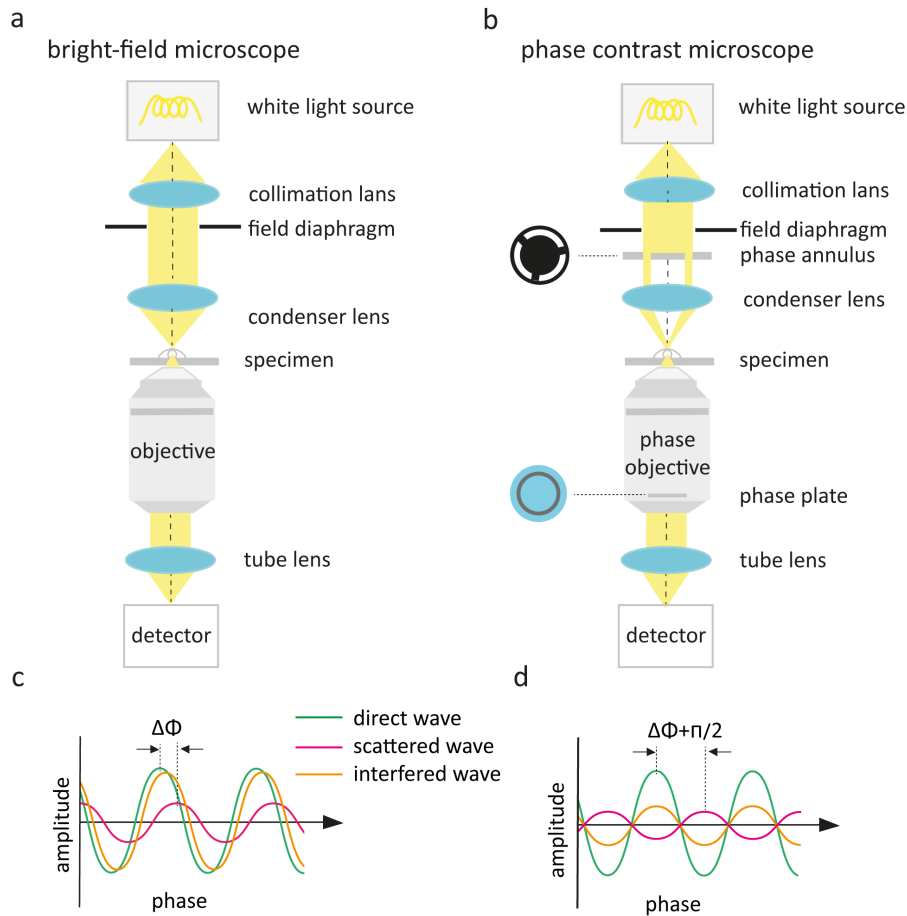


Figure 2.5: Bright-field versus phase-contrast microscopy. (a) bright-field microscope setup where a collimated white light is focused onto a specimen for illumination. The scattered light from the specimen interfered with the transmitted (direct) light is collected using an objective and is imaged onto a detector via a tube lens. (b) phase-contrast microscope setup with the components same as (a) but instead of typical objective, it contains a phase objective conjugated with a phase annulus in the illumination path, between collimation and condenser lens, to increase the phase shift between the scattered and transmitted light by $\pi/2$ (corresponding to quarter wavelength) resulting in improvement of image contrast with respect to the bright-field. Relative phase and amplitude of the direct light (green) and the scattered light (pink) as well as the interfered light (orange) for a (c) bright-field and (d) phase-contrast microscope. Images are reproduced by adaption from (MICROSCOPYU)

Fig. 2.6a, b accordingly present the bright-field and the phase-contrast image of a bulk of inactive isolated *Chlamydomonas* flagella. As can be observed, flagella are barely visible in the bright-field image, whereas the phase-contrast image exhibits a much more distin-

guishable picture from the flagella.

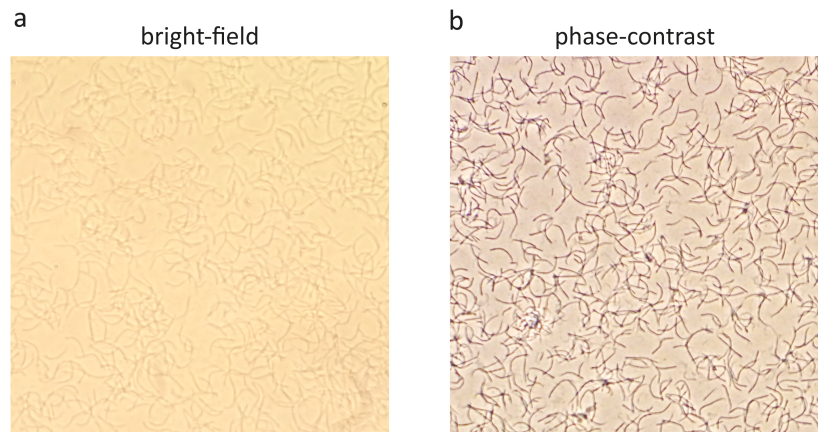


Figure 2.6: BrightField (a) and positive phase contrast (b) images from a bulk of isolated *Chlamydomonas* flagella.

The diffraction halo light appearing as a tiny bright or dark edge around the sample's boundary is an intrinsic artifact to a phase-contrast image, which is due to a small degree of transmission of the scattered light into the ring area of the phase plate where it should be ideally transmissive only for the direct (non-scattered) light. However, this effect does not significantly degrade the image quality, particularly when the object of interest has a thin and non-complex structure. Phase-contrast microscopy has been widely implemented in the real-time investigation of various biological living samples because besides its high image contrast, it usually requires a modest amount of light exposure compared to bright-field microscopy and does not need sample's staining and fixing. More importantly, one can image the sample dynamics for a long time because compared to the fluorescence techniques (described in the next section), their acquisition time is not limited by phenomena such as phototoxicity and photobleaching, where the fluorescent molecules are no longer able to fluoresce after a certain amount of time due to the irreversible photo-physical alterations.

In 1952 Georges Nomarski invented the DIC microscopy, which is based on the interference of two polarized light beams with an equal amplitude in which their relative optical phase is shifted by the transparent object (Fig. 2.7a). An optical element, the so-called Nomarski prism, an optically anisotropic material which exhibits different refractive index depending on the polarization of light (birefringent prism), spatially splits a linearly polarized beam (with a 45° polarization) by a distance, so-called shear distance, nearly equal to half the microscope's optical resolution into two beams with perpendicular polarizations with respect to each other. These two beams are

then focused onto the object using a condenser lens and undergo a phase retardation, equivalent to a change in their relative optical path, dependent on the object's refractive index and thickness distribution. An objective collects these beams. A second Nomarski prism compensates the spatial shift between the two beams and re-aligns them, leading to the interference of two beams. Finally, a second polarizer (Analyzer) transmits the interfered beam with an orthogonal polarization with respect to the beam polarization at the first polarizer. This, in turn, results in halo-free and pure reconstruction of the object's optical phase distribution as a contrast in the image intensity where one side of the object's image appears darker, and the opposite side appears brighter with respect to the image background. Fig. 2.7b, c shows the DIC image of a dividing Hela cell and a stem cell, respectively. The dark and bright shadows at the two opposite sides of the samples can be clearly observed, which results in a volumetric image.

As mentioned, typical DIC microscopes render a three-dimensional (3D) image of an object but only in a qualitative manner. In other words, they do not provide a straightforward and quantitative approach to measure the axial (out-of-plane) components of an image because the intensity distribution across a DIC image is not linearly related to its differential phase. It worth noting that in the case of planar imaging of thin samples with non-complex structures, phase contrast image is preferential because it gives a higher contrast between the sample and background compared to a DIC image.

In chapter 3, we demonstrate how to extend the application of a phase-contrast microscope to three spatial dimensions.

2.3 FLUORESCENCE MICROSCOPY

In the following section, we start with a key concept in optical microscopy, so-called fluorescence, which provides a fundamentally different approach to studying fine objects compared to the non-fluorescence techniques described so far. In fluorescence methods, one needs to label the structure of interest with fluorescent molecules that can be efficiently excited with a specific wavelength and emit light with a different wavelength. The already mentioned non-fluorescence methods are broadly applied in real-time observation of a sample because firstly, there is no need to label it with fluorescent molecules in advance. Secondly, the sample is less prone to photo-toxicity because one uses a broad spectrum of white light in non-fluorescence methods, whereas typically a narrower range in the light spectrum, particularly in the blue region (400 – 480 nm), is used to excite molecules in the fluorescence techniques. However, non-fluorescence methods lack the property of specificity, which is one of the features that separates them in application from the fluores-

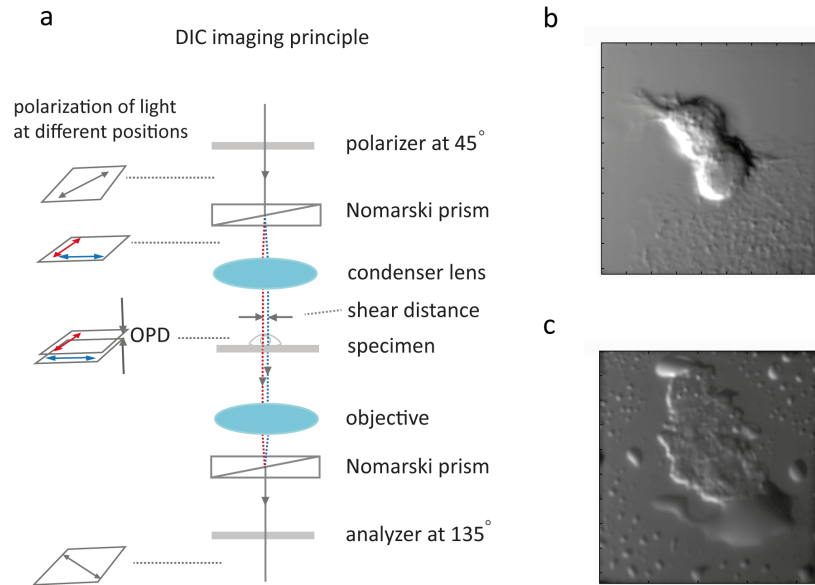


Figure 2.7: DIC microscopy. (a) DIC principle, the First polarizer generates a polarized light with a 45° direction with respect to its fast axis. A Nomarski prism spatially splits the incidence light into two orthogonal polarization shown in red and blue dashed lines. The specimen thickness and refractive index make optical path difference (OPD) between the two polarized beams. Afterward, two beams are recombined by a second Nomarski prism followed by passing through an analyzer with a fast optical axis oriented in a 90° angle with respect to the polarizer's fast axis to transmit a pure interfered light. DIC image of (b) dividing Hela cells and (c) stem cell.

cence methods.

2.3.1 Fluorescence

Fluorescence is a ubiquitous phenomenon observed in a huge variety of matters, from fluorescent minerals to marine organisms. Innumerable examples are around us, from household materials like ordinary plastic pens, liquid laundry detergents to stamps, note bills, and gemstones that emit visible light when they are exposed to ultra-violet light. In nature, one can observe many glowing aquatic species in the sea under a UV light like various types of cnidarians [24], copepods [25], etc.

In terrestrial environments, frog *Hypsiboas punctatus* is probably one of the most exciting species that emits green fluorescent light from its skin when it is illuminated at 400 nm wavelength with low light conditions [26]. The considerable amount of the fluorescent light collected from this species is thought to be a tool for its visual communication at night under the moonlight.

The exploitation of fluorescent dyes and fluorescent proteins in label-

ing bio-species has revolutionized our understanding of underlying biological structures, behavior, and dynamics from macroscopic bio-organisms to nano-scale molecular machines. The most notable example of this type is the Green Fluorescent Protein (GFP), primarily observed in a bioluminescent species, *Aequorea victoria* Jellyfish [27] in 1962. Calcium ions stimulate the protein aequorin in the *Aequorea victoria* Jellyfish to emit a blue light, which is then fluorescently converted to a green light by GFP [28].

The fluorescence process can be well described using the Jablonski diagram presented in a simplified version in Fig. 2.8a.

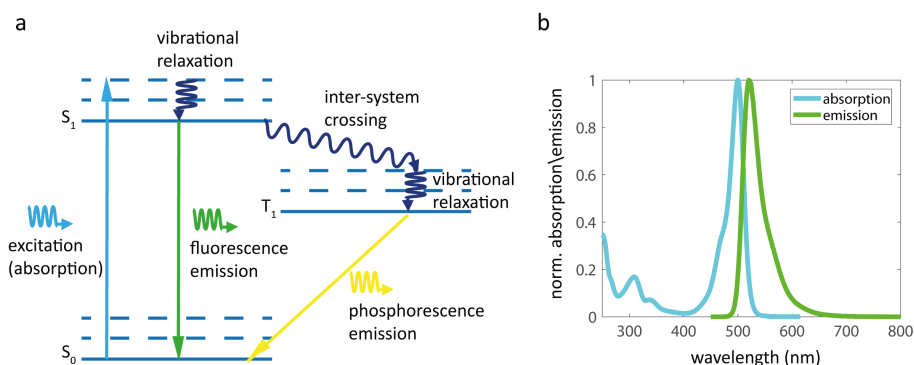


Figure 2.8: Fluorescence. (a) Jablonski diagram, S_0 and S_1 are the ground, and the excited electronic states, respectively, and T_1 represents the triplet states. The blue curved arrow shows the absorption, whereas the green and yellow curved arrows show fluorescence and phosphorescence correspondingly. The dark blue curved arrows indicate the non-radiative transitions. (b) Absorption and fluorescence spectrum of the ATTO 488 in PBS. Data is adapted from the manufacturer (ATTO-TEC).

S_0 , S_1 , and T_1 are different energy states that electrons can occupy. In each energy state in Fig. 2.8a, different rotational or vibrational states are displayed as solid and dashed lines in blue. A molecule in its ground state S_0 can transit to an excited state S_1 via absorbing excitation photons (shown as zigzag blue arrows). The relaxation of the molecule to its ground state is possible in two different scenarios: fluorescence process where the molecule relaxes directly to its ground state associated with the emission of a red-shifted photon, shown as a zigzag green arrow. The whole process occurs very quickly on the order of nano-seconds, known as fluorescence life-time.

The Stokes shift between the excitation and emission wavelength is due to the fluorophore's energy loss in its excited state arising from vibrational relaxations.

Alternatively, due to the inter-system crossing, the molecule can transit initially from S_1 to a triplet state, T_1 , a state also known as the dark state, with an energy level between S_0 and S_1 . The relaxation from the triplet state to the ground state can be either non-radiative

or accompanied by the release of red-shifted photons through a phosphorescence process. Phosphorescence is less likely to occur and is also a much slower process (with an average life-time in order of micro-seconds) compared to fluorescence.

2.3.2 *Epi-fluorescence and confocal laser scanning microscopy*

One can practically distinguish between the excitation and the emission lights by means of a dichroic mirror oriented in 45° with respect to the incident (excitation) light. The dichroic mirror reflects the excitation wavelength while transmitting the fluorescence emission wavelength collected from a fluorescently-labeled specimen. Additional narrowing in wavelength band-pass is obtained by excitation and emission filters. Fig. 2.9 presents two well-known and widely-used fluorescence microscope configurations: wide-field epi-fluorescence and confocal laser scanning microscope. We have only used the wide-field microscope in this thesis. However, we discuss both techniques to better understand their principles, performance, and applicability. Further, wide-field microscopy is usually the core platform used in a relatively novel optical microscopy concept, so-called super-resolution microscopy (SRM), which principally aims to enhance spatial resolution. We discuss this concept more in detail in the last section of this chapter.

Let us assume a 3D sample as several sequential sections. The 'Wide-field epi-fluorescence' term denotes when one illuminates all the sample's planes equally. This is done by focusing an excitation light (shown in blue) at the back focal plane of an objective (Fig. 2.9a), which renders a collimated light along the optical axis in the sample plane. The fluorescence light (shown in green) is collected by the same objective and separated from the excitation light when it is transmitted through a dichroic mirror followed by passing through a band-pass emission filter. Epi-fluorescence illumination also leads to the excitation of the fluorophores existing out of the focal plane, which contributes to the image as a background degrading the image contrast.

In confocal laser scanning microscopy, however, a collimated laser light illuminates the back focal plane of the objective to create a focused excitation onto a tiny area of the sample. The focused excitation is scanned across a section of the sample through a beam scanner like galvo mirrors that deflect the beam in both lateral dimensions. The fluorescence emission is isolated from the excitation light, similar to that of the wide-field. Unlike epi-fluorescence microscopes, confocal microscopes benefit from the optical sectioning capability. This is due to a pinhole in their detection path to block the out-of-focus emission lights. However, due to the beam scanning, these systems typically suffer from a poor temporal resolution, i.e., slow acquisition

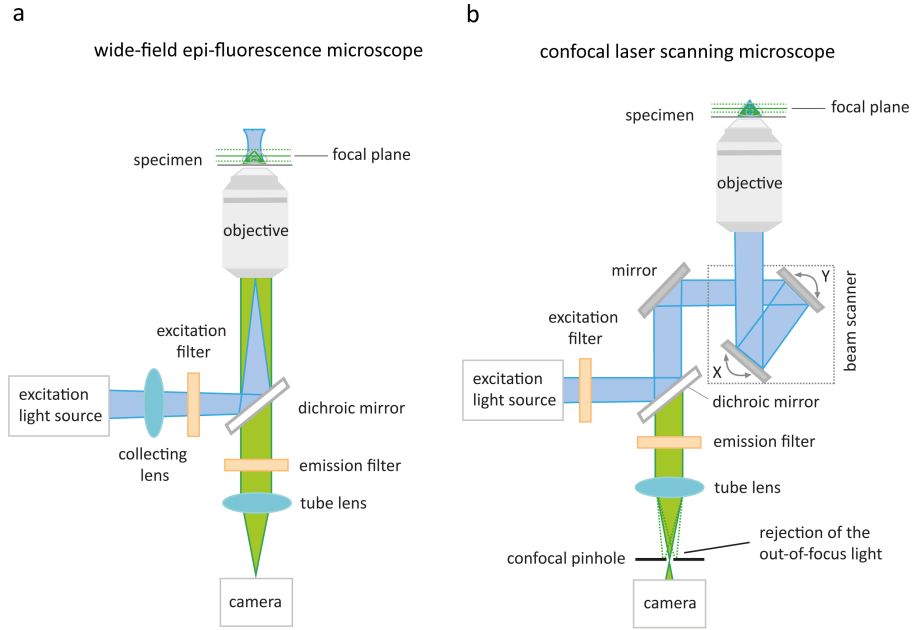


Figure 2.9: Epi-fluorescence (a) versus confocal laser scanning microscope (b). In (a), A collecting lens focuses the excitation light (in blue) at the back focal plane of an objective resulting in equally illuminating different sections of a specimen. The fluorescence emission (in green) is back-reflected through the objective, separated from the excitation light by a dichroic mirror followed by an emission filter. In (b), A collimated excitation light is focused onto the specimen by an objective. A beam scanner sweeps the focused light across the sample in both lateral dimensions. A confocal pinhole blocks the out-of-focus lights resulting in optical sectioning.

speed when compared to a wide-field microscope, which usually restricts their application to structural studies in specimens and relatively slow dynamics.

To realize how these two types of microscope form an image in detail, let us briefly review the theoretical background behind their image formation. In principle, a microscope does not practically image a point source into a point, but instead, spreads the point's intensity into a disk due to the light's diffraction.

One can extend this concept to three spatial dimensions where a light-emitting spherical point source in the object plane will be imaged as an ellipsoid so-called point-spread function (PSF). PSF can fully represent the properties of a microscope like optical aberrations, magnification, and resolution. As a result, one can obtain the image intensity recorded by a detector $I(r')$ as the convolution of the object's function, i.e., the intensity distribution of the real object $O(r)$ with the microscope's PSF $U(r')$ where r and r' are the spatial coordinates in the object plane and image plane accordingly.

$$I(r') = O(r) \otimes U(r') \quad (2.8)$$

PSF of a fluorescence microscope is the combination of the excitation PSF $U_{exc}(r')$ and the detection PSF, $U_{det}(r')$.

$$U(r') = U_{exc}(r') \cdot U_{det}(r') \quad (2.9)$$

As mentioned, both the excitation and detection are different in wide-field and confocal laser scanning microscopes, which proportionally affects the shape of their $U_{exc}(r')$ and $U_{det}(r')$. The mathematical details are well-described in Ref. [29]. Fig. 2.10a presents a cross-section (xz view) of a theoretically calculated PSF with the normalized intensity of a wide-field microscope performed for a water immersion objective with NA 1.2. One can observe the background intensity around the central high intensity distribution as well as the stretch of the intensity distribution along the optical axis, which demonstrates how the axial resolution is lower than the lateral one (Eqns. 2.6 and 2.7).

One can better explain the imaging quality including image resolution in the spatial frequency domain. To this end, the optical transfer function (OTF) calculates the 3D Fourier transform of PSF to provide the 3D distribution of spatial frequencies collected by a microscope.

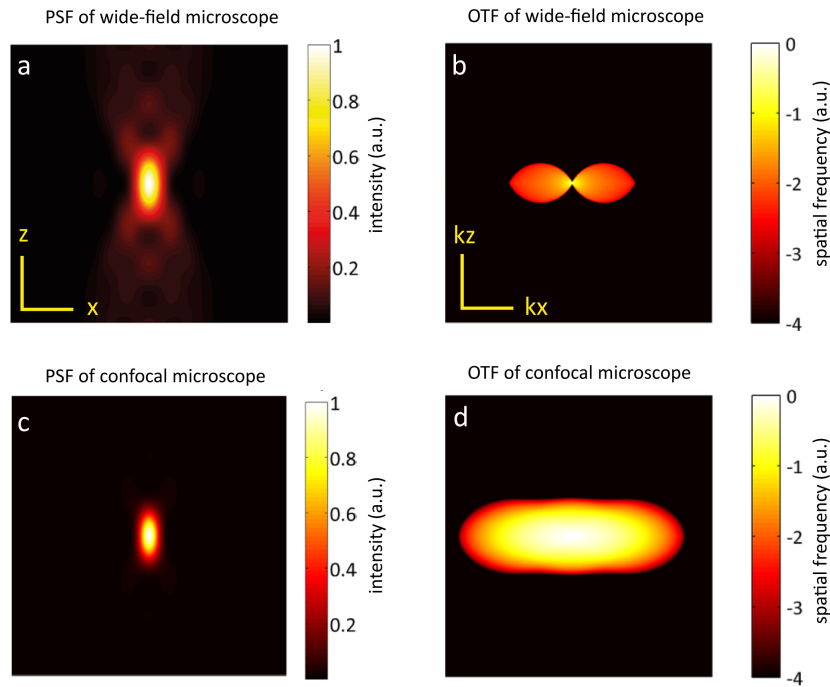


Figure 2.10: PSF and OTF of a wide-field and a confocal microscope. Images are adapted from Ref. [29].

An OTF cross-section of a wide-field microscope is illustrated in Fig. 2.10b where the color bar shows the decadic logarithm of spatial frequencies. One can imagine the 3D shape of the OTF by the rotation of this section around the optical axis (z). Besides the background

blur around the wide-field PSF, the limited extent of the OTF along the k_z indicates the poor axial resolution of a wide-field microscope. To overcome the challenge of low spatial resolution and background image blur in a wide-field image, one can exploit the *priori* knowledge about the microscope's PSF and recorded images in order to back-calculate for obtaining the object's function, which is the core idea of an image processing approach so-called image deconvolution. Alternatively, today's SRM techniques have overcome this problem via different approaches. We will briefly describe the SRM in the last section of this chapter.

Unlike the wide-field microscope, confocal PSF barely shows the background intensity resulting in optical-sectioning. Fig. 2.10c shows the background-free confocal PSF which has shrunk in both axial and lateral dimensions when compared to the wide-field PSF.

The confocal PSF is calculated for a system with infinitesimally small pinhole and focused excitation. The rest of the calculation parameters is the same as those used for the wide-field PSF. Equivalently, the OTF of the confocal (Fig. 2.10d) represents the extended supports of the spatial frequencies in all spatial dimensions. Unlike the enhancement in the image contrast and the spatial resolution, confocal-based systems typically offer low temporal resolution when compared to the wide-field microscopes since they require to scan over the entire sample point by point, resulting in restriction of their application only to structural studies or relatively slow dynamic processes. Further, they deliver relatively low light throughput, i.e., a limited number of photons per scan time, which has currently prevented their usage in most super-resolution techniques.

To obtain a 3D image from a sample in all the optical microscopes mentioned so far, the temporal resolution of imaging significantly drops as one records a stack of scan images along the optical axis. In the following section, we focus on a promising solution to the poor temporal resolution in 3D imaging.

2.4 MULTI-PLANE IMAGING

The resolution and the depth of field of an imaging system are often inversely proportional. In other words, a rise in the numerical aperture of an imaging system enhances its resolution but also results in the reduction of its depth of field. In photography, commonly, the camera lenses with small f-numbers (defined as the ratio of the focal length to the aperture size of a lens) are widely used in portrait or wildlife photography where one requires to emphasize on the object of interest by imaging that with an ultra high resolution in a shallow background (low depth of field). In contrast, high f-number photography is suitable for landscape imaging, where capturing a

broad view in all three spatial dimensions with a reasonably satisfactory resolution is desired. In optical microscopy, however, both the parameters are often required when one deals with ultra-fine structures distributed in a volumetric region like a cell. Besides these two factors, imaging speed plays a crucial role in detecting rapid dynamics, particularly in living specimens. However, as a well-known compromise, when the spatial resolution increases, the temporal resolution decreases and vice versa. To overcome this problem, several techniques have been proposed over the last decade. Here, we focus on one of the most promising techniques of this type: multi-plane imaging, also known as multi-focal imaging.

Let us assume in a photon emitting sample, we have two planes P_1 and P_2 , apart from each other with a distance of dz (Fig. 2.11a), and we are going to image them using an imaging system with $M_{lat} > 1$, comprised of an objective and a tube lens with a fixed distance with respect to each other. Conventionally, one needs to first focus the objective focal plane on the P_1 position, which accordingly creates image P'_1 at a time t_1 (the orange rays). To image the plane P_2 (the yellow rays), one should move the imaging system with respect to the sample to focus on plane P_2 (at a time $t_2 > t_1$). In other words, one needs to scan the sample along the optical axis, which takes the time of $dt = t_2 - t_1$.

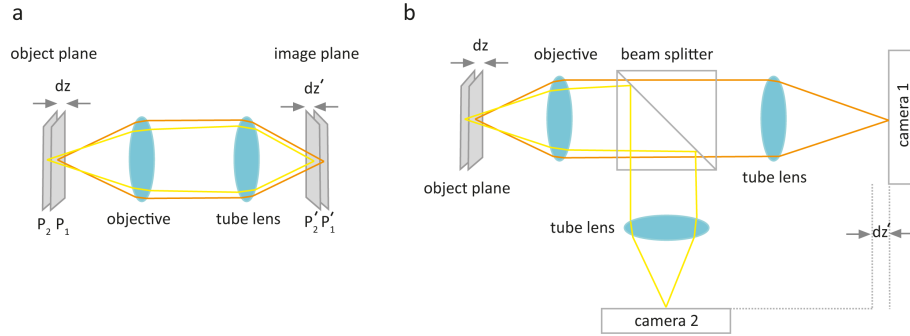


Figure 2.11: Bi-plane imaging concept. (a) Scanning a sample along the optical axis. Sequential planes P_1 and P_2 with a distance of dz from each other along the optical axis are accordingly imaged to P'_1 and P'_2 using an imaging system comprised of an objective and a tube lens. dz' indicates the inter-plane distance of images P'_1 and P'_2 . (b) Simultaneous imaging of two sequential planes. The beam-splitter divides the beams into two perpendicular directions where camera 1 and camera 2 record planes P_1 and P_2 respectively. Camera 2 is displaced by a distance of dz' with respect to its focal plane. Rays in orange and yellow correspondingly belong to the closer and farther planes to the objective.

Now, let us assume that the objective can capture the rays of both planes. To image the two planes simultaneously, i.e., $dt = 0$, called bi-plane imaging, one can split the detection light into two orthogonal paths using a 50R:50T beam splitter and image each of them using a

camera (Fig. 2.11b [30]). One key point is that, with respect to the position of objective, the camera 1 (imaging the plane 1) is by a distance of dz' farther than the camera 2. In other words, with respect to the objective position, the optical path length of the yellow and orange rays are different. Thus, the core idea in multi-plane imaging is to create multiple beams, apply a change in their relative optical path lengths, and image them all simultaneously. Similarly, one can extend the concept of bi-plane to multi-plane imaging.

Using several cameras each to record an image plane gives the benefit of capturing the whole field of view. However, such a system is inefficient because, in the case of recording many focal planes, the implementation of multiple cameras makes the imaging system bulky. More importantly, defocusing a camera from its nominal focal plane increases the spherical aberration of imaging.

Compared to the conventional single-plane, the increased depth of field in a multi-plane system is often equivalent to a reduced field of view. This is technically accomplished by the insertion of a field stop in the detection path to apodize the effective aperture of the image planes and prevent any overlap between them.

A higher number of planes increases the sampling rate along the optical axis, but it comes at the price of lower signal to noise ratio (SNR) at each plane. In other words, the number of planes is inversely proportional to the signal strength in each image plane. Therefore, one needs to estimate the SNR of an image or the brightness of a sample to select the optimal number of planes. In detail, the image SNR (equivalent to the number of collected photons) is particularly important in accurately tracking moving particles and in high localization accuracy. Not surprisingly, the collected number of photons at a certain time depends on the camera's exposure time or equivalently to the camera read-out speed, which governs the temporal resolution of the imaging system. Therefore, depending on the image contrast or brightness of a sample and the accuracy required for a particular application, one should find the desired compromise between the temporal resolution and the sampling rate along the optical axis, i.e., the number of axial image planes.

One determining factor in the magnitude of the inter-plane distances is the axial magnification. As mentioned in the section 2.1, this factor is a function of the focal length of the lenses exploited in the detection path of an infinity-corrected imaging system. Let us consider the detection path of a typical multi-plane wide-field microscope shown in Fig. 2.12. The optical path retarder applies OPD between sequential image planes and the field aperture locating at the intermediate image plane enhances the depth of field of the imaging system. The magnifying system commonly comprises four lenses, i.e., an objective and a tube lens for the infinity-corrected imaging, which creates an intermediate inverted image at the field aperture

(the rectangular aperture) as well as two telescope lenses to relay the intermediate image onto the camera. Additionally, they can be chosen such that they provide an extra magnification or demagnification factor. Shown below each lens in Fig. 2.12, the focal length of these lenses are accordingly f_{obj} , f_t , f_{r1} and f_{r2} which yields the lateral magnification M_{lat} as:

$$M_{lat} = \frac{f_t f_{r2}}{f_{obj} f_{r1}} \quad (2.10)$$

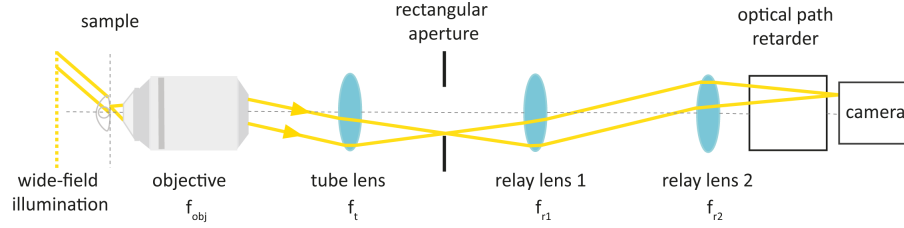


Figure 2.12: Detection path of a typical multi-plane wide-field microscope. An objective, together with a tube lens, creates an intermediate image at the rectangular aperture (field stop), which adjusts the image planes' size. Relay lenses 1 and 2 further magnify and image the intermediate image on a camera. The optical path retarder exerts OPDs among different image planes.

Taking equations 2.11 and 2.10 into account, for the axial magnification we have

$$M_{ax} \sim \frac{f_t^2 f_{r2}^2}{f_{obj}^2 f_{r1}^2} \quad (2.11)$$

Equation 2.11 implies that the inter-plane distance of a multi-plane system can be modified by the replacement of either of the four lenses. However, it is practically inefficient to replace a tube lens, particularly when it is tightly incorporated inside a microscope body. Therefore, the only option is to replace the objective or either of the relay lenses.

Assuming a fixed set of a tube lens and the relay lenses in the detection path, one can estimate the inter-plane distance as a function of the magnification provided in typical objectives available. Plot 2.13 depicts the inter-plane distance obtainable in different lateral magnifications. The lateral magnification M_{lat} in Olympus objectives equals to $180 \text{ mm} / f_{obj}$ where 180 mm is the focal length of the tube lens. The inter-plane distance is calculated with the assumption of 2 mm OPD in a bi-plane imaging system. The magnification factors are set starting from 10 to 150 for some of the objectives provided by Olympus company.

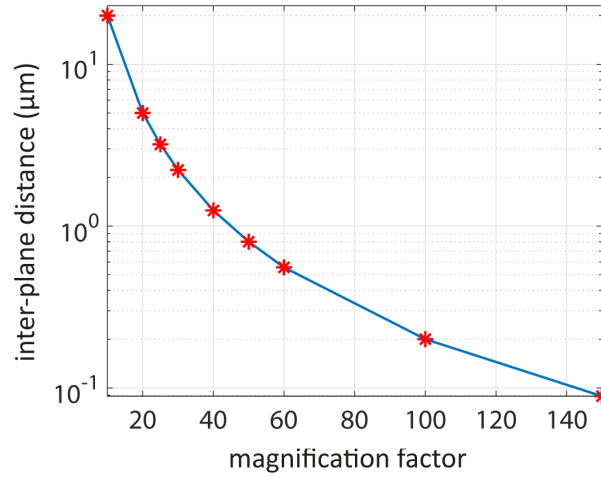


Figure 2.13: Inter-plane distance versus objective's magnification. The OPD is taken equal to 2 mm. Data points along the x-axis is adapted from the manufacturer (**Olympus**) starting from 10x to 150x objectives.

In the design of an optical path retarder, one should consider the Nyquist sampling theorem because, according to this criterium, the inter-plane distance should not surpass half the axial resolution of the imaging system. This implies a careful selection of the magnifying components. As already mentioned in section 2.1, the axial resolution is a function of the emission wavelength, NA , and the refractive index of the sample's medium. Therefore, with the same wavelength and medium's refractive index, the axial resolution is a function of NA , whereas, besides the OPD, the inter-plane distance is dependent only on the magnification factor. NA and magnification are two different, but not independently varying parameters in imaging because typically, the NA of an objective increases together with its magnifying power.

The NA values are set from $NA = 0.25$ typical for 10x objectives to the highest available $NA = 1.7$ for an emission wavelength of 550 nm with air as the sample medium. Consequently, one should wisely select an objective for both the desired magnification and a sufficient sampling rate along the optical axis.

2.4.1 Multi-plane imaging approaches

Multi-plane microscopy can be accomplished via several approaches. Fig. 2.15 shows a part of the detection path starting from the intermediate images to the position of cameras in four different available approaches. Depending on the approach of use, the optical path retarder elements either locate between the relay lenses (Fig. 2.15a, b, d) or between the second relay lens and the camera (Fig. 2.15c). In all of the setups shown, f_1 and f_2 indicate the relay lenses.

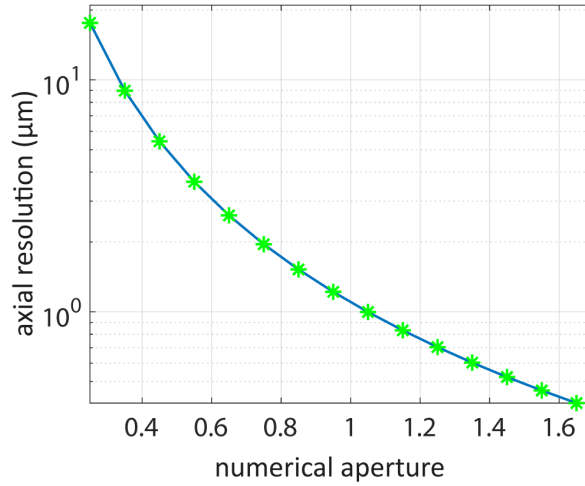


Figure 2.14: Axial resolution versus objective's NA. The emission wavelength is taken 550 nm in the air as the sample's medium. Data points along the x-axis is adapted from the manufacturer (**Olympus**) for the objectives with the NA from 0.25 to 1.7.

These approaches are based on:

1- Dedicated chromatically-corrected diffraction gratings [14].

Fig. 2.15a shows a side view of such a system. The multi-plane inducing elements are located between two relay lenses of f_1 and f_2 where a compound grating with nine diffraction orders splits the intermediate image planes (shown by sequential numbers) into its different diffractive orders and exerts OPDs between them. Another grating (shown as CCG) together with a nine-faceted refractive prism is inserted into the detection path to compensate for the grating-induced dispersion, i.e., the coloration of the exiting diffractive orders. This system delivers the nine intermediate images into a 3×3 array of neighboring image planes on a camera.

2- several lenses with different focal lengths together with several mirrors and beam-splitters [16–18, 31]. Fig. 2.15b presents a schematic of a four-plane system where the beam splitter $bs1$ splits the incident light into two beams: one upward and the other downward with respect to the optical axis. The next beam-splitters $bs2$ and $bs3$ split lights to the left and right, which results in a 2×2 array of adjacent image planes on the camera. Lenses indicated as $fp1$ to $fp4$ with different focal lengths induce desired OPDs.

3- Cascaded beam-splitters and mirrors to adjust eight optical path lengths [15] (Fig. 2.15c). This system is very similar to the second approach, but instead of lenses with different focal powers, the inducing OPDs is accomplished via the adjustment of the tilts in the orientation of mirrors $m2$ with a certain tilt of d and $m3$ with a tilt of $2d$ with

respect to their 45° orientation to the incidence beam where d is the desired OPD desired. As can be seen, this configuration renders two sets of four neighboring image planes each imaged by a camera.

4- Fast scanning deformable mirrors [32] (Fig. 2.15d). A deformable mirror device sweeps the depth of the sample between two focal planes with a high speed. In principle, this system does not render an instant capture of multiple planes like those mentioned in the previous approaches, which besides the SNR, their speed is limited by the camera readout speed. However, considering the fast sweep rate of deformable mirrors (much faster than effective camera readout), one can technically assume them as an instant technique with an extended depth of field.

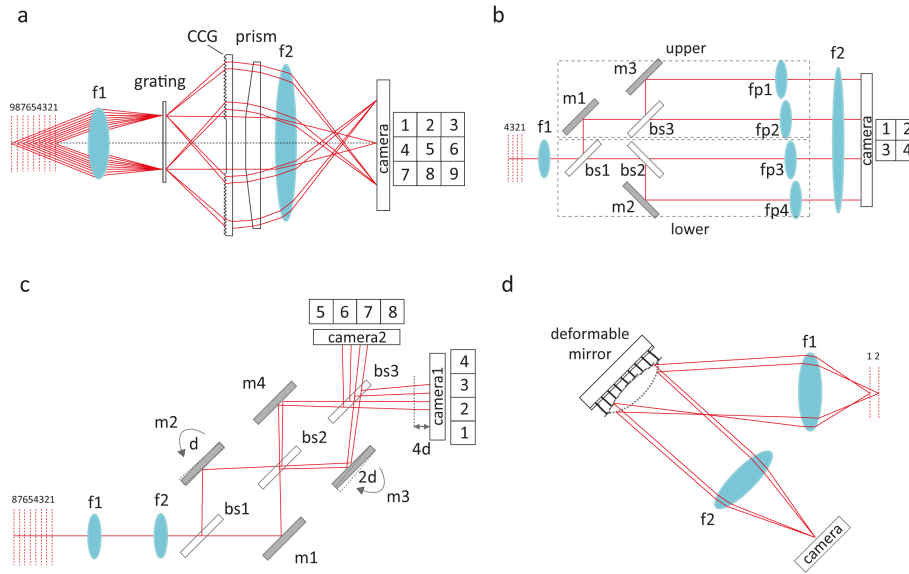


Figure 2.15: Multi-plane imaging with different approaches. (a) Side view of a chromatically corrected grating-based system with nine image planes where a compound grating splits the intermediate focal planes into nine diffraction orders and applies OPD among them. The chromatic compensation grating (CCG) associated with a custom-built prism removes the grating-induced dispersion. (b) Schematic of a many lens system with four image planes. bs , m , and fp with different numbers accordingly indicate beam-splitters, mirrors, and lenses with different focal lengths. (c) Cascaded beam-splitters and adjusted mirrors with eight image planes. Mirrors m_2 and m_3 are tilted equal to d and $2d$ correspondingly where d is the OPD between the focal planes. Camera 1 is displaced by a distance of $4d$ with respect to its focal plane. (d) Rapidly sweeping deformable mirror device with a parabolic surface pattern to provide an extended depth of focus. In all setups f_1 and f_2 indicate the relay lenses. Images a-d are reproduced accordingly by adaption from Refs. [14–16].

Unfavorably, besides being wavelength-dependent, the grating-based systems are complex in optical elements required for aberration correction, which impedes their widespread application. In the second approach, the number of distinct focal planes using a many-lens system is typically restricted to four planes, which is often insufficient to sample the axial range. This is because more optical beam paths make the detection path too bulky and complicated while. Further, more number of planes require a huge sensor. Moreover, the unequal inter-plane distance reported in such systems typically leads to complexity in calibration and image processing.

In terms of being technically demanding alignment, the same holds for the usage of cascaded beam-splitters. Very recently, compound prisms have been employed with the same aims as mentioned in cases 2 and 3, but in a more straightforward manner [19, 33]. In chapter 3, we show how to combine a compound prism proposed in Ref. [19] as a single optical element with two prominent optical microscopic techniques to obtain rapid and 3D yet robust and easy-to-use microscopes.

2.5 SUPER RESOLUTION MICROSCOPY

The sizes of bio-molecule complexes are in the order of few nanometers, which is approximately two orders of magnitude smaller than the diffraction-limited resolution of conventional optical microscopes (~ 200 nm). This considerable gap prevents the investigation of both structure and dynamics of nano and sub-nano scale bio-molecules. However, a rather new family of fluorescence microscopy techniques, so-called super-resolution microscopy (SRM), has revolutionized biomedical imaging by breaking the classical diffraction barrier. This field has been increasingly developing since the first development of STED microscopy [34] in 1994.

In visible optical regime and using the highest NA objectives, the highest resolution achievable, $\delta_{x,y}$, is restricted to the order of 200 nm. This resolution has been tremendously improved over the last two decades up to the order of one nanometer using various SRM techniques which can be divided into two main branches: localization-based methods such as stochastic optical reconstruction microscopy (STORM), photo-activated localization microscopy (PALM), etc., or optics-based methods like structured illumination microscopy (SIM) or image scanning microscopy (ISM).

The first group, also so-called single-molecule localization microscopy (SMLM), aims to precisely localize single emitters based on photo-physical properties of fluorophores. Here, the accuracy of the position scales with \sqrt{N} where N denotes the number of photons collected. For a review of different SRM methods and applications in cell biology, see Refs. [35, 36].

2.5.1 Principles of optics-based SRM

Optics-based SRM like SIM can be well-explained by the Moire effect where typically an overlay of two periodic patterns with slightly different frequencies or orientations yield a new interference pattern which has a lower frequency than the initial interfering ones [37]. Let us consider the sample as an unknown super-position of periodic structures with different frequencies and orientations and illuminate it with a known periodic structure of light array like a stripe pattern (a sinusoidal wave) instead of a homogeneous intensity distribution. Taking the Moire effect into consideration, a diffraction-limited microscope practically records 'interfered' images, which readily show downsampled (yet incomplete) high-resolution content in a lower frequency range.

In other words, acquired images are convolutions of the sample structure (unknown superimposed periodic patterns) with the excitation light patterns (known periodic patterns). One can reconstruct the fine intrinsic structure of the sample containing higher spatial frequencies by a sufficient set of recorded images, where phase and orientation of the illumination patterns have been shifted in order to sample the Fourier space of the structure adequately. The periodicity of the excitation patterns (the Moire wavelength) either has to be smaller than or ideally match the resolution limit of a microscope ($\delta_{x,y}$).

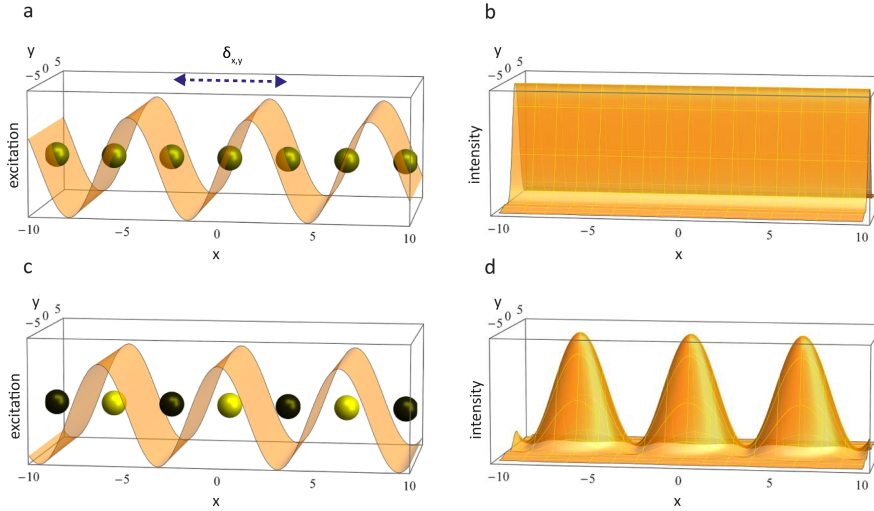


Figure 2.16: Resolution improvement obtained by scanning the sample via structured excitation patterns. (a) Equally distanced emitters excited with a sinusoidal illumination pattern with a period twice the distance between sequential emitters b) corresponding intensity of emitters shown in (a) indicating unresolved emitters, (c) shift of the illumination pattern in (a) by a distance of one period leading to proper excitation of every second emitter, (d) corresponding intensity of already resolved emitters. $\delta_{x,y}$ indicates the resolution limit of a microscope. Image is adapted from Ref. [29].

Fig. 2.16 schematically explains a simplified concept of the resolution enhancement in SIM. A periodic array of fluorophores sitting next to each other with an inter-gap distance equal to half the resolution limit is excited by a structured light with a period equal to the resolution limit (shown as the orange sinusoidal pattern in Fig. 2.16a). The resulting image is a straight intensity line on the detector, i.e., not resolving single fluorophores, which is equivalent to epi-fluorescence result Fig. 2.16b). However, a shift in the position of structured illumination (a distance of $\delta_{x,y}/4$ shown in Fig. 2.16c) leads to the excitation of only every second emitter, which in turn results in resolving them in the image plane (Fig. 2.16d). One can ensure exciting all emitters by scanning the sample with a series of such illumination patterns in different orientations.

2.5.2 Image Scanning microscopy

Likewise to the microscope PSF mentioned in section 2.3.2, OTF of a microscope is found by the convolution of the excitation OTF with the detection OTF. For example, Fourier transform of a focused excitation PSF (excitation OTF) convolved with the Fourier transform of confocal (pinholed) detection (detection OTF) renders the OTF of a confocal microscope. The pinhole size in an ordinary confocal microscope is typically selected in the order of the microscope PSF to collect most of the emission light. The lateral resolution of such a confocal microscope is almost the same as a conventional wide-field microscope. In theory, the resolution of a confocal microscope with an infinitely small pinhole is enhanced by a factor of $\sqrt{2}$ with respect to the resolution of the same microscope but with a ordinary confocal pinhole size [29, 38]. However, there is no wonder that using an infinitely small pinhole is equivalent to a huge rejection of the emission light, i.e., passing almost no signal on the camera.

In 1988, Sheppard [38] provided a theoretical work to describe how to effectively enhance the resolution of a scanning confocal microscope. He suggested to scan a sample with diffraction-limited focused excitation light and replace the typically point detector used in the confocal system with an imaging detector (camera) to collect the detection light at each scan step. In effect, each small pixel of the camera acts the role of a 'infinitely small confocal pinhole' in resolution enhancement but unlike such a pinhole, no light is lost in this approach. Considering both the excitation and detection PSFs diffraction limited, using such a wide-field collection of the scan images, one can reconstruct an image with a doubled resolution and higher contrast with respect to the microscope's resolution limit. In 2010, Müller and Enderlein realized this idea and named that image scanning microscopy (ISM) [39]. In chapter 4, we present the reconstruction process of ISM and review different existing ISM versions. To more understand the idea

behind ISM, one can consider that the diffraction-limited focused excitation beams in ISM play the same role as the structured excitation patterns in SIM.

In reconstruction of a super-resolved image in ISM, the position information of excitation spot (excitation PSF) and the corresponding position in the scanned image is the key. If the position of scan image, or equivalently, the detection PSF recorded by the camera is shifted by a distance of s with respect to the excitation PSF (Fig. 2.17), one can show that the most probable position of the ISM PSF locates at $s/2$ [39]. Detailed mathematical description of ISM theory can be found in the supporting information of Ref. [40].

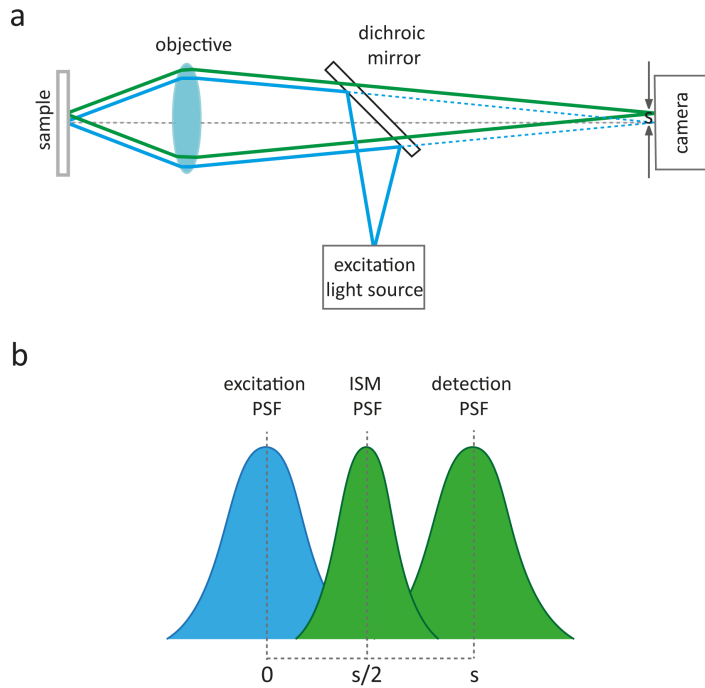


Figure 2.17: ISM working principle. (a) Excitation light is focused onto a sample where the emission light is recorded by a camera at a distance of s with respect to the position of the excitation light (shown in dashed blue line). (b) The position maxima of the product of the detection and excitation PSFs determines the position of ISM PSF which locates at $s/2$.

The resolution enhancement of an ISM image can be well described by the spatial frequency domain of the ISM image, i.e., its OTF. In principle, the OTF of a microscope is found by the convolution of the excitation OTF with the detection OTF. For example, using a confocal microscope with the assumption of the same excitation and emission wavelengths, the supporting edge of the OTF expands twofold because both the illumination and detection OTF present the same cutoff frequencies. This results in the obtaining of higher spatial frequencies existing in the sample's image [39, 40]. A similar scenario occurs for a wide-field based ISM in the lateral dimensions. In other

words, the axial extent of spatial frequencies in the case of a wide-field ISM is more restricted than those in the confocal ISM due to the lack of optical sectioning capability. Fig. 2.18a shows a lateral view of the OTF of a wide-field microscope, and Fig. 2.18b represents the same OTF but with extended support along the lateral dimension (k_x).

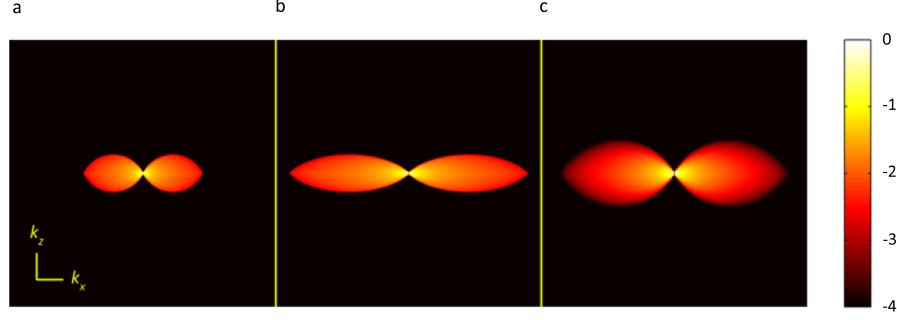


Figure 2.18: OTF comparison of wide-field and wide-field based ISM. (a) OTF of a conventional epi-fluorescence microscope, (b) same OTF as (a) with doubled spatial frequency extension along k_x , (c) OTF of ISM obtained from convolution of OTFs in (a) and (b) containing higher spatial frequencies in both k_x and k_z compared to the epi-fluorescence case (a). Image is adapted from Ref. [29].

The OTF of an ISM system (Fig. 2.18c) is the convolution of these two OTFs (Fig. 2.18a, b) along k_z . A review of theory and mathematics in detail can be found in Ref.[29]. One can write:

$$OTF_{LED-ISM}(\mathbf{q}) \sim OTF_{WF}^2(\mathbf{q}/2) \quad (2.12)$$

Where $OTF_{LED-ISM}(\mathbf{q})$ and $OTF_{WF}(\mathbf{q}/2)$ respectively denote the OTF of ISM and of wide-field (See Supporting info in Ref. [40]). As can be seen in Fig. 2.18c, theoretically under optimal condition, the support of spatial frequency in OTF of ISM is doubled in both lateral and axial dimensions compared to the OTF of wide-field. As the wide-field microscope lacks the optical sectioning capability, the wide-field based ISM also does not have this feature. However, one can set digital pinholing in image analysis on acquired emission spots to somewhat reject the out-of-focus lights [41]. Further, wide-field ISM provides higher axial resolution compared to the conventional wide-field. $OTF_{WF}^2(\mathbf{q}/2)$ denotes the OTF of a conventional wide-field microscope as a function of $q/2$, as half the maximum spatial frequencies desired in ISM.

Equivalently in the spatial domain, let us assume that the excitation PSF is centered at 0, and the detection PSF is centered at an arbitrary position s on the camera sensor. One can prove that the position of the maximum for effective PSF, i.e., the most probable position of the

light's origin locates at position $s/2$ [39]. In chapter 4, we will see that this concept also facilitates the ISM reconstruction process significantly.

MULTI-PLANE 3D MICROSCOPY

This chapter comprises four central sections: 1- Characterization and alignment of a multi-plane prism 2, 3- Realization and application of two novel microscopes based on the multi-plane prism 4- An innovative application for 3D multi-plane microscope

In the first section, I initially characterize the optical performance of the multi-plane prism in applying different optical path lengths to an input beam, which is central in understanding the next three sections. Afterward, I present in detail how to align a multi-plane detection path where such a prism is incorporated.

In the second section, I present my work in the realization of a newly-built multi-plane phase-contrast microscope. I focus on the experimental investigation of flagellar motion in the model biological system, algae *Chlamydomonas*, aiming to obtain a more comprehensive and realistic understanding of the underlying mechanism behind flagellar dynamics. To this end, we introduce a novel and fast 3D imaging system based on the synergistic implementation of phase-contrast illumination and simultaneous multi-plane detection. This project was conducted in collaboration with *Azam Gholami* at Max Planck Institute for dynamics and self-organization (MPIDS) for the preparation of the biological sample. *Sebastian Isbaner* wrote an open-access application for 3D tracking of flagella. *Jörg Enderlein* wrote a script in MATLAB for flagella contour fitting. My focus was on building and calibration of the imaging system. I performed all experiments, and assisted in the data analysis. We submit a manuscript to biomedical optics express in accordance with our results in this section.

In the third section, I establish a multi-plane 3D fluorescence microscope and exploit it as for a novel 3D particle tracking velocimetry (3D PTV) approach appropriate to study the fast dynamic of single particles in the micro-scale regime. Combined multi-plane fluorescence experimental data and 3D tracking, I obtain the imaging system's localization precision, the velocity vectors, and the streamlines of the individual particles that follow the *Marangoni* flow inside a binary mixture of liquids in 3D. This project was conducted in collaboration with Dr. *Stefan Karpitschka* and *Olinka Ramirez Soto* at Max Planck Institute for dynamics and self-organization (MPIDS) for consulting results and the preparation of the sample.

In the fourth section, I explain the experimental realization of an instant 3D 3-color epi-fluorescence microscope. I show how to calibrate and incorporate such a system and employ it in volumetric fluorescence imaging of biological samples labeled with multiple fluorophores. Lastly, I discuss its potential capabilities and developments. A manuscript has been prepared presenting the results of this section.

3.1 CHARACTERIZATION AND ALIGNMENT FOR A MULTI-PLANE PRISM

3.1.0.1 *Characterization of the optical paths in multi-plane prism*

As described in chapter 2.4, a cascade of beam splitters associated with multiple adjusted mirrors enables the simultaneous rendering of eight focal planes in two sets of four neighboring images [15].

Marcel Leutenegger elegantly designed a single piece of glass composed of three cemented prisms which does all the three jobs mentioned at once, i.e., splitting light into multiple paths, applying a certain shift in their optical path length, and directing them into cameras [19].

Here, I characterize the quantitative magnitude of the optical path and OPDs obtained by such a prism. It is made of fused silica and is constructed from three sub-components, each with a particular thickness Fig. 3.1a. More detailed information about the prism design, material, and manufacturer can be found in the supplementary information of Ref. [19]. The interface section of the prism splits an incident light equally into two beams: 50% reflected and 50% transmitted. The inner coating surfaces of the peripheral faces of the prism, indicated as reflector 1, 2, and 3 in Fig. 3.1b, reflect any incident light back inside the prism. As a result, an input beam is split into 2×4 output beams. In detail, the thickness of sub prisms shown inside the colorful dashed lines in Fig. 3.1b are $w = 13.65$ mm for the blue trapezoid, $w + d/\sqrt{2}$ for the red trapezoid and $w - d/\sqrt{2}$ for the yellow parallelogram where $d = 3.32$.

Moreover, these thicknesses are chosen in such a way to provide a lateral distance of d between the output neighboring image planes (Fig. 3.1b). This in turn yields eight distinct but equally distanced optical paths.

Fig. 3.1d depicts the optical path of the eight beams where the plane numbers are ordered in accordance to the optical path length from the longest path (path1) to the shortest path ((path8)).

Given sizes, one can calculate the optical path of each individual image plane starting from the point 'A' highlighted in red in Fig. 3.1c.

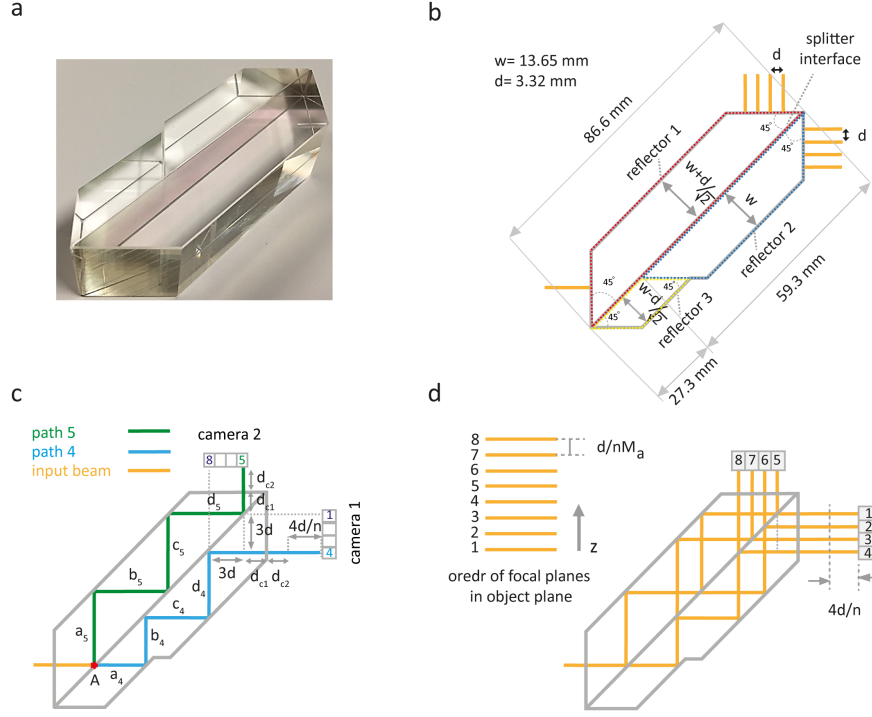


Figure 3.1: Multi-plane prism design. (a) photo of the custom-built prism, (b) sub-components of the prism as two trapezoid prisms highlighted in red and blue dashed sides as well as a parallelogram prism shown in yellow dashed sides respectively, with thicknesses of $w + \frac{d}{\sqrt{2}}$, w , and $w - \frac{d}{\sqrt{2}}$ where $w = 13.65 \text{ mm}$ and $d = 3.32 \text{ mm}$. The output beams are spaced laterally by d . (c) Path of image planes 4 in blue and 5 in green. The red point 'A' is where the input beam is split for the first time inside the prism. Path 4 is the sum of sub-paths $a_4, b_4, c_4, d_4, 3d, d_{c1}, d_{c2}$, and $\frac{4d}{n}$ and the sum of $a_5, b_5, c_5, d_5, d_{c1}$ and d_{c2} gives the length of path 5 starting from the point A to the surface of camera chips. a_4 and b_4 denote the same length as hypotenuses of a right triangle with leg's length of $w - \frac{d}{\sqrt{2}}$. Similarly, the same holds for c_4 and d_4 with a leg's length of w as well as a_5, b_5, c_5 , and d_5 with leg's length of $w + \frac{d}{\sqrt{2}}$. Camera 1 is shifted with respect to its focal plane by a distance of $\frac{4d}{n}$ where n is the refractive index of the prism. d_{c1} denotes the same length in both paths 4, 5 inside the prism. Likewise, d_{c2} is the distance (in air) from the splitter's surface to the in-focus camera chip position, the same for both paths. (d) The path of all eight beams inside the prism are numbered according to their height from a surface. $\frac{d}{nM_a}$ is the inter-plane distance in the sample plane where M_a denotes the axial magnification of imaging system.

For the path of plane 4, P4, and plane 5, P5 depicted in Fig. 3.1c we write:

$$P4 = \frac{1}{n}(a_4 + b_4 + c_4 + d_4 + 3d + d_{c1}) + d_{c2} + \frac{4d}{n} \quad (3.1)$$

$$P5 = \frac{1}{n}(a_5 + b_5 + c_5 + d_5 + d_{c1}) + d_{c2} \quad (3.2)$$

where n is the prism material's refractive index. Considering the Pythagorean relation for a right triangle, one can write:

$$a_4 = b_4 = \sqrt{2}(w - \frac{d}{\sqrt{2}}) \quad (3.3)$$

$$c_4 = d_4 = \sqrt{2}w \quad (3.4)$$

$$a_5 = b_5 = c_5 = d_5 = \sqrt{2}(w + \frac{d}{\sqrt{2}}) \quad (3.5)$$

By substitution and a bit of simplification we have:

$$P4 = \frac{4\sqrt{2}w}{n} + \frac{5d}{n} + \frac{d_{c1}}{n} + d_{c2} \quad (3.6)$$

$$P5 = \frac{4\sqrt{2}w}{n} + \frac{4d}{n} + \frac{d_{c1}}{n} + d_{c2} \quad (3.7)$$

For the OPD between two sequential paths P4 and P5 we have:

$$P4 - P5 = \frac{d}{n} \quad (3.8)$$

$$(3.9)$$

Similarly, one can calculate the length for other paths including the longest path, i.e., P1 and the shortest path, P8:

$$P1 = \frac{4\sqrt{2}w}{n} + \frac{d_{c1}}{n} + d_{c2} + \frac{8d}{n} \quad (3.10)$$

$$P8 = \frac{4\sqrt{2}w}{n} + \frac{d_{c1}}{n} + d_{c2} + \frac{d}{n} \quad (3.11)$$

Which indicates the maximum OPD among planes equal to $\frac{7d}{n}$ in the image plane which corresponds to the maximum axial range obtainable in the FOV. Respectively the inter-plane distance in the object plane equals to $\frac{d}{nM_a}$ where M_a denotes the axial magnification of imaging system (Fig. 3.1d).

Four of the light beams exit the beam-splitter prism in a direction parallel to the incident light in 'A', and four exit the prism in a perpendicular direction. Each set of four beams is imaged onto a separate camera in such a way that the images of the different focal planes are positioned next to each other on the camera chip. The rectangular field stop aperture positioned at the focal plane of the microscope

tube lens adjusts the field of view size and prevents any overlap between adjacent images on the 4 Megapixel orca flash 4V2 sCMOS cameras with a pixel size of $6.5\ \mu\text{m}$. Thus, the width of four neighboring image planes (with a 3.32 mm lateral distance in between) nearly matches the width of the sCMOS camera sensor chip.

More detail about the multi-plane prism can be found in section 6.2 in the supplementary information of Ref. [19].

3.1.0.2 *Alignment of the multi-plane detection in a non-fluorescent microscope*

Step 1: After the alignment of the *Köhler* illumination is ensured (detailed in Appendix section B.1), a calibration grid array (R1L3S3, Thorlabs) is brought onto the focus of a low magnification objective while looking it through the microscope's eyepiece. With a low magnification objective, one can easier find the approximate focal plane of the tube lens.

Step 2: Afterwards, the light path is directed onto an output of the microscope. We direct the detection light to the left port of an IX71 Olympus microscope. A tube lens is incorporated inside the microscope body, which creates an intermediate image of the sample at a $\sim 102\ \text{mm}$ distance with respect to the microscope frame (Fig. 3.2). For this microscope, the output beam propagates with a $\sim 84\ \text{mm}$ height from the optical breadboard. One should mark the focal plane position.

Step 3: Next step is to adjust the position of relay lenses RL1 and RL2. To do so, first, we screw a microscope mount adapter (U-CMAD3, Olympus) to the left port of the microscope and screw an adjustment iris diaphragm to it in order to adjust the opening of the output beam. The opening is set to ~ 1 to $2\ \text{mm}$ to easily check whether the output beam of each newly placed optical element is telecentric. After the telecentricity is ensured, the adjustment iris diaphragm is removed from the light path. Next, the first relay lens is placed at a distance equal to its focal length (f_{RL1}) from the already-marked focal plane of the tube lens. The second relay lens is positioned at a distance of $f_{RL1} + f_{RL2}$ from the lens RL1, to provide a telescope system (Fig. 3.3). The inter-distance of relay lenses is fixed. Afterward, the intermediate image, i.e., the focal plane of the tube lens, is imaged using an accessory camera and the telescope system. The precise position of the telescope system from the tube lens focal plane is ensured when the intermediate image is sharply imaged on the camera.

Step 4: The next step is to align the position of the multi-plane prism. Again, an iris diaphragm is positioned just in front of the lens RL2, and an adjustment mirror (minimally with a 2 inch size of reflecting surface) is placed in a distance from the iris where one can later

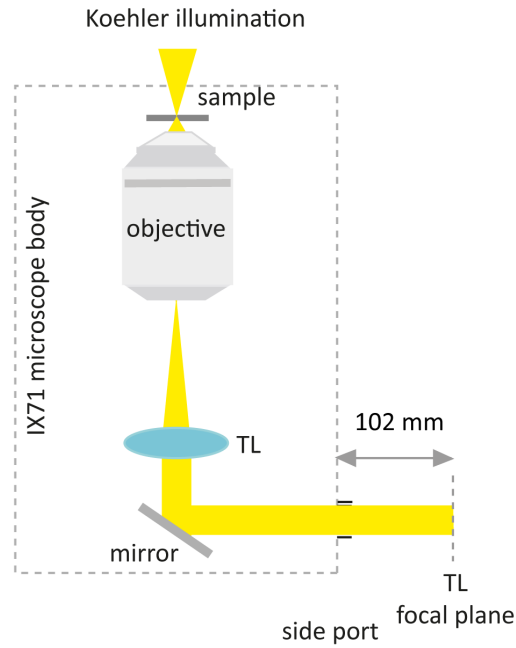


Figure 3.2: Finding the focal plane of the tube lens in a IX71 Olympus microscope.

place the prism safely in between. The beam is orthogonal to the mirror when the reflected beam matches the iris opening. Afterward, the prism is positioned between the iris and the mirror so that the beam roughly hits the center of the prism's entrance surface (Fig. 3.4). One should see a number of reflecting beams on the diaphragm where there is one set of four neighboring beams, brighter than the others, reflected on the iris diaphragm. The perpendicular orientation of the prism surface with respect to the incidence beam is ensured by adjusting its inclination such that the four beams match the iris opening. Afterward, the iris and mirror are removed. Next, sCMOS cameras (camera 1 and camera 2) are mounted on xy translation stages and are positioned in front of the prism's outputs.

Step 5: A rectangular field aperture is placed at the focal plane of the tube lens, and its opening is adjusted so that there will be no overlap between the adjacent image plane on the cameras (Fig. 3.5).

Step 6: Displace the cameras so that the middle image planes are at the focus (Fig. 3.6).

Finally, the camera 1 is displaced by a distance of $4d/n$ with respect to its focus position. This configuration (called sequential configuration) renders a d/n OPD between the consecutive image planes. The inter-plane distance and brightness of image planes are calibrated by scanning fluorescent beads described in detail in section 3.2.2.2. Since the prism's geometry and refractive index is fixed, the inter-plane distance can be adjusted only by changing the detection system's magnification, which is governed by the overall magnification of the objec-

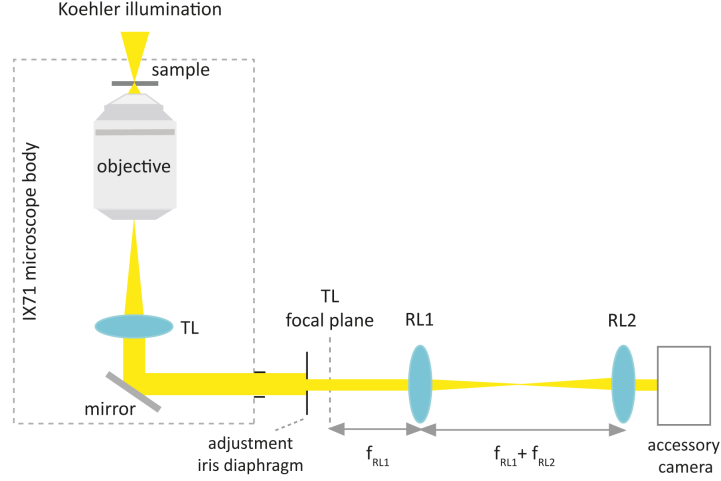


Figure 3.3: Adjustment of the relay lenses.

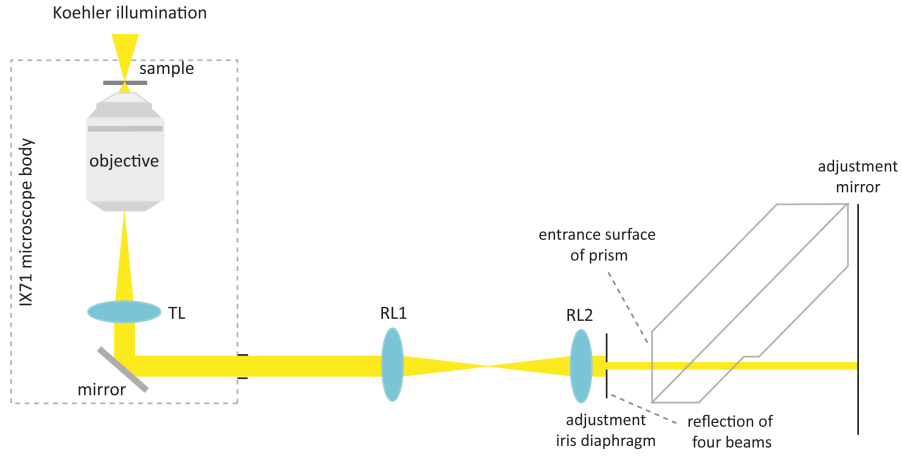


Figure 3.4: Adjustment of the position of multi-plane prism.

tive, tube lens, and relay lenses $L1$ and $L2$.

In an alternative configuration, while the camera 1 is kept at its focus position, one can only displace the camera 2 by a distance of $d/2n$ with respect to its focus position. Such configuration provides an inter-plane distance of $d/(2nM_a)$ between the focal planes, i.e., half the corresponding value obtained in the previous configuration. This is called an inter-laced configuration, which is suitable for doubling the sampling rate of the axial range while it equivalently gives half the axial range obtained by the $4d/n$ configuration. The inter-laced configuration is particularly suitable for low NA objectives where the axial resolution is low. Such configuration is used in the section 3.3.2.2.

Prism-based alignment of a multi-plane detection path for an epifluorescent microscope is similar to the procedure described above and can be found in detail in [42].

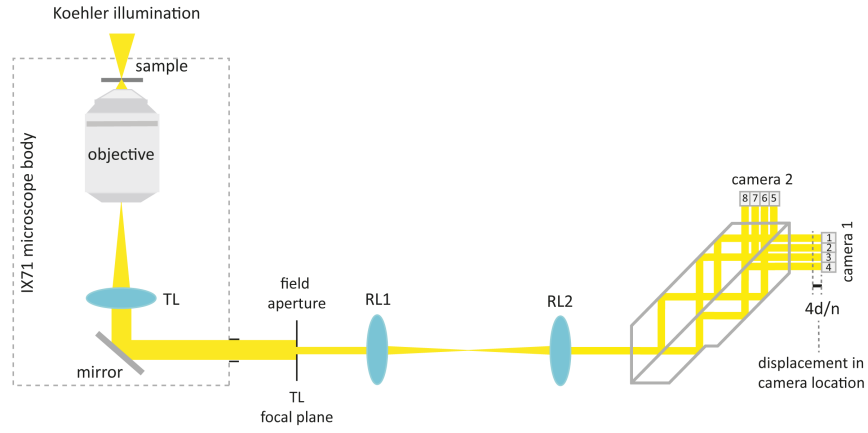


Figure 3.5: Alignment of the field aperture.

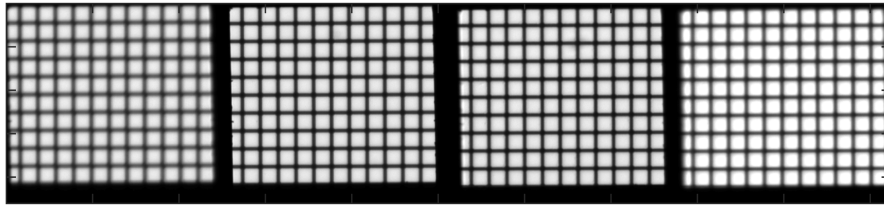


Figure 3.6: Grid array for alignment.

In the next section, we incorporate a sequential configuration in a non-fluorescent microscope. In sections 3 and 4 accordingly, we implement the inter-laced and sequential configurations for in the epi-fluorescent mode of our microscope.

3.2 OBSERVATION OF BEATING *chlamydomonas* FLAGELLA WITH
MULTI-PLANE PHASE-CONTRAST IMAGING

3.2.0.1 *Why Chlamydomonas flagella? Why multi-plane phase-contrast imaging?*

It might be of interest to the reader which specific properties of *Chlamydomonas* flagella's motion encouraged the design and realization of a new microscopic imaging technique. There is an important yet still open question in biophysics how flagella and cilia move in 3D. *Chlamydomonas* axoneme (the central cytoskeletal structure of motile flagella) exhibits a rapid motion (up to 100 Hz of beat frequency). Moreover, they show an almost planar motion when they swim close to a surface. Therefore, the fast dynamics and the small out of plane components of motion imply that one cannot sufficiently fast follow the sample's dynamic in 3D using the available microscopic techniques.

Studying such motion does not necessarily require a fluorescence microscope because one can efficiently detect the axonemes using the already mentioned non-fluorescent techniques like the phase-contrast or DIC microscopy. However, most of these techniques provide only a two-dimensional image. As mentioned in chapter 2, on one hand, the DIC microscope gives a pseudo-3D picture from a sample of interest. However, such a DIC image, i.e., the visualized optical phase distribution, cannot be easily inverted to quantitative information about the axial coordinates, i.e., the z-coordinates of different parts of a sample.

On the other hand, conventional phase-contrast microscopy inherently provides an image only in 2D. However, it is typically a convenient technique to obtain a high contrast image and is not limited to short acquisition time like those in fluorescence microscopy, which involves photo-bleaching and photo-toxicity. Further, as already mentioned in chapter 2, generally, a phase-contrast image yields a higher contrast image than a DIC image in particular for samples with non-complex structures like bare axonemes.

As a result, we decided to combine a phase-contrast microscope (providing high contrast and straightforward imaging over a long time) with a multi-plane microscope (providing volumetric detection with high temporal resolution). Meanwhile, *Chlamydomonas* axonemes are excellent test samples for checking the capability of our multi-plane phase-contrast microscope. This is because *Chlamydomonas* axonemes require relatively simple procedures for isolation and reactivation as compared to sperm cells.

3.2.1 Introduction

Cilia and flagella, filamentous arms attached to cell bodies, exist in prokaryotic cells, eukaryotic cells and also in tissues of large animals. In general, cilia are shorter in length but more abundant on cell surfaces compared to flagella. However, they both have very similar functions.

Axoneme, as the core structure in cilia and flagella, is a highly conserved structure. It is composed of two central single microtubules, and nine peripheral microtubule doublets (MTDs) as depicted in Fig. 3.7a, see Ref.[43, 44] for structural details. Fig 3.7.b shows a cross section of the axonemal structure which has a diameter of ~ 200 nm. MTDs are decorated with an asymmetric distribution of dynein motor proteins [45] which is thought to be the cause of the asymmetric activity along MTDs [46]. Dyneins are categorized in inner and outer arms each with a distinct function [47]. See Ref.[48] for mechanics of motor proteins. Nexins (repetitive proteinous linkers) connect neighboring MTDs and radial spokes are spacers between MTDs and the central pair of microtubules.

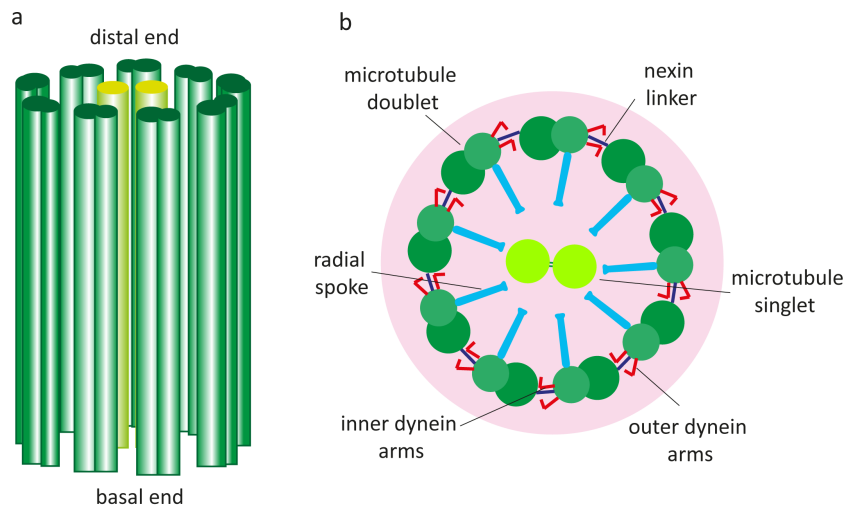


Figure 3.7: Axonemal inner structure. (a) the longitudinal view of axonemal configuration made of nine microtubule doublets (light green) in addition to a pair of microtubule singlet (light green), (b) the cross section of axoneme containing nexin linker (blue), dynein (red) and radial spoke (cyan) coupled to microtubules.

Both the radial and longitudinal polarities of the axonemal structure introduce an inherent chirality of its structure. This can be seen by the orientation of the dynein-decorated MTDs around the central MTD [45].

Cilia and flagella play crucial roles in a variety of biological phenomena such as cell locomotion, fertilization or the generation of micro-scale flows over a cell body or a tissue surface.

Ciliary carpets on the respiratory epithelia are life-important, e.g., in mucociliary clearance of the airways of large animals [49–51] and in active fluid transport in the brain [52, 53]. It has been shown that the motion of nodal cilia is necessary for correct embryo development [44, 54, 55].

In chemotaxis, flagella not only play the role of a sensory element (sensing the chemical cues) but also as a chemical actuator to propel a cell, e.g., a sperm cell, towards an egg. In detail, receptors on sperm flagella sense the chemical attractant released by an egg. This sensing activates a series of signaling processes which lead to a release of Ca^{2+} ions to control flagellar motion. [56, 57]. Flagella-attached sperm cells of different species are shown in Fig. 3.8, adapted from [58] with permission.

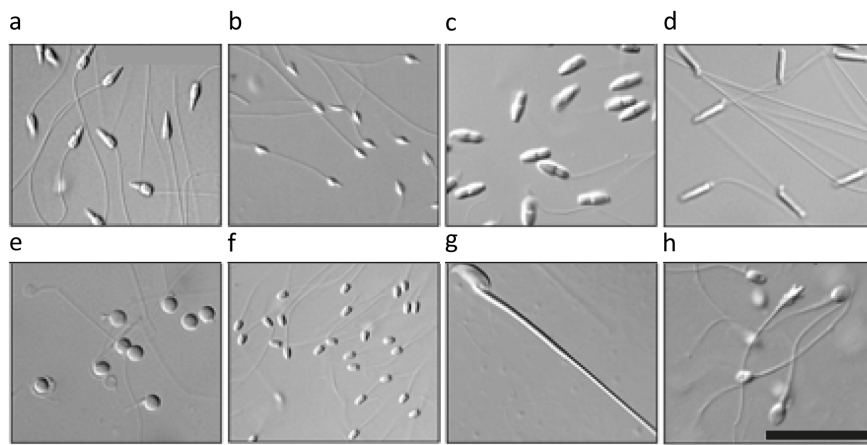


Figure 3.8: DIC image of uni-flagellate sperm cells of several species with the same magnification. (a) sea urchin (*H. pulcherrimus*), (b) tunicate (*C. intestinalis*), (c) sea snail (*Ompphalius pfeifferi*), (d) Sturgeon (*Acipenser baerii*), (e) fresh water fish (*Barbus barbus*), (f) puffer fish (*Takifugu niphobles*), (g) mouse (*Mus musculus*) and (h) human (*Homo sapiens*). Flagella images exhibit a lower phase contrast as compared to sperm heads due to their smaller thickness. Scale bar indicates length of 20 μm [58].

Altogether, understanding of the motion mechanism and dynamics in motile flagella and cilia is of paramount importance.

One of the most prominent examples of a flagellum-based motile system is the single cellular bi-flagellate green algae *Chlamydomonas reinhardtii* which has been extensively studied to learn about the flagellar motion

Chlamydomonas Reihardtii

Chlamydomonas Reihardtii has attracted a huge attention since the middle of the last century [59]. It is a uni-cellular micro-organism numer-

ously existing in water and damp soil, with a typical diameter of $\sim 10\ \mu\text{m}$ associated with two cell-bound flagella (Fig. 3.9.a).

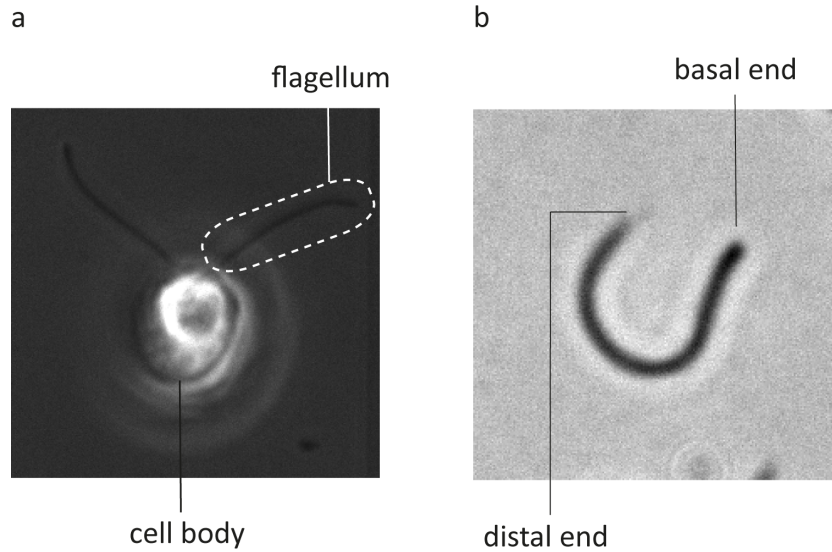


Figure 3.9: *Chlamydomonas*. (a) phase-contrast image of *Chlamydomonas* alga. One flagellum is highlighted in the white dashed loop. (b) an isolated flagellum from cell body with basal end and distal end indicated.

An isolated *Chlamydomonas* axoneme is shown in Fig. 3.9b. The basal and distal end of the axoneme can be distinguished by looking at the thickness of the two ends. The basal end of the axoneme is slightly ($\sim 10\%$) thicker than its distal end [60]. Moreover, in an intact beating flagellum, curvature waves typically propagate from the basal towards the distal end. This property can be used to determine axoneme orientation.

The grown flagella of *Chlamydomonas*, have a quite stable length [61, 62], between $10\ \mu\text{m}$ and $12\ \mu\text{m}$. This length has recently been shown to be the optimal length for efficient mechanical locomotion [63].

Due to the technical simplicity of culturing *Chlamydomonas*, and the ease of genetically modifying this organism, *Chlamydomonas* has become one of the best studied model organism in particular for investigating phenomena such as photosynthesis [64, 65], phototaxis [66, 67] or flagellar-driven motion [68].

Similar to many types of micro-alge, *Chlamydomonas* is able to produce organic compounds and oxygen by photosynthesis. Due to its unicellular nature, reproduction capability in both sexual [69] and asexual ways [70] and its capability to flexibly adapt to various environmental factors such as light intensity or availability of nutrients, *Chlamydomonas* is able to rapidly reproduce and grow.

Chlamydomonas flagella simultaneously rotate the cell body counter-clockwise (ccw) around its long axis (with up to 2.5 Hz when propelling forward [71]). The flagellar beating frequency is in the range

of 20 to 60 Hz. It has been shown that the axonemal beating shape can be decomposed into a time-averaged axonemal shape (static mode) and time-dependent beat (dynamic mode) [72, 73]. The dynamic mode propels the axoneme whereas the static mode leads to the well-known asymmetry in both beating and swimming direction of wild type axoneme [73–76].

A *Chlamydomonas* flagellum swims in a breast stroke manner using both in-phase and stochastic flagellar beats [43, 77, 78].

Most of the available theoretical models describe flagellar motion in 2D, despite the fact that flagellar motion is generally three-dimensional. In particular, 3D motion has been reported for various micro-swimmers such as human sperm [79–82], bull sperm [83, 84], sea urchin sperm [85, 86], the alga *Euglena*'s flagellum [87], or *P. berghei* microgametes [88].

Among the existing 3D models [89–93], it has been suggested that torques generated by dynein motor proteins give rise to internal twist and external bending of the axoneme [91, 93]. Axonemal twist can potentially result in out of plane component when the whole axonemal structure bends.

Furthermore, in a closed observation chamber, *Chlamydomonas* axonemes will accumulate at the top and bottom surfaces, which strongly indicates that their motion is intrinsically three-dimensional [60].

Despite the 3D observation of flagellar motion in the mentioned micro-swimmers, nearly all experimental studies of *Chlamydomonas* axoneme motion are purely two dimensional. This is partly due to the fact that *Chlamydomonas* axonemes are almost three to five times shorter and faster (~ 50 Hz beat frequency) than flagella of typical sperm cells. Therefore, a real-time 3D investigation of flagellar motion requires a rapid imaging technique in three dimensions.

Several techniques have been developed for rapid 3D optical microscopy. Among them are computational quantitative phase imaging (QPI) [7, 8, 94], holographic methods [9, 10, 95], phase modulation methods [96, 97], or methods that control the phase delay with phase modulators [98]. Alternatively, by recording two or more images in different focal planes [99–101], optical phase information can be retrieved without interference but rather via the so-called transport intensity equation (TIE). Another method is light field microscopy which employs micro-lens arrays associated with wide-field imaging to acquire single-shot data that can be reconstructed to render 3D images via inverse filtering (3D deconvolution) [12, 102].

However, all these techniques come at the price of either computationally expensive data processing (QPI techniques), technical complexity (multi-plane imaging with diffractive grating), setup instability and image reconstruction ambiguity (holographic techniques), resolution

inhomogeneity (light field microscopy), or low signal-to-noise ratio (SNR) all techniques.

As already mentioned in the chapter 2, recently, a new family of multi-plane fluorescence microscopes has been developed for parallel and simultaneous imaging at multiple focal planes. Here, we combine such a multi-plane microscope using the multi-plane prism with a conventional phase contrast microscope to enable rapid, label-free, robust and easy-to-use 3D imaging of flagellar motion.

3.2.2 *Methods*

3.2.2.1 *Multi-plane phase-contrast imaging*

The combination of a multi-plane microscope with the conventional phase-contrast imaging enables rapid, label-free, robust and easy-to-use 3D imaging of flagellar motion. Our multi-plane phase-contrast microscope allows for the simultaneous recording of eight axially stacked images with several hundred frames per second. In contrast to QPI or light-field imaging, our system does not require any reference image for image reconstruction, and it provides real-time 3D observation of rapidly moving samples with excellent SNR in a robust and straightforward manner. Furthermore, most of existing quantitative phase imaging techniques require complex and time-consuming image analysis and filtering. Taking this all into consideration, our proposed imaging system meets the technical demands.

A schematic of the proposed multi-plane phase-contrast microscope is shown in Fig. 3.10. I established this system on a commercial IX71 microscope from Olympus. The collimated light of a white-light source (Halogen Lamp U-LH100L-3) is sent through a condenser annulus (IX-PH3, Olympus) and focused by a condenser lens (IX2-LWUCD, Olympus) onto the sample in *Köhler* illumination (see section B.1 for procedure of *Köhler* illumination and phase-contrast alignment).

Scattered and transmitted light are collected by a Zernike phase-contrast objective (UPLFLN 60XOIPH, Olympus, 1.25 N.A., 60 \times magnification) which shifts the phase of the transmitted light by $-\pi/2$ with respect to the scattered light resulting in destructive interference between scattered and non-scattered light. This provides a phase-contrast image when focused by the tube lens onto a camera. Before imaging, a multi-plane prism splits the collected light into eight beams with different optical path lengths corresponding to eight different focal planes in the sample. Setup specifications can be found in section B.2.

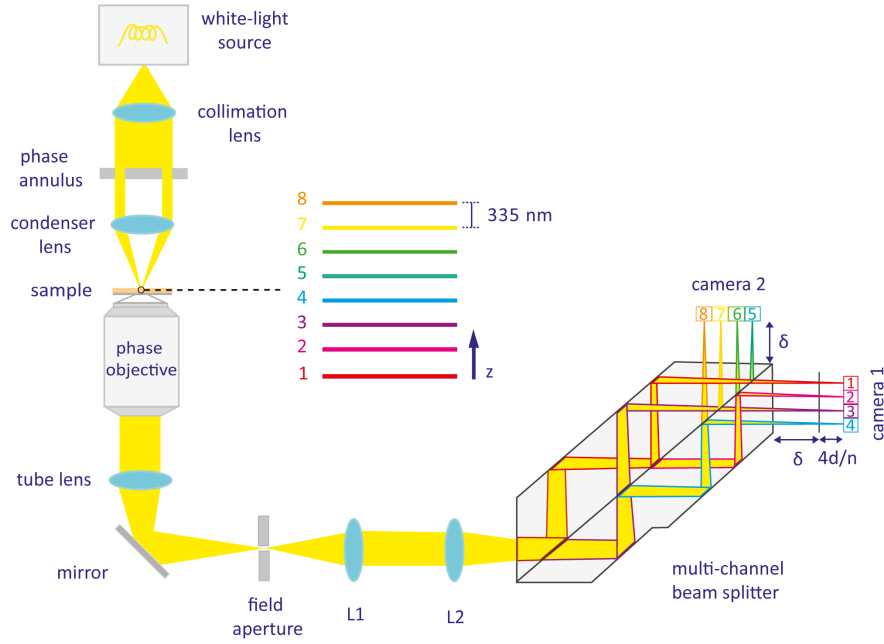


Figure 3.10: Schematic of the multi-plane phase-contrast microscope. Light from a white-light source is sent through an annular aperture and focused onto the sample for high-angle illumination. Transmitted and scattered light are collected with a Zernike phase-contrast objective (oil immersion, $60\times$ magnification, 1.25 N.A.), focused by the tube lens through a slit aperture, and then sent through two relay lenses $L1$ and $L2$ (that increase magnification to $80\times$) towards a custom-made multi-plane beam splitter. This splitter generates eight laterally shifted image replicas with increasingly longer optical path length, corresponding to eight different focal planes in the sample, shown with color-coded lines. These eight images correspond to eight focal planes in the sample separated by 335 nm (in aqueous solution), and they are recorded by two sCMOS cameras. The slit aperture limits the field-of-view and prevents overlap between neighbouring images on the cameras. Camera 1 is in distance of δ and camera 2 is positioned by distance of $\delta + 4d/n$ from splitter output where d is interleaved lateral distance between neighboring planes and n is refractive index of beam splitter material.

3.2.2.2 Setup calibration

As mentioned in section 3.1.0.1, the prism was designed to render four adjacent channels with interleaved lateral distance of $d = 3.2$ mm in between which fits in size to width of the 13.3×13.3 mm pixel area of our sCMOS detector (ORCA-Flash 4.0 V2, Hamamatsu). Considering focus of the camera 1 as the reference with distance of δ from the prism output, the camera 2 is displaced from the focus by a distance of $4d/n \sim 9$ mm where $n = 1.46$ is the refractive index of the prism material. In other words, with respect to the prism outputs, camera 2 is positioned by the mentioned distance farther than camera 1.

This allows one to obtain an OPD of $\sim d/n$ between sequential planes. To calibrate this system, we performed z -scans of immobi-

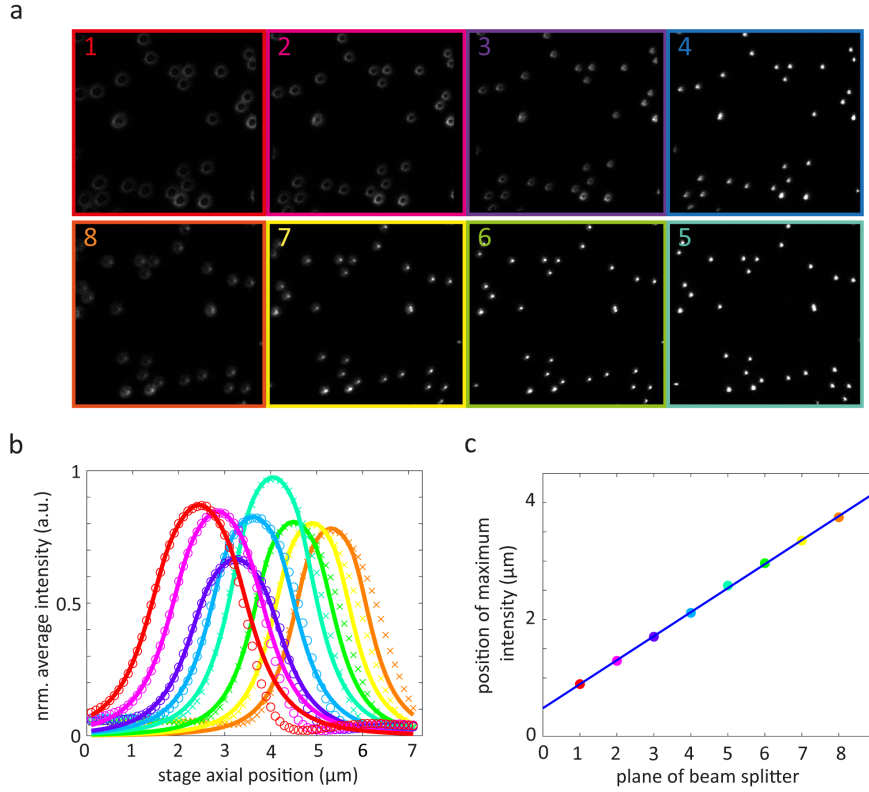


Figure 3.11: Inter-plane distance and brightness calibration. (a) Example of the eight images of fluorescent beads recorded by the multi-plane wide-field microscope. In this example, beads are in focus in nominal plane #4 (b) Normalized average intensity in each image plane as a function of axial scan position (for axial scan steps of 100 nm). Crosses (for camera 1) and open circles (for camera 2) represent measured data, solid lines are Gaussian fits. (c) Linear fit of positions of intensity maxima from panel (b). The fit yields an average inter-plane distance of ~ 430 nm (for oil immersion).

lized green fluorescent beads of 200 nm diameter (FluoSpheresTM Carboxylate Micro-spheres, 0.2 μm, yellow green fluorescent (505/515), Thermo Fisher Scientific) that were spin-coated on a glass coverslide, using an oil immersion phase objective (UPLFLN 60XOIPH, 1.25 NA, Olympus), a tube lens and the relay lens system as shown in Fig. 3.10, that totally provide a lateral magnification of $80\times$. Fluorescence excitation was done at 470 nm with a LED, and the objective was moved over an axial scan range of 7 μm with 100 nm step size.

Fig. 3.11a displays multi-plane image acquisition of fluorescent beads at one z-scan step. A plot of the total intensity recorded in each of the eight planes as a function of axial position of the objective together with Gaussian fits are shown in Fig. 3.11b. The area under each curve is the relative amount of light that is recorded in each of the eight channels. These numbers, $\epsilon(\text{plane \#})$, are required later for correcting the slight brightness variations between different planes. A linear fit of the position of their maxima as a function of axial posi-

tion of the objective, Fig. 3.11c, yields an average inter-plane distance of ~ 430 nm.

The corresponding inter-plane distance in water shrinks by a factor of 0.78 due to the refractive index mismatch between immersion oil and water, as numerically calculated using the full wave-optical theory developed by Wolf and Richards[103, 104]. The result of these calculations, Fig. 3.12, shows how the axial center of the PSF in water (blue line) deviates from its position it would have in glass/oil (red line). Thus, our multi-plane system allows us to record a sample volume of $40\text{ }\mu\text{m} \times 40\text{ }\mu\text{m} \times 2.4\text{ }\mu\text{m}$ in an aqueous medium with almost equally spaced inter-plane distance of ~ 335 nm.

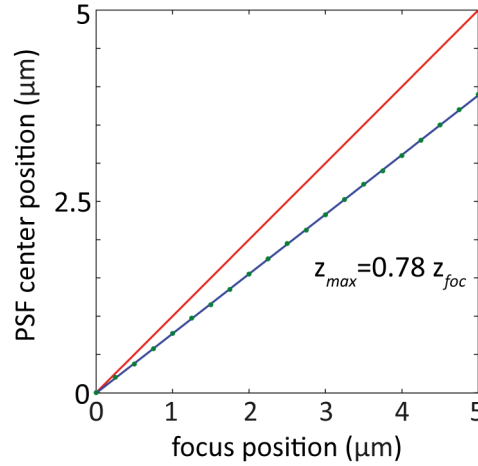


Figure 3.12: Relative shift of focal plane position in water (blue line) with respect to oil (red line). Open circles are the result of a wave-optical calculation of imaging in water, the blue solid line is a linear fit to this result. It shows that close to the glass interface, we still find a linear relationship between focal plane position and the objective's axial position, but inter-plane distance in water is by a factor of 0.78 smaller than in oil.

3.2.2.3 Spatial resolution of the imaging system

Lateral and axial resolution of the optical system (at emission wavelength of $\lambda = 520$ nm) was determined by measuring the full-width-at-half-maximum (FWHM) of single bead images. Fig. 3.13a represents image intensity of fluorescent bead at focal plane and Fig. 3.13b is the view of scanned intensity along the optical axis (axial view of PSF). Optical resolution is determined by measurement of the FWHM of 1D Gaussian fit to the experimental data points in both lateral (324 nm) and axial dimensions (1135 nm) shown respectively in Fig. 3.13c, d. Chosen axial magnification ($M_{ax} \sim M_{lat}^2 = 6400 \times$) fulfills the Nyquist-Shannon's sampling criterion[105]. In regard of depth sampling in imaging system, this criterion indicates that inter-plane distance should not surpass half the axial resolution.

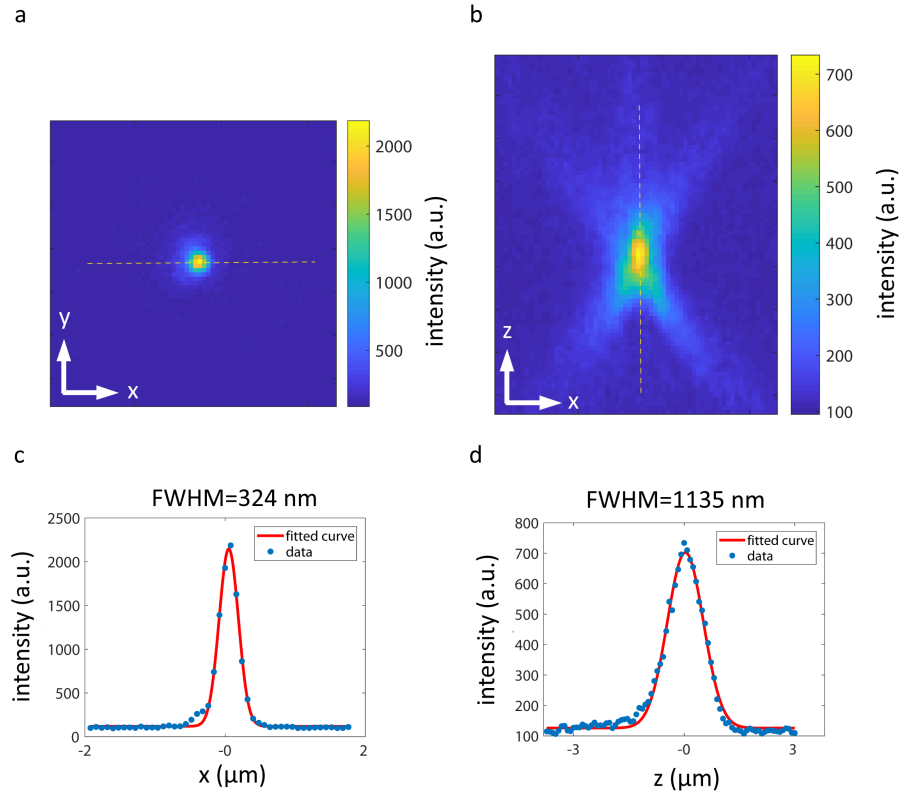


Figure 3.13: spatial resolution of multi-plane phase-contrast imaging system. (a) image intensity of fluorescent bead at focal plane #4 (b) xz axial view of intensity along scanned planes (c) intensity plot along the yellow dashed line highlighted in (a) and corresponding Gaussian fit (d) intensity plot along the dashed line highlighted in (b) and corresponding Gaussian fit.

3.2.2.4 Sample preparation

Detachment and isolation of axoneme from the *Chlamydomonas* cell body [106, 107] is more straightforward than the detachment and isolation in existing flagellar-based micro-swimmers. It enormously facilitates the investigation of axonemal structure and dynamics from the level of a full axoneme down to individual microtubules. In particular, it allows one to study pure flagellar motion in a highly controlled and reproducible manner [60, 108]. Isolated *Chlamydomonas* axonemes (Fig. 3.9b) exhibit a significantly different motion properties compared to those of cell bound flagella. This is due to the different boundary conditions for the motion of isolated flagella and those attached to a cell body.

However, during a beat cycle, the shape of waveforms is very similar in both cases. This has been shown by studying the in-plane motion of cell-bound flagella confined in a micro-chamber [60]. Furthermore, isolated axonemes, rotate in a narrow layer parallel to the confining walls. This offers the possibility to study flagellar motion in great detail by simple optical microscopy without the need of mechanically

holding flagella in place with micro-pipettes or optical tweezers. As a result, isolated *Chlamydomonas* axonemes can be considered as one of the simplest and easiest to handle model systems for studying the fundamentals of ciliary motion. Below, we explain how to isolate the axonemes.

Axonemes are isolated from wild-type *Chlamydomonas reinhardtii* cells, strain SAG 11-32b. They were grown axenically in TAP (tris-acetate-phosphate) medium on a 12 h/12 h day-night cycle. Axonemes were isolated using dibucaine,[107, 109] then purified on a 25% sucrose cushion ultracentrifugation, and demembranated in HMDEK (5 mM MgSO_4 , 30 mM HEPES-KOH, 1 mM EGTA, 50 mM potassium acetate, 1 mM DTT, pH 7.4) supplemented 0.2 mM Pefabloc. The membrane-free axonemes were resuspended in HMDEK plus 1% (w/v) polyethylene glycol ($m_w = 20 \text{ kg mol}^{-1}$), 30% sucrose, 0.2 mM Pefabloc and stored at -80°C . To perform reactivation experiments, axonemes were thawed at room temperature, then kept on ice and were used for up to 1 hr. Thawed axonemes were diluted in HMDEKP reactivation buffer containing 1 mM ATP and infused into 100 μm deep flow chambers, built from cleaned glass and double-sided tape. The glass surface was blocked using casein solution (from bovine milk, 2 mg/mL) to avoid attachment of axonemes to the substrate. Detachment and isolation of axonemes presented in this thesis was done by Dr. Azam Gholami.

3.2.2.5 Data acquisition

Image acquisition by the two cameras is synchronized with an external trigger instrument. This is of critical importance when one records rapid dynamics (up to 100 Hz beating frequency) of objects to prevent any time lag among camera acquisitions. We used a digital micro-mirror device (DMD) model (DLP-LigheCrafter 6500, Texas Instruments) as the master device. Trigger signal of type 'Edge' was sent through both camera simultaneously. We selected 'Edge' mode since it allows to set the exposure time of camera by a command from the external device. The nominal imaging speed of full camera (OrcaFlash4-v2) chip with 2048×2048 pixels is 100 frames per second (f.p.s).

Imaging speed is inversely proportional to the number of rows within the region of interest (ROI) selected from camera pixels. The optimum ROI for axoneme imaging was 512×2048 pixels. We could capture maximally 272 f.p.s for the mentioned ROI which is large enough to cover swimming radius and small lateral movements of axoneme during acquisition. Setup of DMD and cameras are defined and controlled by the open-source microscopy software Micro-Manager [110]. The configured hardwares (hardware configuration wizard) and corresponding setting parameters are shown respectively in tables B.2 and B.3 in Appendix B.3

Fig. 3.14 a, b illustrate respectively, the image frames of camera 1 and camera 2 which were acquired simultaneously.

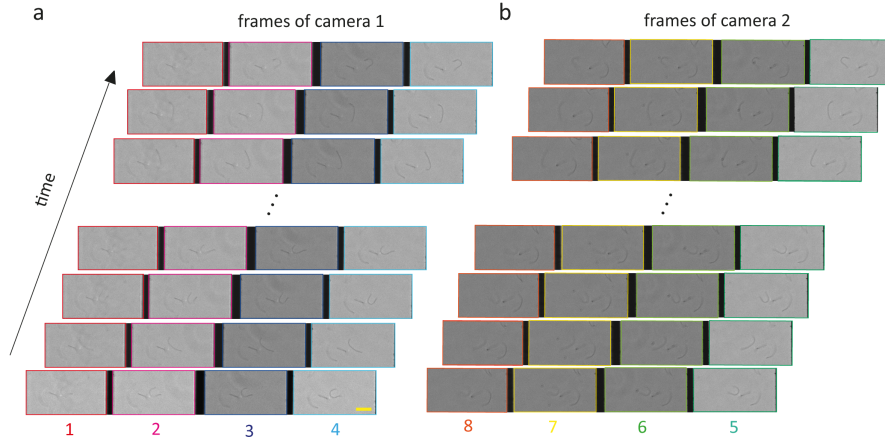


Figure 3.14: Acquisition of multi-plane phase-contrast image frames. (a) image frames of four upper planes acquired by camera 1 and (b) four lower planes acquired by camera 2, the yellow scale bar indicates $10\mu\text{m}$ of length.

Next, images of camera 1 are horizontally flipped to have the same orientation as those of camera 2. Next, they are ordered according to their height from surface which is shown in Fig.3.15a from left, (plane #5) as the low most plane toward right, (plane #1) as the upmost plane.

3.2.2.6 Image analysis from acquired raw data to a registered 3D image stack

Here, a detailed and orderly procedure of processing multi-plane data before 3D axoneme tracking is explained which are preliminary and straightforward steps. It includes slight brightness correction of planes, image inversion, Gaussian filtering, median intensity subtraction, co-registration of planes and image deconvolution.

Image inversion: All image values are inverted to negative numbers. By this, the darker axoneme structure in the images (Fig.3.14) appear as brighter features over the now darker background (Fig.3.15a). This provides contrast enhancement and better visualization of axonemes particularly after image background subtraction (Fig.3.15d).

Brightness correction: As it can be observed in Figs.3.11b and 3.14, the brightness response of different planes of beam-splitter is not exactly equal. This originates from intrinsic non-perfect equal division of light by the beam splitter ($\pm 11.7\%$ s.d. of averaged brightness). Intensity values in all eight image planes are balanced by multiplying with the corresponding weight factors $\frac{1}{\epsilon}$ achieved by calibration measurement (Fig. 3.15a).

Gaussian filtering: For noise reduction, a 2D Gaussian kernel (`imgaussfilt` function in MATLAB) with standard deviation of $\sigma = 2$ is used for low-pass frequency filtering (Fig. 3.15b).

Subtraction of median intensity: Median intensity of each plane determined over all frames (Fig. 3.15c) is subtracted from data to remove all contributions from immobile and static sources. This also increases the SNR by a factor of 3 to 5 times, depending on signal strength (Fig. 3.15d).

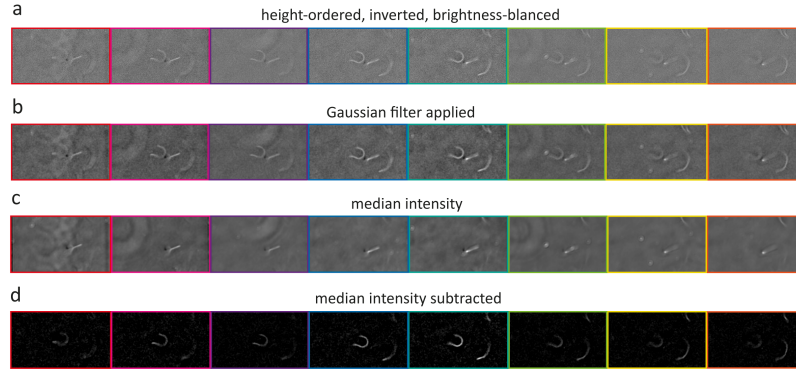


Figure 3.15: brightness balance, conversion, filtering and background subtraction. (a) Image intensities are inverted (for better contrast) and planes are ordered following their distance from the surface, from left (bottom) to right (top). Brightness values of all planes are balanced using the $\epsilon(\text{plane \#})$ values from the calibration measurement, (b) 2D Gaussian low pass filtered planes, (c) median intensity of each plane over 1980 frames, (d) median intensity subtracted image planes.

Co-registration of planes: The eight raw images have slight relative shift with respect to each other (Fig. 3.16a) which has to be registered. This is done by calculating the two-dimensional cross-correlation of each plane to one reference plane (either plane #4 or plane #5 close to the center of the stack) (Fig. 3.16b). The peak position of this cross-correlation gives direction and value of the relative shift of the considered plane with respect to the reference plane. This shift estimation is refined by repeating the procedure on Fourier up-sampled images[111]. Using these values, all images are registered to a common frame with sub-pixel precision (Fig. 3.16c,d). Non-overlapping image borders arising from registration are cropped in the final aligned image stack (Fig. 3.16d,e).

Image sharpening: The diameter of *Chlamydomonas* axonemes (~ 150 nm) is smaller than the resolution limit of the microscope. To enhance the localization of axoneme in all spatial dimensions, we perform a simple 3D deconvolution. Please note that the basal end of the axoneme is slightly ($\sim 10\%$) thicker than its distal end [60], but otherwise all axonemes show an almost homogeneous image intensity along their contour length. Thus, the shape of an axoneme can be effectively considered as a continuous one-dimensional line in three-dimensional space.

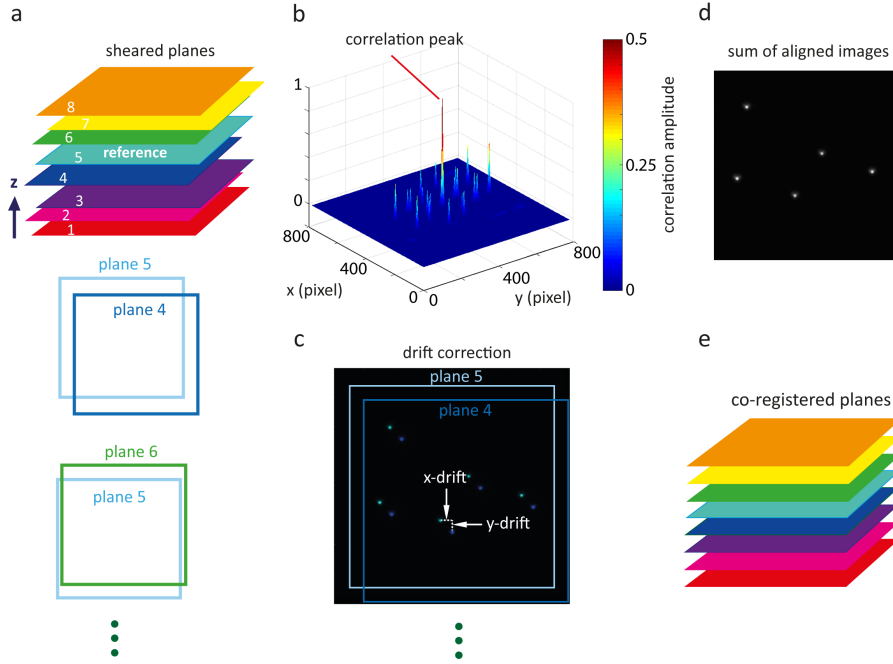


Figure 3.16: Shear correction. (a) Example of plane shearing where fifth plane from bottom is considered as the reference image. (b) Cross-correlation between one plane with reference. Peak position defines direction and value of shear between considered plane and reference plane. (c) Shear correction between plane 4 and 5. (d) Overlay of aligned planes 4 and 5. (e) Shear-corrected image stack of eight planes.

This *a priori* information can be used for a three-dimensional image deconvolution. Each frame of the multi-plane image stack is deconvolved using a pre-calculated aberration-free PSF at the interface of glass coverslide and water (Fig. 3.17a). This PSF is calculated using the full wave-optical theory developed by Richards and Wolf [103, 104] and the optical parameters of our setup (imaging wavelength λ_{peak} of 585 nm, numerical aperture NA of 1.25, image magnification of $80\times$, principal focal length of objective of 3 mm, and water and oil refractive index values of $n_{water} = 1.33$ and $n_{glass} = 1.52$, respectively).

Within a small axial distance from the surface, this PSF remains an excellent approximation of the actual ones despite refractive index mismatch, as can be seen by comparing its shape at a nominal focus position of $\sim 1.5 \mu\text{m}$ above the surface (Fig. 3.17b) with the aberration-free PSF directly at the surface (Fig. 3.17a). For deconvolution, we performed ten iterations using a 3D Lucy-Richardson algorithm [112, 113] (deconvlucy function in MATLAB) which results in a sharpening of the axoneme contour by a factor of ~ 2 in all directions. Fig. 3.17c,e presents an axoneme image maximum-projected along the optical axis and along the y -direction, respectively. Corresponding deconvolved images are shown in Fig. 3.17d,f.

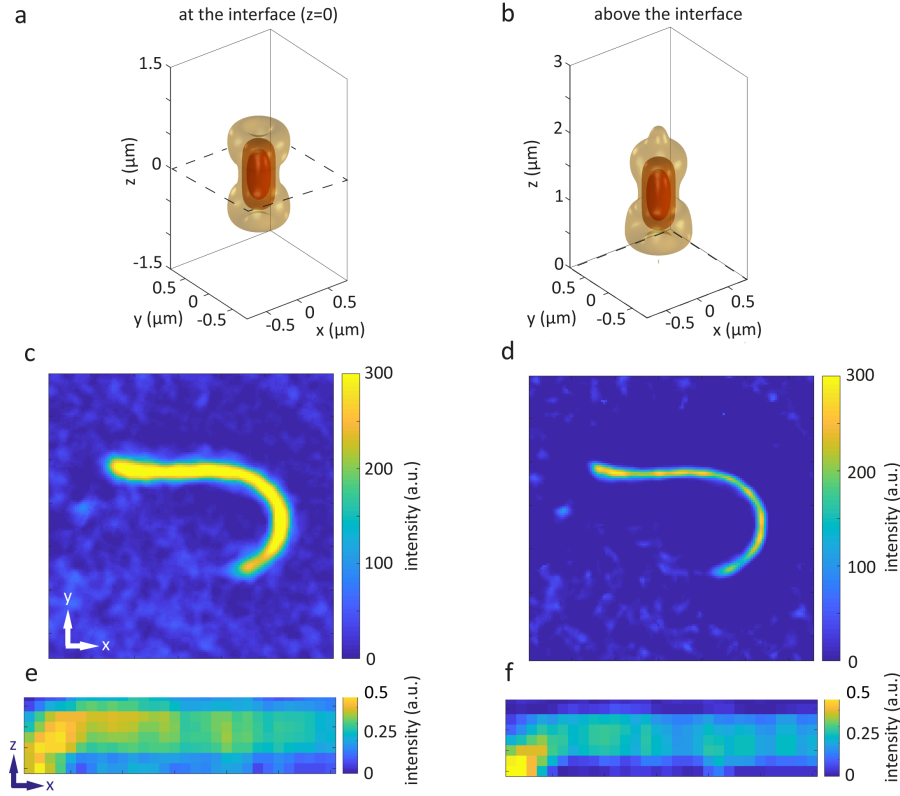


Figure 3.17: Image sharpening by 3D deconvolution. (a) Iso-surfaces (at $1/e$, $1/e^2$ and $1/e^3$ of its maximum value at the center) of a calculated PSF directly at the glass-water interface (indicated by dashed line). The same for a nominal focus position of $1.5\text{ }\mu\text{m}$ above the glass interface. Although small changes can be seen for the $1/e^3$ iso-surface, the center shape and values of the PSF are nearly identical to those of the aberration-free PSF in panel (a). (c) Maximum projection of axoneme image along the optical axis. (d) The same image after deconvolution. (e) Maximum projection of axoneme image along a lateral direction. (f) Same image after deconvolution.

3.2.2.7 3D tracking of axonemal motion

3D tracking of axoneme was performed using a costum-made tracking routine application written by Sebastian Isbaner. Starting from an already existing 2D snake tracking routine, he developed a graphic user interface application appropriate to our 3D image stack.

Tracking of an axoneme is accomplished initially by finding its 2D contour in the 2D maximum intensity projections using a gradient vector flow (GVF) snake [114, 115] (Fig. 3.18a,b). For the first frame, the user selects a region of interest that should contain only one single axoneme. Then, the user initializes the snake by drawing a polygonal line along the contour of the axoneme (Fig. 3.18c) which estimates the contour length. In the same frame, the polygonal line is interpolated to $N = 30$ points and used as a starting guess for the snake algorithm (Fig. 3.18d).

The GVF is calculated using 20 iterations and a GVF regularization

coefficient of $\mu = 0.1$. The snake is then deformed to the contour in the next frame according to the GVF where we have adapted the original algorithm by Xu and Prince for open boundary conditions [115].

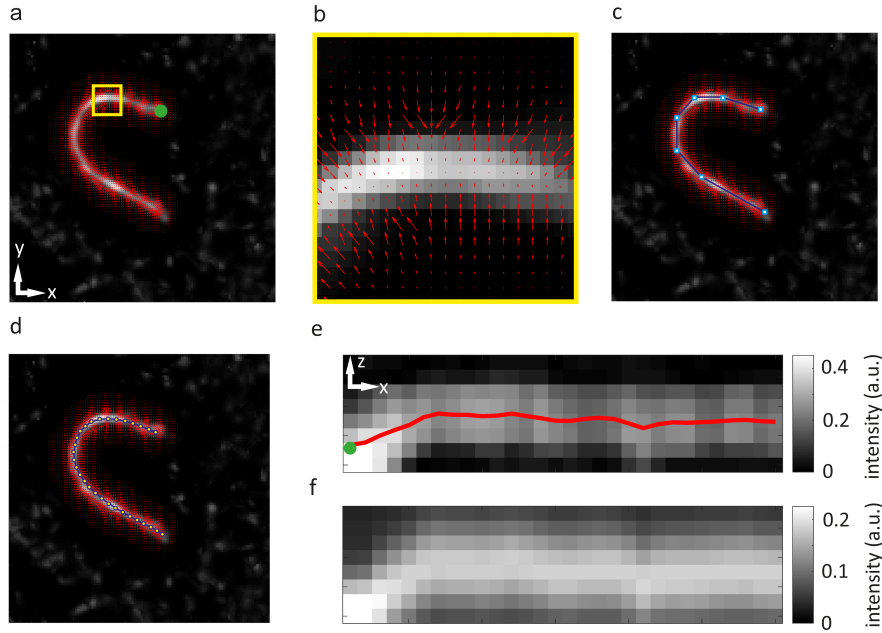


Figure 3.18: 3D tracking of axonemal motion. (a) Maximum intensity projection of axoneme image (green dot indicates basal end). (b) Calculated vector for small yellow region of panel (a), converging toward pixels with maximum intensity. (c) A polygonal line with seven nodes along the contour snake. (d) Division of snake into 30 segments. (e) the vertical cross section of axonemal image and contour (green dot indicates basal end). (f) Same as (e), but after fitting axial intensity distribution at each lateral position with 1D Gaussian function.

In a next step, a height profile $h_i(z)$ is created for each segment i , averaging the intensity over pixels of the segment (Fig. 3.18e). This profile is fitted with a 1D Gaussian (Fig. 3.18f). The z -position of the maximum of this fit yield the axial coordinate z_i of the segment, and together its lateral positions x_i and y_i constitute the 3D coordinates of segment i .

An installation file 'AxonemeTracking3D.mlappinstall' for a platform-independent MATLAB app together with its source code ('source code.zip') and sample data ('testdata.mat') can be downloaded at: <https://www.dropbox.com/s/x8iequg72zmkx4b/FlagellumAnalysis.zip?dl=0>. This app executes the contour determination and contour discretization of 3D axoneme images. The zip-file contains also the commented MATLAB program 'FlagellumAnalysisExample.m' together with tracking data ('result_tracking22.mat') of the flagellum analyzed for Fig. 3.22a, b which demonstrates the calculation of curvature and torsion from a discretized contour, and their graphical display.

3.2.2.8 *Determination of basal end from distal end*

As mentioned before, the slightly ($\sim 10\%$) thicker end of axoneme accounts for the basal end. The joint head of cilia to the cell body, so-called basal body, dominantly controls the bending direction of axoneme. In intact isolated axonemes, a bending wave propagates gradually from the basal body to the distal tip [60]. We use the pre-knowledge of directionality in wave propagation along the axoneme contour length to distinguish between basal and distal ends in raw tracking coordinates. We take average curvature value of the first half (segment numbers 1:15) and the last half (segment numbers 15:30) of contour length and subsequently check for the sign of cross correlation between them. The positive sign is defined as normal direction of propagation.

3.2.2.9 *Contour padding*

Fitting of the three-dimensional contour obtained from the 3D tracking was done by a polynomial fit of the determined discrete 3D coordinates. Such a fit becomes ambiguous at the ends of the tracked contour which can lead to unphysically large values of curvature at these ends. To prevent this, we have padded a discretized contour on both ends by mirrored inner points. The impact of the number of padded points on the fit results is shown in Fig. 3.19. As can be seen, the absolute values of curvature at the contour ends become smaller with increasing contour padding, but the values in the middle of the contours remain mostly unchanged, similar to the torsion values.

3.2.3 *Results*

3.2.3.1 *Contour fitting*

Using multi-plane phase-contrast system, we recorded movies of beating axonemes with 272 f.p.s. An example of four of such consecutively taken volumetric images are shown in Fig. 3.20a, where the color encodes the third dimension.

In each of the volumetric images, the three-dimensional contour of an axoneme was discretized (see section 3.2.2.7 for 3D tracking of axoneme), and the resulting discrete lateral x_j and y_j and axial z_j positions were fitted with polynomial functions (for details see section 3.2.2.9). The result is a four-dimensional representation $\mathbf{r}(s, t)$ of an axoneme's contour as a function of time t and arc length s , where we have $|\partial \mathbf{r}(s, t) / \partial s| \equiv |\mathbf{r}'(s, t)| = 1$ which ensures that the axonemal filaments are incompressible. Discretized contours and fit results for the four images in Fig. 3.20a are presented in Fig. 3.20b. As seen from the projections into different coordinate planes, the discretized axial positions show a ~ 10 -fold bigger jitter than the lateral positions.

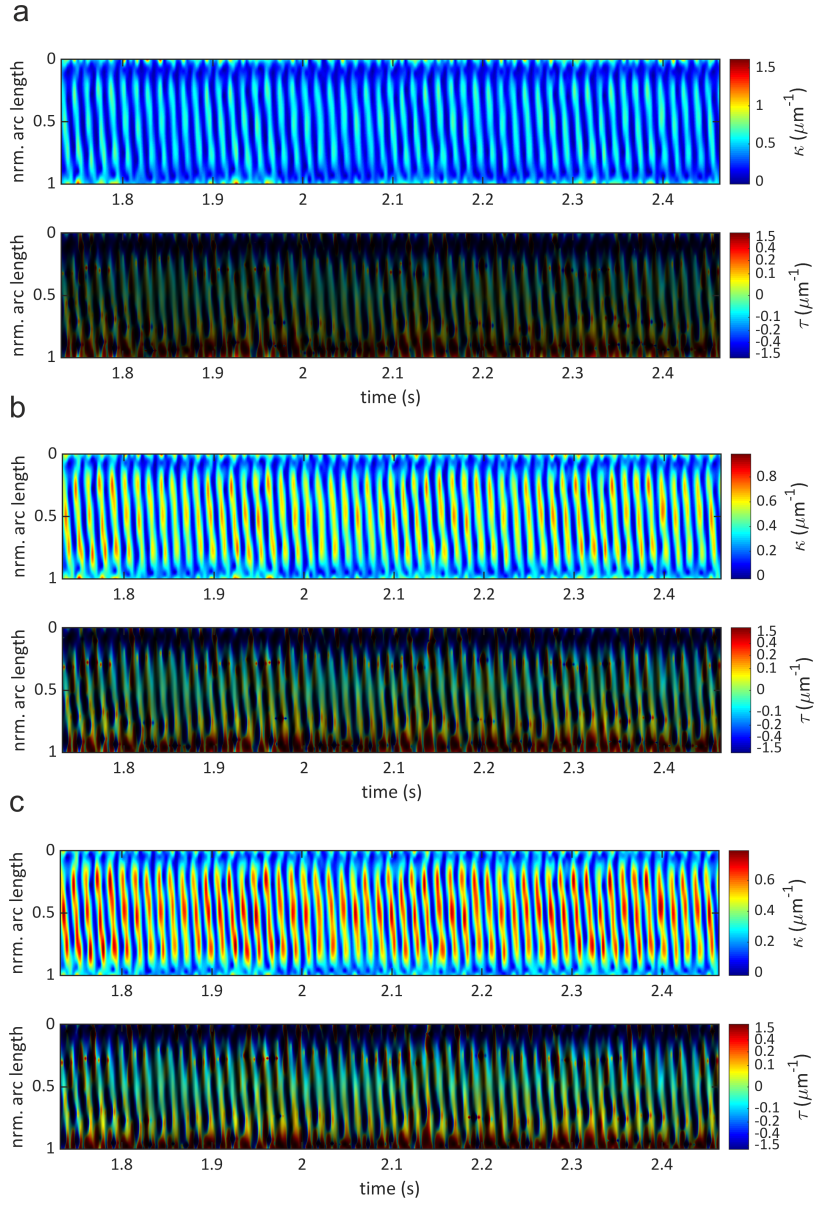


Figure 3.19: Effect of contour padding on calculated curvature and torsion. (a) Zero padding, (b) padding with one extra point, (c) padding with two extra points. Compare with Fig. 3.22 in main text showing results for padding with three extra points. As can be seen, padding does mostly suppress excessive curvature values at contour ends, but does nearly not change curvature values elsewhere, and has little impact on torsion values (different brightness values in torsion plots are due to different dynamic range of curvature values).

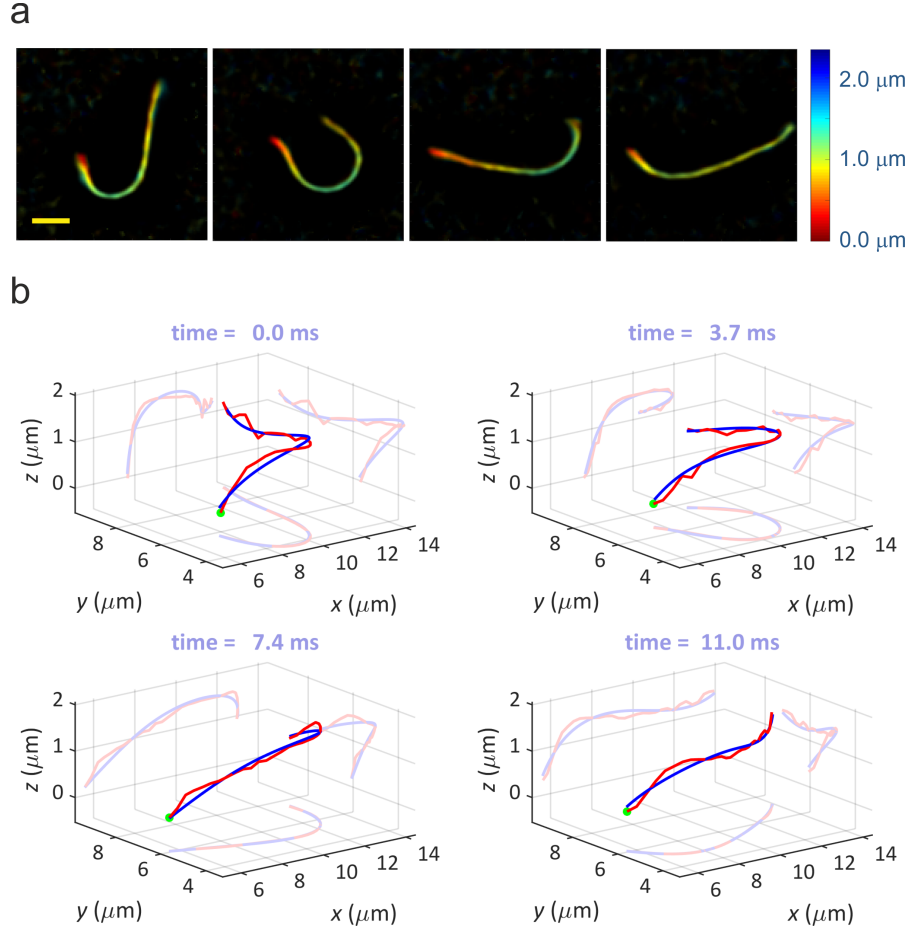


Figure 3.20: Three-dimensional recording of axoneme motion. (a) Four consecutive raw images recorded with the multi-plane phase-contrast microscope. Color encodes the axial position (see color bar), the yellow bar in the leftmost panel has a length of 2 μm. (b) Discretized axoneme contours (red) and fitted polynomial curves (blue) for the four images shown in (a). For better visibility, the respective projections into the three coordinate planes are also shown. The green dot indicates the basal end of the axoneme.

3.2.3.2 Contour fitting accuracy

We estimated the accuracy of the polynomial contour fit from the standard deviations between fitted and discretized position values, and find a lateral position accuracy better than 20 nm, and an axial position accuracy better than 120 nm shown in Fig. 3.21a ,b correspondingly for axoneme 1 and axoneme 2.

From the polynomial representation of the axonemal contours, spatio-temporal profiles of curvature $\kappa(s, t)$ and torsion $\tau(s, t)$ are calculated by [116]

$$\kappa(s, t) = |\mathbf{r}''(s, t)| \quad (3.12)$$

$$\tau(s, t) = \frac{[\mathbf{r}'(s, t) \times \mathbf{r}''(s, t)] \cdot \mathbf{r}'''(s, t)}{\kappa^2(s, t)} \quad (3.13)$$

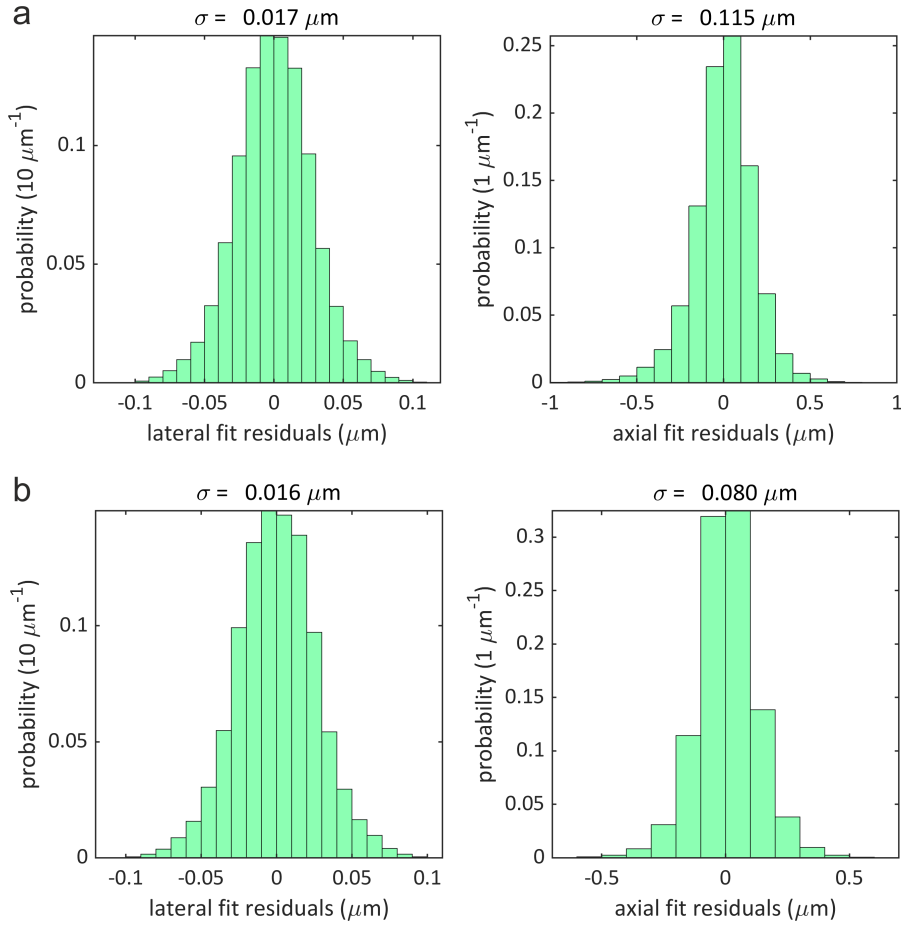


Figure 3.21: Distributions of standard deviations between discretized and fitted position values for (a) axoneme 1 and (b) for axoneme 2 in main text. Left panels show standard deviation distributions for lateral x, y -positions, right panels for axial z -positions. Calculated standard deviation values $\sigma_{x,z}$ for all distributions are given on top of each panel.

where a prime denotes differentiation with respect to arc length s . It should be emphasized that torsion quantifies the out-of-plane bending of an axoneme and can only be extracted from its full three-dimensional contour.

We measured the contour dynamics of 35 axonemes. All observed axonemes move close and parallel to the coverslide surface of the observation chamber, due to hydrodynamic interactions with the surface [117]. All except one (with a beat frequency of ~ 12 Hz) of them showed a counter-clockwise (ccw) circular motion when viewed from above. The cw rotation has been occasionally observed in previous studies which is attributed either to lack in outer dynein arms [60] or even a significant drop in ATP concentration [118]. For further analysis, we present two ccw moving axonemes with nearly identical swimming radius and high beat frequency (~ 73 Hz, determined from Fourier spectra of space-time curvature plots).

Projections (x, y -coordinates) of the swimming contours of the basal and distal ends for both axonemes are shown in Figs. 3.22a and 3.22c.

The basal end traces a smaller circle and swims closer to the surface than the distal end (see also Fig. 3.20 and Fig. 3.24) and clearly follows a helical path (see Fig. 3.20b). Space-time plots of curvature and torsion for axonemes 1 and axoneme 2 are presented respectively in Figs. 3.22b and 3.22d.

The plots show curvature waves that start at the basal end ($s = 0$) and move towards the distal tip. This is accompanied by torsion waves that start with negative torsion values at the basal end and gradually change sign until they finish with positive torsion values at the distal tip. Torsion wave dynamics are nearly identical for both the presented axonemes.

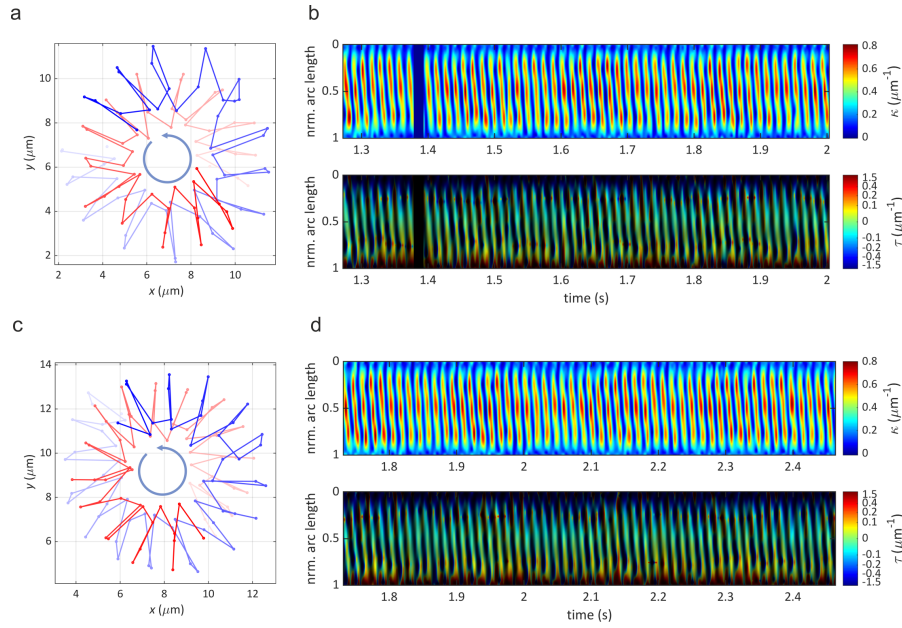


Figure 3.22: Analysis of axonemal motion. (a,c) Circular motion of basal end (red) and distal (blue) tip of two ccw-moving axonemes (correspondingly axoneme 1 and axoneme 2) as seen from above the surface. From light to dark shading indicates progression in time. Time between two discrete points of trajectory is 3.7 ms. (b,d) Space-time plots of curvature and torsion for the same axonemes as shown in (a,c), over an observation time of ~ 0.7 s. The dark vertical lane at ~ 1.4 s corresponds to a short excursion of the distal tip of the flagellum beyond the axial range of our observation volume and was excluded from analysis. Vertical axis is the *normalized* arc length ($s = 0$ at basal end, $s = 1$ at distal tip). In the torsion plots, color encodes torsion values, while brightness is proportional to curvature. This suppresses nonphysical torsion values in regions of low or zero curvature, where torsion is ill-defined. Note also the strongly non-linear color mapping (see color bar) which is used to make small torsion values better visible.

3.2.3.3 3D swimming path of axonemal basal end

Three different sections along the axonemal contour are distinguished in the Fig. 3.23a. In Fig. 3.23b we plot 3D swimming path of the basal

end using 3D tracked data of the ccw rotating axoneme. Time evolution is indicated by color. As can be seen, axoneme motion is confined to a small axial range of less than 800 nm close to the coverslide.

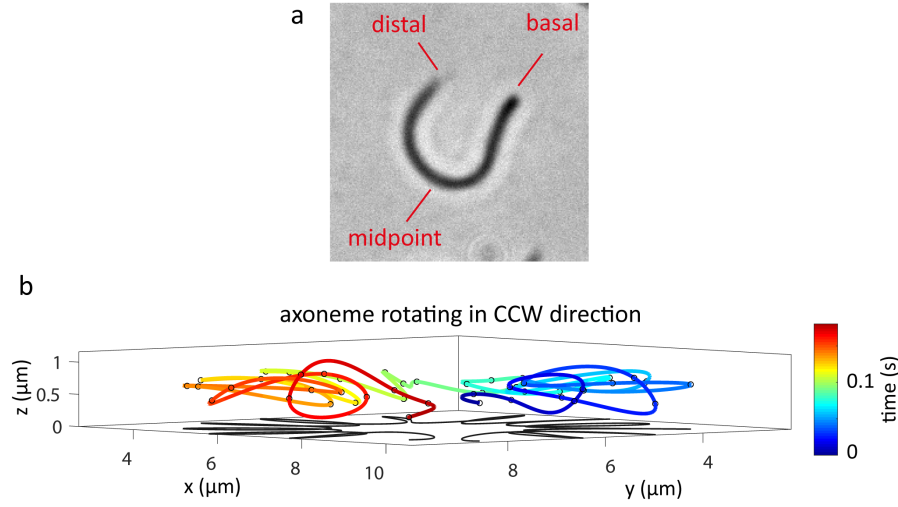


Figure 3.23: 3D swimming trajectories. (a) 2D maximum intensity projection image of one axoneme with indication of basal end (the slightly thicker end), midpoint, and distal end. (b) Swimming trajectories of basal end over nearly one complete rotation for a ccw rotating axoneme. The black shadow at the bottom is the projection of the path on the surface.

Axial localization of basal end, midpoint and distal end of axoneme: We quantify axial localisation of the three different axonemal patches highlighted in Fig. 3.23a using the 3D tracking coordinates. Fig. 3.24a, b represent distribution of the axial positions for basal end (first two segments), midpoint (intermediate segments numbers 14-16) and distal end (last two segments) patches respectively for the two axonemes presented in Fig. 3.22a, c over 860 frames. In both cases, the basal end swims on average closer to the surface than both the midpoint and the distal end. Mean plus/minus standard deviation of axial positions is given in the table 3.25. Interestingly, the midpoint of both axonemes swims on average above the distal end. Moreover, various axial coordination of the three patches indicates a helical path.

3.2.3.4 Volume axial range required to cover axonemal motion

Using z -coordinates obtained from tracked data, I estimate the axial range of motion for all $n = 35$ axonemes measured. Fig. 3.26 shows the histogram of Δz , where Δz equals to absolute value of difference between height extrema ($z_{max} - z_{min}$) of axonemes with respect to the surface in all frames recorded. Mean plus/minus standard deviation obtained from fitting curve is $(1 \pm 0.42) \mu\text{m}$ which demonstrates nearly planar motion of an isolated *Chlamydomonas* axoneme in vicinity of a surface. Moreover, it shows that the axial extent chosen,

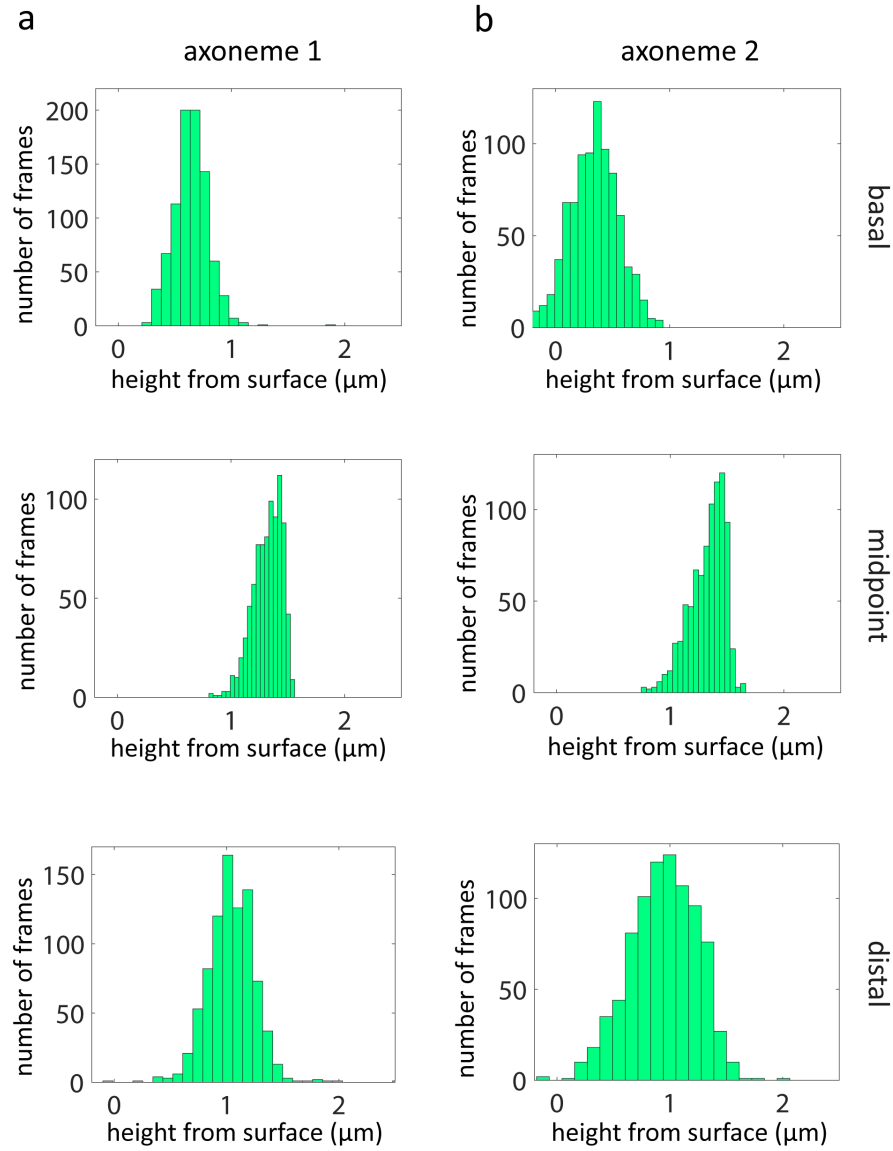


Figure 3.24: Axial position of different axonemal segments. (a) Height distributions of basal end, midpoint, and distal end of the axoneme 1 over 860 frames. (b) Same as panel (a), but for the axoneme 2.

($\sim 2.5 \mu\text{m}$), with 335 nm average inter-plane distance fits adequately to both cover and sample the axial motion of axoneme.

3.2.3.5 Distribution of beat frequency

Beating frequency of axonemes were calculated using power spectrum density (PSD) of curvature. This has been shown correspondingly in Fig. 3.27a, b for axoneme 1 and axoneme 2 as the highly active ones with 73 and 72.6 Hz.

Considering all 35 axonemes, they exhibit a quite broad distribution of beat frequency (Fig. 3.27c), i.e. from 10 to 73 Hz which can be considered as different levels of activation or ATP consumption in dif-

height from surface (nm)	basal end	midpoint	distal end
axoneme #1	641 ± 153	1320 ± 127	1041 ± 230
axoneme #2	333 ± 215	1323 ± 156	947 ± 320

Figure 3.25: Table of mean values and standard deviations of the height distribution for basal end, midpoint, and distal end for the two axonemes.

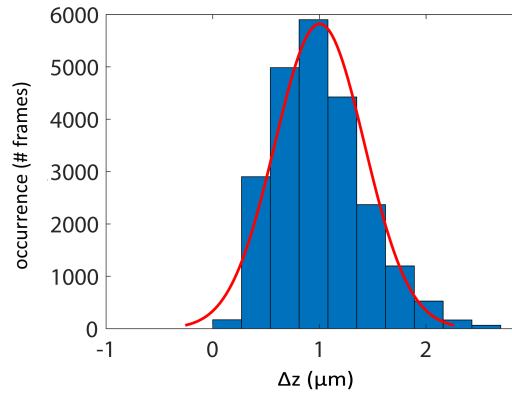


Figure 3.26: Frequency of absolute difference value between extrema of axonemal height from surface. Solid red curve indicates distribution fit.

ferent axonemes. Alternatively, higher frequencies might correspond to early measurements because axonemes were measured individually one after the other where ATP concentration drops in time due to its consumption by axonemes. With a good approximation based on literature, one can consider axonemes with beat frequencies higher than 40 Hz as the well-activated ones.

3.2.4 Conclusion and Discussion

We have developed a novel multi-plane phase-contrast microscope that allows for volumetric imaging with close to diffraction-limited resolution and with rates of several hundred volumes per second. In our application of imaging *Chlamydomonas* axonemes we have chosen such a magnification so that the eight image planes cover a volume of $\sim 2.5 \mu\text{m}$ depth. For applications that require imaging over a deeper volume, this depth value can be easily changed by changing magnification. Using our microscope, we resolved the rapid ATP-driven motion of demembranated *Chlamydomonas* axonemes in three dimensions. We were able to reconstruct the spatio-temporal dynamics of

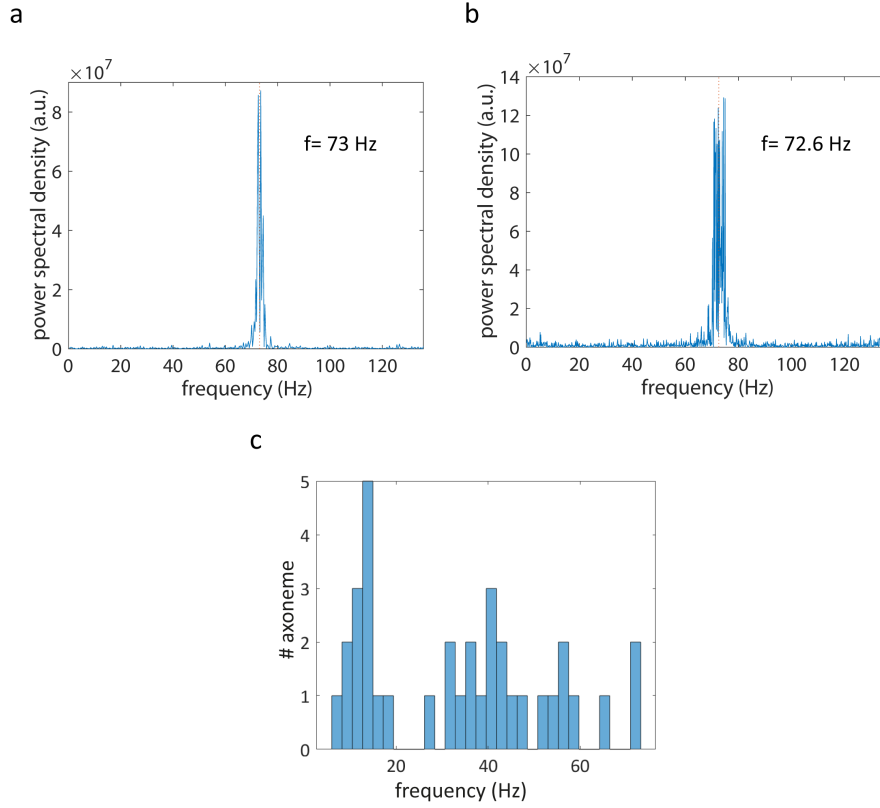


Figure 3.27: fundamental beat frequency of (a) axoneme 1 and (b) axoneme 2, (c) fundamental beat frequency distribution of 35 axonemes.

curvature and torsion of axonemes.

The observed bending and torsion dynamics demonstrates the fundamentally *three-dimensional* nature of flagellar motion. We propose that the observed torsional waves are closely connected to the intrinsic chiral structure of the axoneme and to twist induced by dyneins. According to the model developed in Refs. [91] and [93], dynein motors induce sliding between neighboring MTDs which does not only drive axoneme bending but also induces twisting of the axoneme. Dyneins transiently attach with their MT binding domains to neighboring MTDs and walk towards the basal end which cause distal-oriented sliding forces between neighboring MTDs [119]. In an untwisted axoneme, such a motion will induce a positive twist (as seen from the basal end) which should be observable as a positive torsion in a bend axoneme. Because we observe a repetitive negative torsion in each beat cycle close to the basal end, we suggest the existence of an intrinsic negative twist at the beginning of each beat cycle. This is visualized in Fig. 3.28a as a side view of sinistrally twisted MTDs close the basal plate of an axoneme to which the axonemal MTDs are fixed (note that numbering of MTDs in this figure follows Ref. [76]). Then, action of the dyneins unwinds this negative intrinsic twist, reducing negative torsion at the basal end, inducing a twist-free region in vicinity of axonemal mid-points, but generating positive twist and

torsion at the initially twist- and torsion free distal end (Fig. 3.28b). Such change in torsion sign has been observed also in quail sperm flagella [120]. Any axonemal bending readily translates twist into torsion with the same sign.

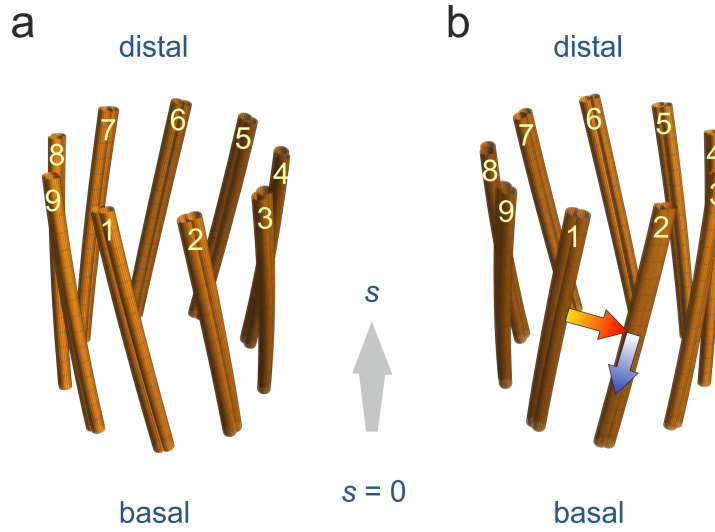


Figure 3.28: Twist of an axonemal structure. Shown are the nine MTDs around the circumference of an axoneme. (a) Intrinsic sinistral twist close to the basal end. (b) dynein-induced dextral twist close to the distal tip. The red arrow indicates the direction along which dynein motors reach from their MTD of attachment to the neighboring MTD on which they act. The blue arrows indicate the walking direction of the dynein motors. The action of the dyneins leads to sliding of MTDs with respect to each other. Due to structural connections between MTDs (e.g. by nexin proteins), this is likely to induce local twists of the axoneme structure, as shown in (b). If the whole structure is additionally bent, this twist would translate into torsion (with corresponding to twist sign), as experimentally observed at the basal end and distal tip of the bare axonemes.

In other words, we speculate that the observed torsional waves are due to dynein-generated axoneme twisting determined by axoneme structural chirality and dynein walking direction. Torsion waves start with a negative sign at the basal end and gradually change sign while propagating towards the distal tip.

We attribute the negative sign of torsion to a left-handed twist at the proximal side which slowly switches to a right-handed twist as we move towards the distal tip. Since dyneins are minus-directed molecular motors, active torque generation of accumulated dyneins at the distal tip of axonemes can generate a right-handed twist, consistent with the sign of the positive torsion observed at this location. We hypothesize that the left-handed twist at the basal end is a passive structural twist that exists independent of activity of dynein motors. Twist was observed in axonemal structure itself [120–122] down to inner pair microtubules in different types of flagella including *Chlamydomonas* [123, 124].

Further, it has been experimentally observed that axonemal outer dynein arm is capable of rotating microtubules by torque generation [125, 126]. Moreover, due to the radially asymmetric geometry of MTDs, they can exhibit torsional forces [127, 128]. Simultaneous existence of twist and bending can potentially result in emergence of torsional beat components, i.e. 3D axonemal motion.

In future studies, it would be highly interesting to see whether this connection between torsion dynamics and structural twist can be corroborated, for example by electron-microscopy of flagella. Also, which type of dyneins contribute to non-planar motion requires further investigations.

3.3 3D μ -PARTICLE TRACKING VELOCIMETRY (μ -PTV)

Here, we develop a new application for prism-based multi-plane fluorescence microscopy [15, 19]. We build and implement such a microscope for 3D tracking of single particles moving along the so-called *Marangoni* flow.

3.3.1 Introduction

Fluid velocimetry is a fundamental concept used in fluid mechanics and numerous biological processes. It can be accomplished via various non-intrusive methods, majorly using laser Doppler velocimetry (LDV) or particle image velocimetry (PIV).

LDV is a time-resolved (kHz) point measurement method where fringe patterns made by the interference of laser beams undergo a frequency shift in the presence of scattered light caused by the movement of flow-driven particles. Deformed frequency-shifted fringe patterns can be readily attributed to instantaneous velocity values of particles [129].

However, imaging-based methods such as PIV or PTV are inherently multi-point/multi-pixel, i.e., capable of determining velocity fields in both 2D and 3D, directly by a sequential recording of scattered or fluorescence signals collected from flow-tracing particles. Image frames in PIV are typically divided into several small interrogation regions to be cross-correlated with corresponding regions in other frames. Given the frame rate of image acquisition, one can obtain velocity fields by measuring pixel shifts between cross-correlated regions.

PIV in microscopic scale, μ -PIV, was firstly introduced in 1988 by Santiago et al. [130] who measured velocity fields of fluid flow in 2D based on a high NA wide-field microscope with a spatial resolution of nearly 1 μ m. After that, numerous versions of μ -PIV were introduced and exploited in microfluidic and quantitative biological studies. Among applications of μ -PIV are near-wall velocity measurement [131], investigation of surface effects on fluid velocity [132], studying combustion phenomena [133], in-vivo investigation of biological flow fields like blood flow [134, 135], etc.

A good review on different versions as well as applications of μ -PIV can be found in Ref.[136, 137].

μ -PIV has been more established than the rest of velocimetry techniques due to its high throughput and straightforward nature and its capability to deal with rather large amounts of data, including highly-dense particle images through correlation analysis.

However, μ -PIV methods have some distinguishable drawbacks. One can first mention the 2D nature of most available techniques, limiting their application only to planar fluidic motions. More importantly,

out of plane motions of particles lead in turn to particle mismatch in correlation calculations [138].

Secondly, the fluid under investigation should be stationary or predictable to obtain reliable and unbiased ensemble correlation analysis.

Under stable conditions, 3D studies are mainly restricted to a rapid scan of sample along the optical axis. Besides the signal strength, the temporal resolution of z-scan is limited to the number of 2D planes/slices selected and a scan speed of the piezo stage, which typically does not exceed the maximal speed of 100 Hz. Alternatively, one can achieve 3D velocity components in so-called stereo-PIV, which exploits at least two cameras located at different angles with respect to the sample. However, this method is generally applicable only for low NA objectives [139]. Further, it requires accurate calibration to register the position of particles in 3D.

PTV, as another optical macroscopic velocimetry method, has been broadly used in fluid mechanics. It directly measures flow velocity by tracking coordinates of individual flow-driven particles suspended in fluid [140]. PTV's ultimate goal as a moving observant or Lagrangian method is the same as PIV, an Eulerian method where an ensemble of particles in each acquired image is considered a whole in a given spatio-temporal point.

Spatial resolution and accuracy of results in both PIV and PTV techniques are mostly limited by the diffraction limit of the recording optics (NA of the objective), low SNR in particle image, interaction of the fluid with the finite-sized tracing particles, and the Brownian motion of particles. [141].

Although PTV techniques are physically more accurate than the PIV ones, they have been less exploited due to the complexity in their current technology and data processing approaches. Also, systematic errors close to boundaries (wall or surface) in PTV are minor compared to PIV.

Here, our main aim is to verify the applicability and precision of a multi-plane fluorescent microscope in micro-scale PTV. In particular, we implement such a microscope to study the fast dynamics of the individual particles following *Marangoni* flow in a sessile droplet in 3D.

3.3.1.1 *Marangoni Flow*

Fluid-driven transport of matter in the liquid phase is of paramount importance and ubiquitous in nature, technology and biological pro-

cesses of living creatures. One widespread phenomenon in fluid mechanics is the *Marangoni* effect, which is mass transport or flow occurring due to the variation in surface tension at the interface between liquid and gas [142, 143]. Surface tension itself can be altered by a change in the local concentration of solute, temperature gradient or adding a surfactant to a liquid.

The *Marangoni* effect is of primary importance in the fields of welding [144] and crystal growth [145]. Because each liquid has a particular surface tension, a mixture of two different miscible liquids, so-called binary solutions, results in the creation of *Marangoni* flow. It has been shown that *Marangoni* flow can potentially play a key role in surface cleaning [146] and in a controlled surface coating using binary solutions [143].

In 2017, Karpitschka and colleagues demonstrated that two miscible liquids (water and carbon diols) can create a quasi-static sessile droplet on a surface showing a stable *Marangoni* flow [147]. The apparent contact angle measured for such a droplet was in the range of 5° to 15° , indicating nearly a complete wetting of the surface (implying a hydrophilic surface).

It has been recently shown that the gravitational effect plays a key role in the shaping of the velocity fields inside evaporating droplets [148]. This holds for both sessile and pendant droplets (in μL volume of water and glycerol mixture).

This finding implies that firstly one requires a careful interpretation of flow fields inside an evaporating droplet. Secondly, any drift or instability in exploited $\mu\text{-PIV}$ or $\mu\text{-PTV}$ approach can result in ambiguity in experimental results due to the critical role of gravitational effects. Therefore, a stable measurement technique preferentially with a high spatio-temporal resolution is required to reliably monitor and analyze the flow dynamics in the micro-scale regime.

3.3.2 *Methods*

3.3.2.1 *Piranha cleaning and sample preparation*

Surface cleaning is an essential step in surface and $\mu\text{-PIV}/\mu\text{-PTV}$ studies because any dirt, contamination, or bump on the surface could result in unexpected results. To minimize these effects, glass coverlides were rinsed with a Piranha solution (hydrogen peroxide 30% with sulfuric acid, volume fractions 1 : 3, respectively) followed by washing in deionized water [149]. For preparing the sample (a mixture of two liquids with different volatilities together with tracing particles), Propylene glycol (propane-1,2-diol) and deionized water were mixed with volume fractions 1 : 1 with an initial volume of $\sim 10 \mu\text{L}$. Such a solution should readily yield a sessile mixed droplet when it is dis-

pensed on a glass surface. Afterwards, 0.3 μL of polystyrene fluorescent beads (540/560) of 1 μm diameter (FluoSpheresTM polystyrene microspheres, Thermo Fisher Scientific) were added to the solution as flow tracers inside the solution.

3.3.2.2 Setup

We employed an interlaced multi-plane configuration (Fig. 3.29) with $\sim 13.1 \mu\text{m}$ axial range to image flow-tracing fluorescent particles inside a sessile droplet in 3D. Unlike the sequential order of planes like those already described in the previous section, every second plane is imaged on each camera in the interlaced multi-plane configuration. In other words, the even planes are imaged by the camera 2, whereas the odd planes are imaged by the camera 1 (Fig. 3.29). This is achieved by displacement of camera 1 by a distance of $d/2n$ with respect to its focus where again d is the lateral distance between neighboring images on a camera and n is the refractive index of prism. Inter-plane distance and consequently, the axial range obtained in this configuration is half the previously described 'sequential' configuration (using the same optical components), which ensures Nyquist sampling criteria for low magnification optics.

A fiber-coupled 470 nm cyan LED light has been used for wide-field excitation through an air objective (UPLFLN20X, 0.5 NA, Olympus). The LED output is coupled to an optical fiber followed by a collecting lens ($f_L = 300 \text{ mm}$), which provides a homogeneous converging excitation light. A multi-bandpass dichroic reflects the excitation light toward the back focal plane of the microscope objective.

The emission signal is back-reflected through the objective and then separated from the excitation light when transmits through the dichroic mirror. Further isolation of the emission signal is achieved using a bandpass filter of 560/25 nm. Further, the signal is magnified by a factor of $\sim 1.33 \times$ using a relay telescope system, $L1$, and $L2$.

Multi-plane beam splitter splits the input signal into eight outputs, each with a specified optical path length as described previously but here with the average inter-plane distance of $\sim 1.87 \mu\text{m}$ in an aqueous medium. Images are recorded simultaneously using two synchronized sCMOS camera with exposure time $\sim 4 \text{ ms}$.

The microscope stage is moved laterally to bring the edge of the sessile droplet in one corner of the objective FOV in order to quantify flow velocity fields in the vicinity of the droplet boundary and contact angle of the droplet with the surface. The concentric path of *Marangoni* flow loops inside a sessile droplet is depicted in red dashed lines according to Ref. [147]. The compositional gradient of a mixed droplet leads to a gradient of surface tension, resulting in *Marangoni* flow. Under the influence of the *Marangoni* flow, one expects that in the vicinity of a sessile droplet border, the particles inside move toward, collide to, and bounce back from the border. One can

retrieve the *Marangoni* flow path, the velocity fields, and the contact angle of the droplet by imaging a number of single particles.

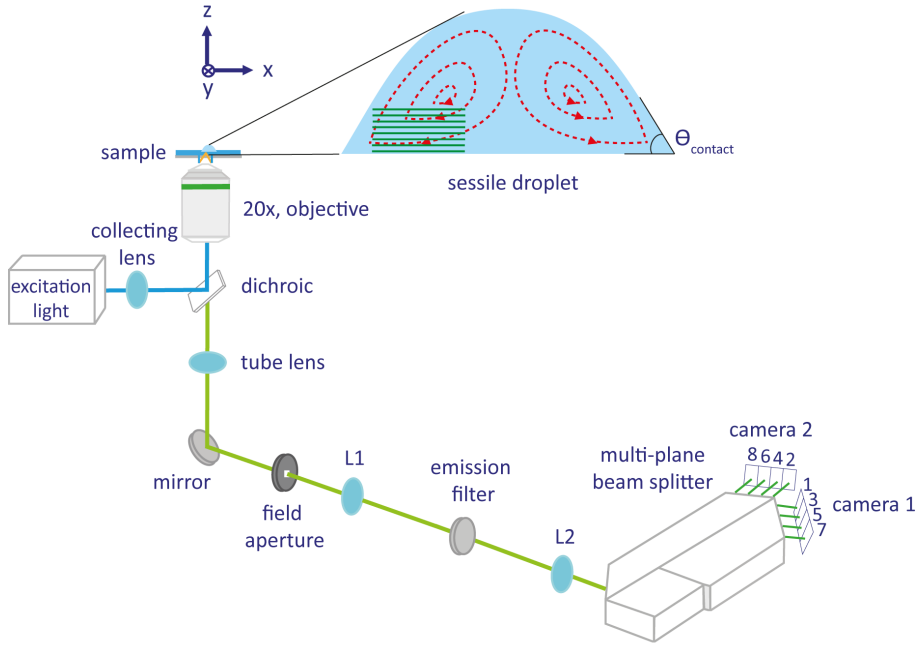


Figure 3.29: Multi-plane interlaced fluorescence setup for imaging of flow tracing single particles in 3D. Illumination light with $\lambda = 470$ nm is collected at the back focal aperture of a low magnification fluorescent objective to excite flow tracing orange fluorescent micro-spheres inside a sessile droplet with $\theta_{\text{contact}} < 90$. The emission signal is back-reflected through the objective, magnified further using L_1 and L_2 and directed toward a multi-plane beam splitter, which splits the signal into eight outputs with different but equally spaced optical paths conjugated with eight focal planes along with the depth of sample shown in parallel green lines. Output image planes of the splitter are adjusted as neighboring images without overlap using a field aperture. Once both cameras are positioned at focus, camera 1 is displaced forward with respect to the splitter output by a distance of $d/2n$ where n is the refractive index of the splitter, and d is inter-leaved lateral distance between neighboring image planes which delivers even planes on camera 1 and odd planes on camera 2.

3.3.2.3 Data analysis

Fig. 3.30a represents the raw image of a single axial plane (the bottom-most plane) acquired by the multi-plane system. Two bright, straight lines at the top corner of the image indicate an array of beads sitting next to each other at the border of the droplet. Likewise, to our routine so far in processing multi-plane data, the brightness of planes is balanced according to brightness weighting factors obtained from calibration measurement. Subsequently, a 2D Gaussian kernel (`imgaussfilt` function in MATLAB) with standard deviation of $\sigma =$

2 pixels is applied as a low-pass frequency filter. In the next step, the median intensity of all image planes is subtracted from the individual corresponding image plane, which significantly enhances the SNR by removal of background and static diffraction patterns from data. Finally, each image stack is deconvolved based on a calculated 3D PSF using ten iterations of 3D Lucy-Richardson algorithm (deconvlucy function in MATLAB), which delivers higher spatial resolution in all three dimensions. The maximum projection of intensity along the filtered 3D image stack is shown in Fig. 3.30b.

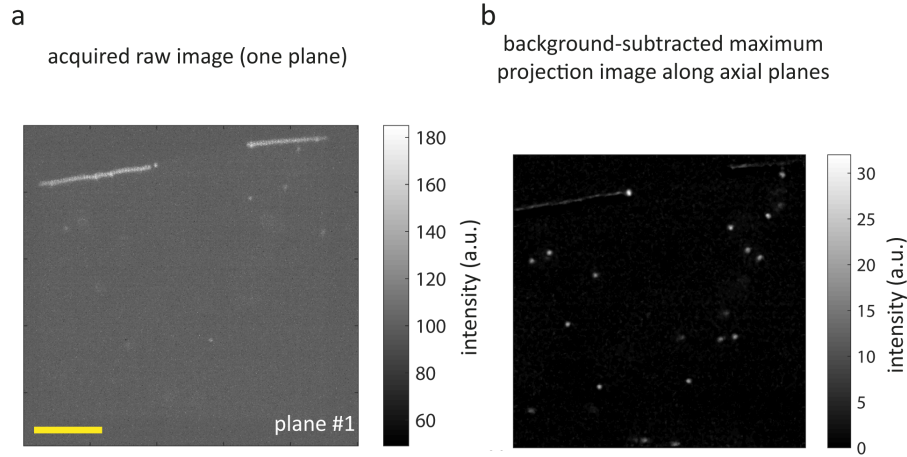


Figure 3.30: Raw image of a single plane and the processed maximum projection of the image planes acquired from flow-tracing beads. (a) example of a raw image of moving beads in the lowest plane acquired with 4 ms exposure time, (b) background median intensity subtracted image of beads obtained from the sum of maximum intensities in all axial planes. Different size of FOV in (a), (b) is due to cropping of image borders in co-registration of image planes. The yellow line in (a) indicates a length of 20 μm .

As can be seen, the intensity of bright and nearly immobile beads observable in Fig. 3.30a is notably reduced due to the subtraction of the median intensity.

I carried out the tracking of single particles in two steps:

1. 2D planar tracking of particles performed on the maximum projection of intensities along axial planes to get x, y coordinates.
2. Fitting a 1D Gaussian function on the axial extent of particle PSF to get z coordinates.

2D tracking was done using our custom-written tracking routine in MATLAB called TrackNTrace (TNT) software [150], which achieves lateral coordinates, amplitude, and background of each tracked particle. Fig. 3.31 shows the graphic user interface of TNT and setting parameters defined for particle tracking.

Tracing the path of different single particles moving toward the droplet

border is shown in different colors (Fig. 3.32a).

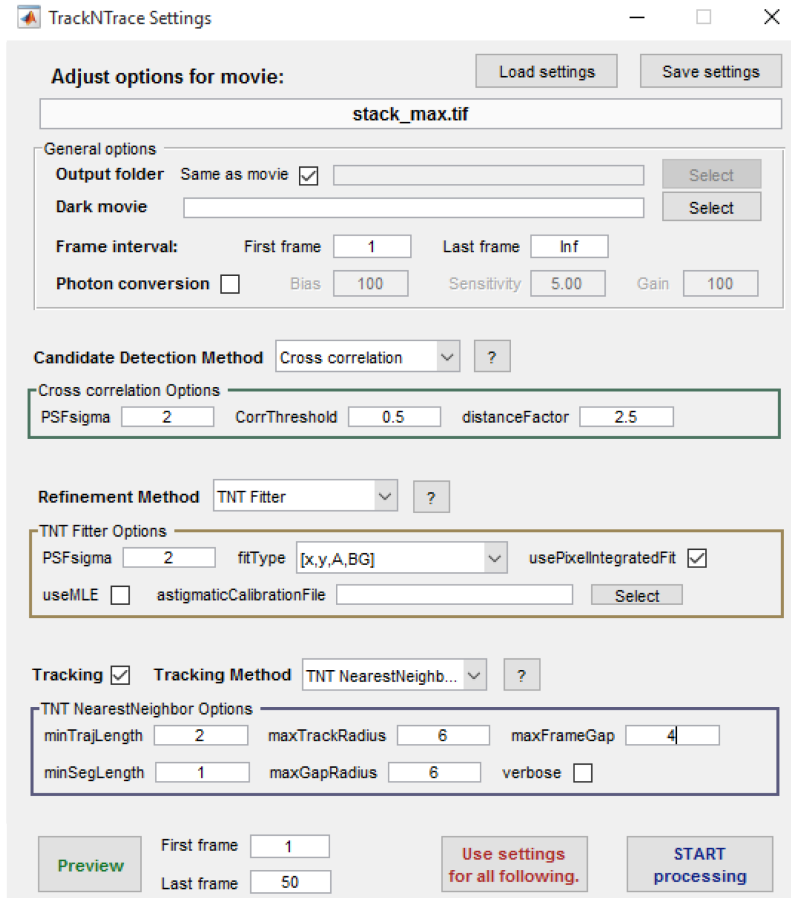


Figure 3.31: GUI of TNT software and the setting parameters used for the 2D tracking of particles performed on the maximum intensity projection along the axial planes.

In detail, only the particles moving toward the droplet border and bouncing back from it appearing in more than consecutive 90 frames are selected for further analysis. $n = 14$ of such particles are analyzed from the same measurement. The depth color-coded image of particles in one frame is shown in Fig 3.32b. Please note that for this measurement, only six axial planes lay inside the droplet volume ($\sim 9.5 \mu\text{m}$ of whole axial range). However, one can set the focus to have the bottom-most plane at the bottom of the surface to get the use of the whole available axial range. This can be ensured when the bright border of a droplet is sharp and bright at the focal plane number 1.

Fig 3.32b readily indicates that particles with different axial positions relative to the surface are distributed across the entire depth of imaging volume. Secondly, it demonstrates that particles close to the droplet border are located close to the surface. To estimate the axial location of particles, the axial range of imaging volume is upsampled

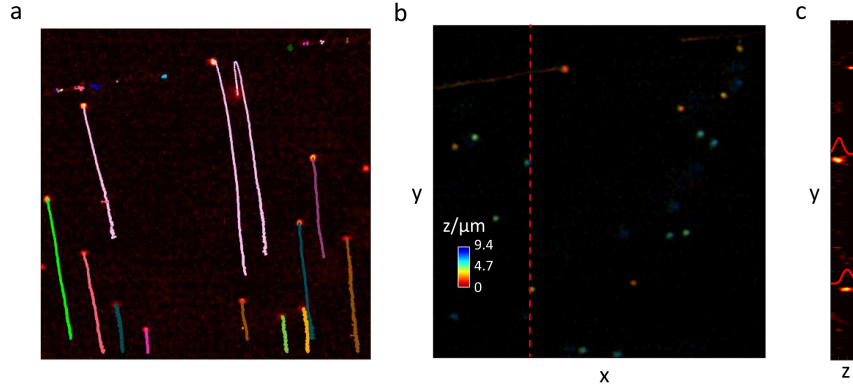


Figure 3.32: 3D tracking of single particles obtained by multi-plane fluorescence system. (a) path of different flow-tracing particles obtained from 2D tracking shown in various colors indicating a directive flow, (b) One frame of the image stack where colors represent particle's height with respect to the surface, (c) An axial yz slice of a 3D stack from the red dashed line highlighted in (b) including two particles. 1D Gaussian curves in red depict intensity fit to the axial extent of PSF.

from 6 to 26 planes by linear interpolation to facilitate the fitting of a smoothed one-dimensional Gaussian curve to the axial extent of PSF. Fig 3.32c visualizes a zy slice (axial view) of imaging volume along the red dashed line highlighted in Fig 3.32b, which contains two particles with their respective Gaussian fit intensity plots. The maxima position of the Gaussian fit is estimated as the axial location of the particle.

3.3.3 Results

We used the obtained 4D coordinates of particles, i.e., (x, y, z, t) , in calculating particle velocity, the contact angle of the droplet, and estimate streamlines of flow using velocity fields.

We observe that particles dominantly move toward the droplet border, hit the border, and bounce back from it. The inclination angle of particles with respect to the lateral plane, defined as $\tan^{-1}(\frac{z}{\sqrt{x^2+y^2}})$ where the origin is set at the border of the droplet, i.e., where the particles collide (Fig. 3.33a). The time evolution of such angle is shown in Fig. 3.33b, where the spike in the inclination angle around $t = 1$ s indicates the collision of the particle to the droplet border.

As already mentioned, this type of particle motion can be attributed to the existence of the *Marangoni* flow. Few particles stick to the border after the collision. This happens most likely because of the relatively big particles (1 μm in diameter), which makes them good candidates to pinning.

To quantify our observation, we obtain instant planar velocity (V_{xy}),

axial velocity (V_z), and total velocity (V_{tot}) of individual particles at each frame position, indexed by j , based on the equations below.

$$V_{xy}(j) = \frac{\sum_{n=-k/2+1}^{k/2} (r_{j+k/2} - r_{j-k/2})}{kt} \quad (3.14)$$

$$V_z(j) = \frac{\sum_{n=-k/2+1}^{k/2} (z_{j+k/2} - z_{j-k/2})}{kt} \quad (3.15)$$

$$V_{tot} = \sqrt{V_{xy}^2 + V_z^2} \quad (3.16)$$

where $r = \sqrt{x^2 + y^2}$ and t denote respectively radial coordinate and time duration of a single frame. k is the length of window, set to $k = 6$, across adjacent elements of the position j .

In other words, coordinates in every six sequential frames are averaged to reduce noise-related jitters or fluctuations in velocity vectors. V_{xy} and V_z of a single particle versus its radial and axial distance from droplet border, i.e., $r = z = 0$, are respectively plotted in Fig. 3.33b, c. In both figures, color encodes the progress of time.

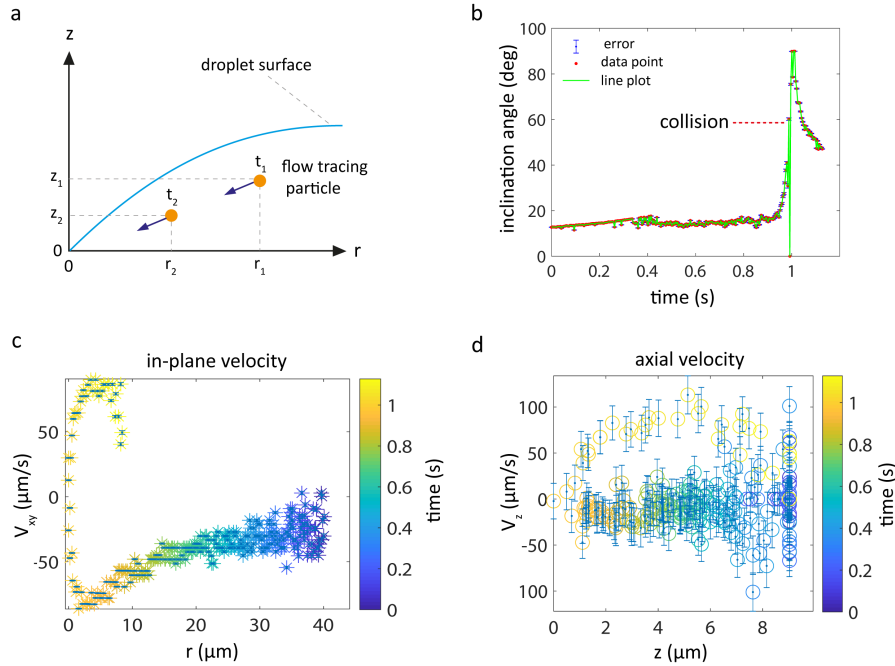


Figure 3.33: Velocity field a single flow tracing particle moving in a *Marangoni* flow before and after a collision to a droplet border. (a) Schematic of the particle motion in two different spatio-temporal coordinates of (r_1, z_1, t_1) and (r_2, z_2, t_2) where $t_2 > t_1$ and the coordinate's origin is located at the border of droplet, (b) spike in inclination angle due to collision, (c) radial velocity and (d) axial velocity component. The negative velocity values correspond to forward motion (before the collision) of the particles, whereas the positive values belong to backward motion (after collision), all with respect to the droplet border ($r = z = 0$). Colors in (c, d) encode the time progress.

Velocity values with negative signs indicate the forward motion of particle toward the droplet border, whereas positive signs belong to the backward motion when the particle moves away from the border. Besides the collision effect, the accelerating particle motion can be evidently observed in both lateral and axial dimensions. Further, absolute lateral velocity is, on average, more than doubled the velocity in the axial direction.

Particles reach their highest absolute velocity ($\sim 85 \mu\text{m/s}$ for the particle shown in Fig. 3.33) at the droplet border or just in the vicinity of it (roughly in $1 \mu\text{m}$ interval of lateral distance from the border) which is in order of particle size. Deviation of this distance from zero can be attributed either to the wall effects or not sufficient temporal sampling of the rapid motion in a close neighborhood of collision border, which causes a ghost image resulting in a reduction in the tracking precision.

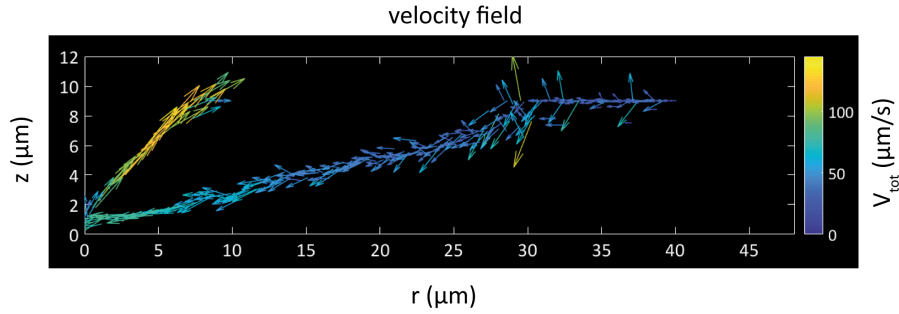


Figure 3.34: Velocity vectors of a single particle tracing the *Marangoni* flow in the vicinity of a sessile droplet border located at ($r = z = 0$). Both the color and the length of arrows indicate the magnitude of the velocity vectors.

Fig. 3.34 represents corresponding vectors of total velocity where the trend of arrows can be approximately considered as flow field or so-called streamline. Both length and color represent the magnitude of velocity arrows. A significant increase in velocity is observable in the vicinity of the droplet border. The angle between the particle's backward path (the path after collision) and the horizontal axis is defined as the contact angle of the droplet.

We obtain velocity fields of single particles as an approximation for streamlines inside the droplet (see Fig. 3.35a). A straight line is fitted to the particle path before and after collision (Fig. 3.35b) to estimate the contact angle. The mean plus/minus standard deviation of this angle for fourteen molecules' presented data is $62.1^\circ \pm 12.1^\circ$. I consider the maximum angle measured, $\theta_{\text{contact}} = 76.2^\circ$ as an estimate for droplet contact angle, which indicates an intermediate state of wetting.

As previously mentioned, it has been shown that for a droplet wetting a surface, the contact angle of a sessile droplet is in the range

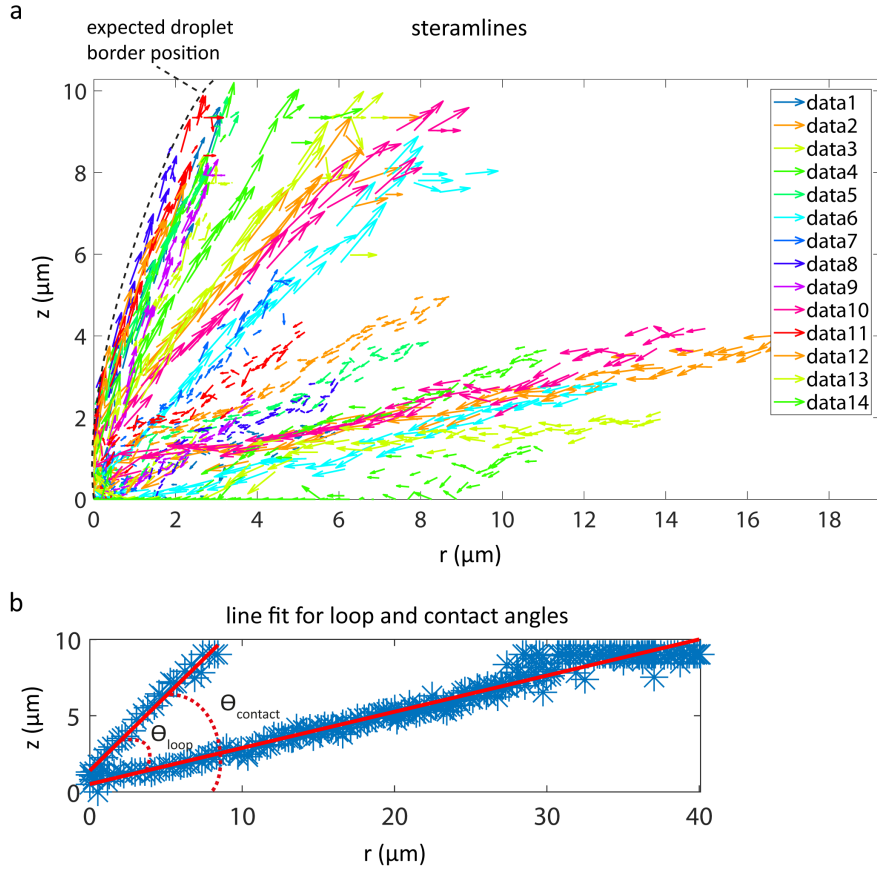


Figure 3.35: Streamlines and contact angle. (a) velocity vectors of fourteen particles within 90 frames in the neighborhood of a droplet border representing flow fields (b) line fit in red to forward and backward path of a single particle (the data 10 in (a)). θ_{contact} measures the angle between the backward path and horizontal plane, and θ_{loop} is defined as the angle between the lines fitted.

of $5^\circ - 15^\circ$ in steady-state [147]. Deviation from this value could be mainly attributed to non-smooth coverslip surface and saturation in humidity, which has been shown to be directly proportional to the contact angle in a power-law fashion [147].

Moreover, localization precision in lateral dimension, $\delta_{x,y}$, is approximated by Eq. 3.17 where σ , N and τ respectively denote lateral extent of PSF in pixel (the initial set parameter 'PSFsigma' in Fig. 3.31), collected number of photons and background to signal ratio (see Ref.[151]). The background to signal ratio, is calculated by $\tau = 2\pi b(\sigma^2 + 1/12)/N$ where b denotes the background intensity. Conversion factor of detector, i.e., the ratio of the gray digital counts to photo-electrons, and the quantum efficiency of ORCA-Flash 4.0 V2 sCMOS camera at $\lambda = 550$ nm have been correspondingly assumed equal to 0.46 and 0.72 to estimate the collected number of photons which is obtained by $N = 2\pi\sigma^2 I(0.46/0.72)$ where I is the peak sig-

nal intensity. The background intensity (b) and peak signal intensity (I) are obtained by the TrackNtrace tracking software.

$$\delta_{x,y}^2 = \frac{\sigma^2 + \frac{1}{12}}{N} (1 + 4\tau + \sqrt{(\frac{2\tau}{1 + 4\tau}))} \quad (3.17)$$

The standard deviation of axial positions obtained from the Gaussian fit is considered as the localization precision of our system along the optical axis. Averaged over $n = 14$ particles measured, the localization precision of our method is better than $\delta_{x,y} = 60$ nm in lateral and $\delta_z = 300$ nm in axial direction in a $120 \mu\text{m} \times 120 \mu\text{m} \times 13 \mu\text{m}$ field of view. I have provided a straightforward custom-written script in MATLAB, which takes 2D tracked coordinates, fits the axial location obtained by a multi-plane microscope, and calculates velocity fields, contact angle, and localization precision.

3.3.4 Discussion

In this work, we introduced one of the most appropriate applications of fluorescent multi-plane microscopy in instant 3D μ -PTV.

Our current application can be considered as a novel 3D and instant μ -PTV method. However, multi-plane data can also be treated as 3D μ -PIV in case one applies correlation analysis to retrieve velocity fields. In the case of 3D μ -PIV, however, a high concentration of tracing particles in the FOV is required for reliable analysis, in particular, to enhance the localization precision and reduce incorrect spurious vectors.

The temporal resolution of our imaging system is only limited by the camera frame rate because tracing bead particles are typically bright enough, which results in high SNR images. To study very fast flow dynamics, the imaging speed can be straightforwardly enhanced coming at the price of selecting smaller regions of interest on FOV. For instance, using the current setup, one can acquire 540 volumes with size of $(120 \mu\text{m} \times 60 \mu\text{m} \times 13 \mu\text{m})$ per second which obtains ~ 63 frames from particles with in-plane speeds of 1 mm/s.

One can incorporate a camera synchronized with the sCMOS cameras to have a side view from droplet to control droplet shape and evaporation process during multi-plane recording. Moreover, such a camera could be used to easily cross-check validation of measured contact angles and streamlines obtained by instant multi-plane system.

Meanwhile, the selection of tracer particles is important to achieve reliable results because both the signal strength in μ -PIV (or μ -PTV) data and hydrodynamic interactions between the tracing particles and flow is highly dependent on the shape and dimension of particles. On the one hand, the particle size has to be small enough to be faithfully considered a flow tracer with minimal hydrodynamic in-

teractions. On the other hand, it should be large to represent less diffusive Brownian motion, and more importantly, to deliver sufficient fluorescence or scattering signal. In fluorescence techniques, this size is usually selected in the range of 100 nm-1 μ m.

One can upgrade the presented work by exploiting a field-programmable gate array (FPGA) card to speed up the data streaming and analysis and reduce the memory allocation for long term measurements [152].

The droplet volume in this type of flow measurement is typically in the range of 1 – 10 μ L. Therefore, one should carry out the experiments rather quickly (roughly in the range of 5 – 10 minutes) before droplet evaporation. Moreover, it has been proved that the flow velocity in an evaporating sessile droplet is nearly one order of magnitude higher during its last lifetime steps [153].

3.4 3-COLOR MULTI-PLANE MICROSCOPY

3.4.1 Introduction

Investigation of several sub-cellular components via multi-color detection is one of the critical applications of fluorescence microscopy. In biomedical imaging, specificity in fluorescence-based techniques has been a robust tool in discovering the structure, colocalization, and dynamics of different species in a sample of interest. A typical example of a multi-color fluorescence microscopy image is shown in Fig. 3.36. Here, we observe a 3-color fixed cell from the *vero* cell line where each color represents a particular subcellular component. Nuclei, α -tubulin, and actin are stained by fluorescent markers, i.e., 4, 6-diamidino-2-phenylindole (DAPI), fluorescein isothiocyanate (FITC) and Atto 550-phalloidin accordingly.

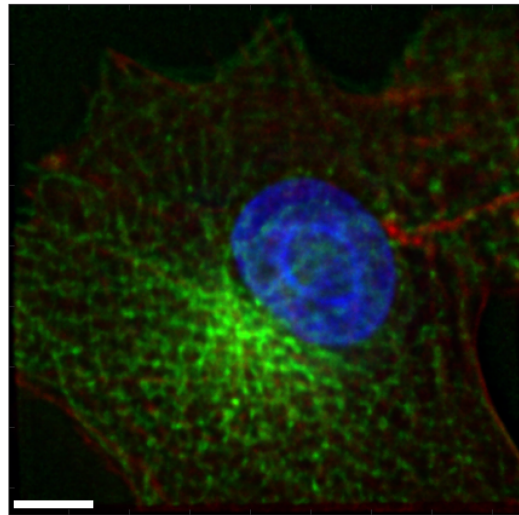


Figure 3.36: Three color fluorescence image of a stained fixed Vero cell. Nuclei (blue), α -tubulin (green) and actin (red) are correspondingly labeled by DAPI, FITC, and Atto 550-phalloidin. Scale bar indicates a length of 5 μm .

Selectivity in fluorescence imaging is achieved by using unique characteristics of fluorophores such as fluorescence life-time, spectral property, i.e., specific excitation and emission wavelength or recently by PSF engineering via deep learning [154]. In life-time based techniques like fluorescence life-time imaging microscopy (FLIM) [155], a time-correlated single-photon counting (TCSPC) electronic device synchronized with a pulsed laser (used for fluorescence excitation) record the arrival times of photons detected by photo-multiplier tube (PMT) or a single-photon avalanche photodiode (SPAD). One can readily histogram the number of photons collected versus arrival times to estimate fluorescence life-time at each scan position (each pixel) and construct a FLIM image of a sample where instead of typ-

ical image intensity, each pixel represents a particular life-time value [156, 157].

Spectrum-based methods are often accomplished by hyperspectral imaging by means of multi-channel spectrometers and then post-processing data via spectral pattern matching or linear spectral unmixing to disentangle different colors [158–160].

It has been shown that one can obtain simultaneous multi-color information from spectrally close fluorophores excited by a single laser [161]. It is worth noting that the acquisition of reference data sets for each spectral channel is crucial for reliable analysis of acquired data. One can resolve multiple targets by the combination of the two techniques in so-called spectral FLIM, which exploits both spectra and lifetime information of fluorophores [162, 163].

Although the mentioned techniques render high throughput and a spectrally resolved picture of a specimen, they are massive on both the hardware (complexity of experimental setup) and on the software side, where demanding analysis routines are required to determine color components and for minimization of cross-talks between spectral channels. More importantly, instant multi-color information in all of these methods is restricted to only one 2D planar slice of the sample. In 2013, Abrahamsson and coworkers introduced a chromatically corrected grating-based imaging system implemented on an epi-fluorescence microscope which obtains dual-color instant 3D images [14]. However, the proposed system firstly requires several sophisticated optical elements for aberration correction. Secondly, the demanding optical alignment of this system impedes its widespread application. Further, it is limited only to two spectral channels. Here we present a novel instant three-color multi-plane imaging system by the combination of an optics-based spectral unmixing and the multi-plane prism.

3.4.2 *Methods*

3.4.3 *Design of the spectral unmixing block*

The idea behind this element is to split the emission into three separate color channels. To separate them on the camera, we introduce an inclination angle $\pm\theta$ with respect to the xy-plane for the first and third color channels, respectively. By this, the position of the respective image on the camera will be shifted by $\Delta z = \pm f_{L2} \sin(\theta)$. Fig. 3.37 depicts the design of our spectral unmixing block in detail. The initial beam transmitted through the lens $L1$ has a height of ~ 84 mm from the breadboard. All three emission wavelengths should travel the optical path length, which equals to sum the focal length of the lenses $L1$ and $L2$. One should position the optical elements close to the lens $L1$ to have enough space for alignment in the next steps. The long-pass

dichroic mirror (580) is placed in 90 mm distance from the lens $L1$, measured from the middle of the lens holder to the entrance point of the light on the long-pass dichroic mirror, which is a distance enough for the alignment of the long-pass dichroic mirror yet no disturb with the band-pass emission filter positioned between the long-pass filter and the mirror 3 which is in 50 mm orthogonal distance from the long-pass (580) dichroic mirror. The same distance is adjusted accordingly between the long-pass dichroic mirror (624) and the mirror 4 also between the mirror 2 and the mirror 3. The 50 mm distance should be sufficient to place the emission filters in the orthogonal paths (along the y -direction). The distance between the sequential elements along the x -direction (for instance between the long-pass 580 and the long pass 624) is adjusted roughly to 30 mm.

The crucial step is that the green beam reflected from the mirror 3 and the orange beam reflected from the mirror 4 do not face any optical element in their path until the lens 2. Simultaneously, all the wavelengths meet roughly on the same region on the lens $L2$ firstly to reduce image artifacts arisen from different aberrations like the spherical aberration, and secondly, to lay inside the camera pixels area. The lens $L2$ with the aperture size of 2 inch is selected to reduce the spherical aberration. First, to align the beam paths, I adjust the red beam path where the mirror 5 is positioned as close as possible to the breadboard yet able to reflect the red beam with the height of ~ 78 mm from the breadboard. Afterward, the red beam is reflected off-axis off-axis from the top area of the mirror 5, and it meets the lens $L2$ with the height of ~ 82 mm (close to the height of the initial on-axis beam). The orange beam remains parallel on-axis in all its traveling paths from the long-pass dichroic mirror (624) until the lens $L2$ and cameras. The mirror 4 is also positioned in such a way to reflect the orange beam with its utmost area, letting the green beam passing non-disturbed over it. The green beam is tilted up by the long-pass dichroic mirror (580), arriving the mirror 3 with the height of 88 mm and then is reflected a bit down, meeting the lens $L2$ with the height of ~ 87 mm.

One can configure the spectral unmixing block for a different set of emission channels, such as blue, green, and red. This is achieved by the incorporation of proportional dichroic mirrors and band-pass filters. A photo of obtained blue, green, and red channels in two orthogonal sets of four adjacent planes is shown in Fig. 3.38.

3.4.3.1 Setup

We propose a simultaneous acquisition of eight axial image planes, each containing three spectrally-distinct color channels. Three coherent light sources, a 100 mW laser at $\lambda = 473$ nm (CNI), a 200 mW laser at $\lambda = 561$ nm (CNI) and a 140 mW laser at $\lambda = 637$ nm (Coherent,

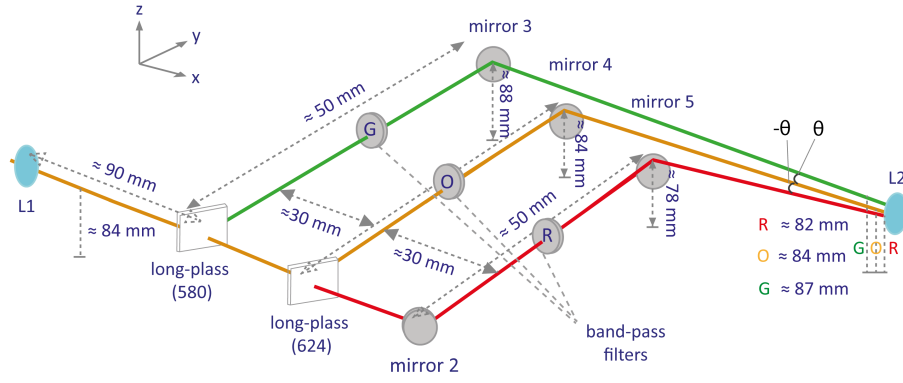


Figure 3.37: Spectral unmixing. The optical axis height is ~ 84 mm. The initial beam is split into three different bandpasses: $\lambda < 580$ nm, the green, reflected from a long-pass filter with a cutoff at 580 nm, $\lambda 580 : 624$ nm, the orange, reflected from a long-pass with a cutoff at 624 nm, and $\lambda > 624$ nm, the red, reflected from the mirror 2. The lens L1 is at a distance of 90 mm with respect to the long-pass filter 580. Except for the lenses, the sequential optical elements along each row of the x-direction are 30 mm apart from each other. The long-pass 580 filter, the long-pass 624, and the mirror 2 are in 50 mm distance accordingly from the mirrors 3, 4, and 5. The green beam's height from the mirror 3 is ~ 88 mm while this value is ~ 84 mm for the orange beam at the mirror 4 and ~ 78 mm for the red beam at the mirror 5. These beams (G, O, R) meet the lens L2 while they are respectively $\sim (87, 84, 82)$ mm height from the breadboard. The elements with symbols 'G', 'O', and 'R' are the emission filters. $+\theta$ and $-\theta$ accordingly indicate the inclination angle of the first and the third color with respect to the on-axis (the middle) color.

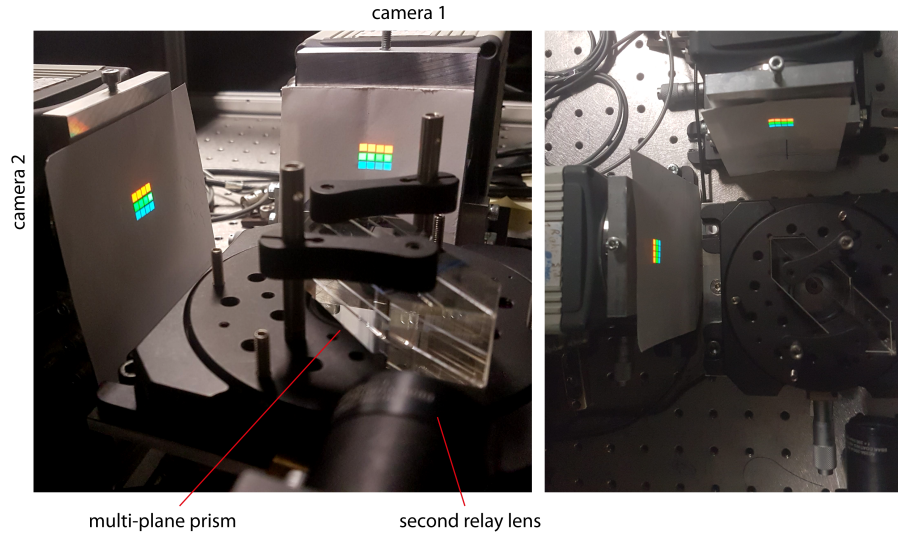


Figure 3.38: Three emission channel (the blue in the lower row, the green in the middle, and the red in the top row) $\times 8$ axial planes. Left and right panels respectively, belong to a side and a top view of the output beams of the 3-color multi-plane imaging system.

Obis) are incorporated into the illumination path of a conventional inverted epi-fluorescence microscope (Olympus IX71). A schematic of the illumination path is presented in Fig. 3.39.

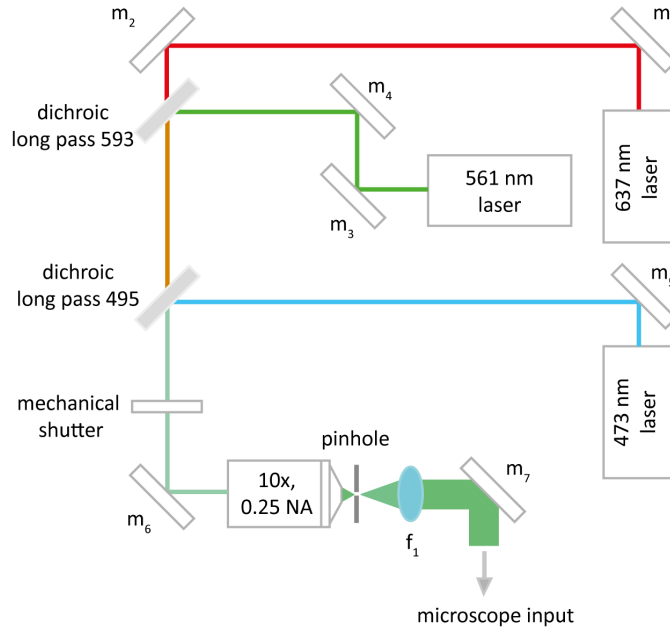


Figure 3.39: Illumination path of three color multi-plane setup. Three laser beams at 473 nm, 561 nm and 637 nm are co-aligned using a set of dielectric mirrors, m_1 to m_5 , and dichroic long-pass filters at $\lambda = 495$ nm and $\lambda = 593$ nm. A 4f system comprised of a 10x, 0.25 NA objective, and lens f_1 , is conjugated with a 20 μm pinhole to provide collimated and expanded co-path beams with a transverse mode of TEM_{00} . The mechanical shutter is slaved by a master device to control the on-off switching of illumination. The combination of co-path green and red lasers is shown in orange, and the combination of all co-path lasers is shown as light green.

Laser beams are co-aligned using dielectric mirrors (m_1 to m_5) and long-pass dichroic mirrors with wavelength thresholds at $\lambda = 593$ nm and $\lambda = 495$ nm. They are spatially filtered and expanded by a 4f system comprised of a 10x, 0.25 NA objective conjugated with a pinhole (20 μm in diameter), and a lens (f_1 with a focal length of 200 mm). The detection path of the microscope can be divided into a spectral unmixing block followed by a multi-plane beam splitter (see Fig. 3.40).

In the unmixing block, the emission signals are spectrally isolated into three distinct color channels: green (spectral range of 450 nm to 580 nm), orange (580 nm to 624 nm), and deep red (650 nm to 700 nm).

The middle color, i.e., the orange signal, propagates on-axis while the green and deep red signals are aligned off-axis (tilted with respect to the optical axis) to be imaged vertically onto separate areas on the multi-plane beam splitter and subsequently on camera 1 and

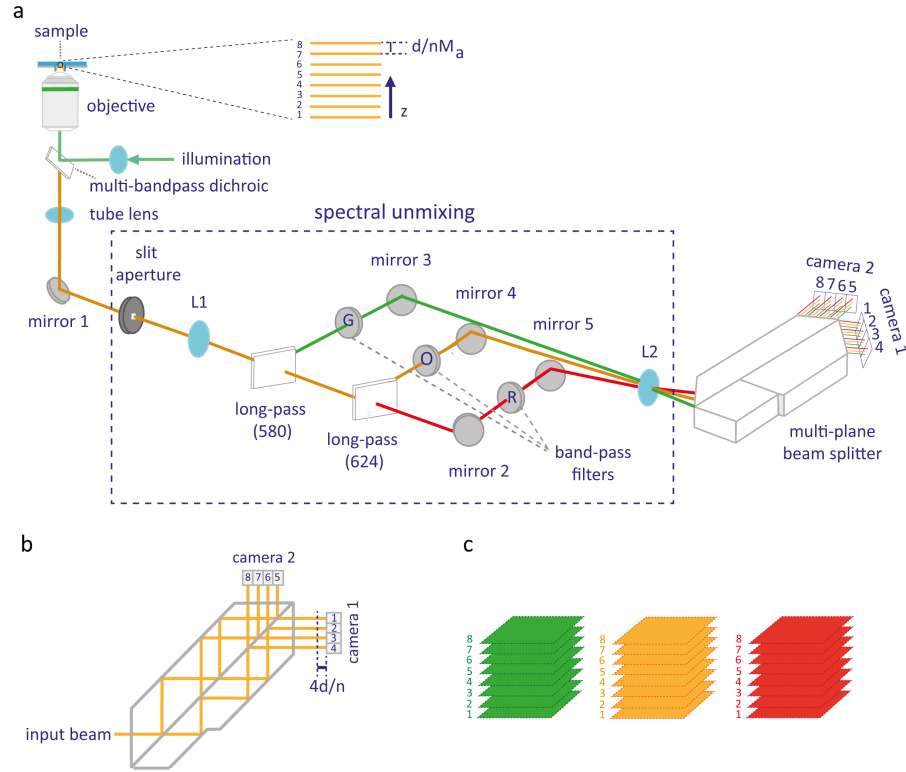


Figure 3.40: Schematic of 3-color multi-plane fluorescence microscope. (a) Excitation lights are reflected by a multi-band pass dichroic and focused at the back focal plane of an objective for epi-fluorescence illumination. A mixture of fluorescence emission signals with different colors is back-reflected through the objective and passed by the multi-band pass dichroic. The spectral unmixing block depicted inside the dashed rectangle initially splits the color-mixed signal into three distinct color bands of green ($\lambda < 580$ nm), orange ($580 < \lambda < 624$ nm), and red ($\lambda > 624$ nm). The multi-plane beam splitter renders eight adjacent images with distinguished and equally spaced optical path length corresponding to eight distinct focal planes inside the sample, shown as lines with increasing numbers for each color signal. Overall, 3-color \times 8 focal planes are simultaneously imaged by two sCMOS cameras. L_1 and L_2 are relay lenses and increase magnification by a factor of 1.33. Slit aperture prevents overlap between neighboring focal planes and controls the size of FoV. G , O and R indicate emission filters inserted respectively in green, orange, and red bands. (b) beam path of a color channel inside the multi-plane prism. (c) Schematic for simultaneously acquired 3 color \times 8 axial planes.

camera 2.

Each color signal is passed through a multi-plane beam splitter that provides eight different axially-distinguished planes along with the sample depth. The optical path of the orange signal inside the multi-plane beam-splitter is depicted schematically on the top right of the Fig. 3.40.

As seen, the multi-plane beam splitter is geometrically designed in a way that it splits an input beam through multiple reflections into two sets of four neighboring output beams with distinct but equally distanced optical paths.

Ultimately, this configuration provides simultaneous imaging of three distinct color channels, each containing eight axial planes. The field aperture avoids lateral overlap of axial planes when imaged onto the camera chip. Images are magnified further by a factor of 1.33 using a telescope system comprised of lenses $L1$ and $L2$.

In the image plane, the inter-leaved lateral distance between adjacent planes is $d = 3.2$ mm, which matches in size to the width of the $13.3 \text{ mm} \times 13.3 \text{ mm}$ pixel area of our sCMOS detector (ORCA-Flash 4.0 V2, Hamamatsu). Once both cameras are positioned at the focus, the camera 2 is displaced with respect to the prism output by a distance of $4d/n \sim 9.16$ mm where $n = 1.46$ is the refractive index of the prism material. This provides sequential axial planes imaged on each camera with OPD of $\sim d/n$ between them. See table B.4 for specification of setup components.

3.4.3.2 Setup calibration

To obtain diffraction-limited performance and calibrate our imaging system, we carried out z-scans of immobilized tetra-spectral fluorescent beads of 100 nm diameter (TetraSpeckTM Carboxylate Microspheres, 0.1 μm , Thermo Fisher Scientific) that were spin-coated on a glass coverslide, using a water immersion objective (60 \times , 1.2 NA) and the relay lens system shown in Fig. 3.40.

Fluorescence excitation was done using 473 nm and 561 nm lasers. The objective was moved over an axial scan range of 7 μm with a 100 nm step size. Fig. 3.41 displays simultaneous multi-plane 3-color image acquisition, i.e., three row of colors times eight column of axial planes of fluorescent beads at one z-scan step where the image of beads is at the focus of plane #5. The numbers above images represent the corresponding plane numbers depicted in Fig. 3.40.

Comparison of image intensities of different colors at each common axial plane indicates negligible axial color aberration of the imaging system.

1D Gaussian function is fitted to the z-scan intensity values of each plane for every color channel to obtain brightness response of each plane, inter-plane distances and quantify magnitude of axial color aberration.

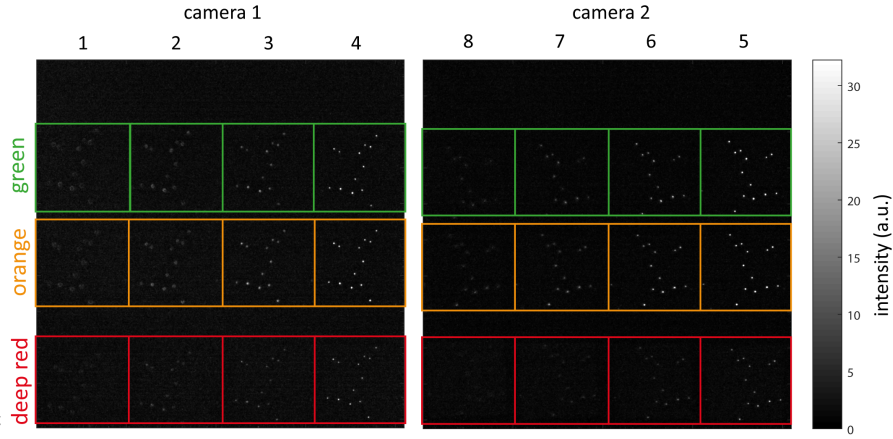


Figure 3.41: Eight-plane three-color image of tetra spectral fluorescent beads at one scan position of calibration measurement. The neighboring squares highlighted in green, orange, and red simultaneously recorded by camera 1 (right panel) and camera 2 (left panel), are axial image planes of 100 nm tetra spectral beads with corresponding emission wavelengths at 520, 593, and 685 nm. The numbers above colored squares show the axial order of the image plane from the surface. Similar intensity distribution and magnitude of tetra spectral beads in different color channels at corresponding axial planes (columns) demonstrate minimal axial color aberration of the imaging system. In this particular scan position, beads are in focus at nominal plane #5.

Fig. 3.42a indicates the measured intensity of planes in the green channel at each axial step (circles for camera 2 and cross for camera 1) and respective fitted Gaussian curves to each plane intensity. Average and standard deviation of inter-plane distances are determined correspondingly by calculation of offset between the maxima position of Gaussian fits for each color channel.

A linear fit to maximum intensity positions for each color channel is presented in Fig. 3.42b. The average inter-plane distance is slightly different among presented color channels (maximally less than 5%) due to the wavelength-dependent axial extent of PSF. Slight axial color aberration obtained from calibration data is maximally 205 nm over the axial depth range of $\sim 2.5 \mu\text{m}$ measured for the entire spectral range of 165 nm (from green to deep red emission range). This is consistent with analytical color aberration values ($\sim 220 \text{ nm}$) in (500 nm - 700 nm range) calculated from ray-tracing analysis (See SI of Ref. [19]) for multi-plane beam splitter.

It has also been shown that the multi-plane beam-splitter compensates for the color aberrations originated by the objective, the tube lens, and the telescope lenses. Ultimately, this leads to a minor axial color aberration of the imaging system. We crop the overlapping axial range in volume of different color channels based on the measured axial color aberration and the position of the bottom-most planes of each color channel, which finally renders a volume size larger than

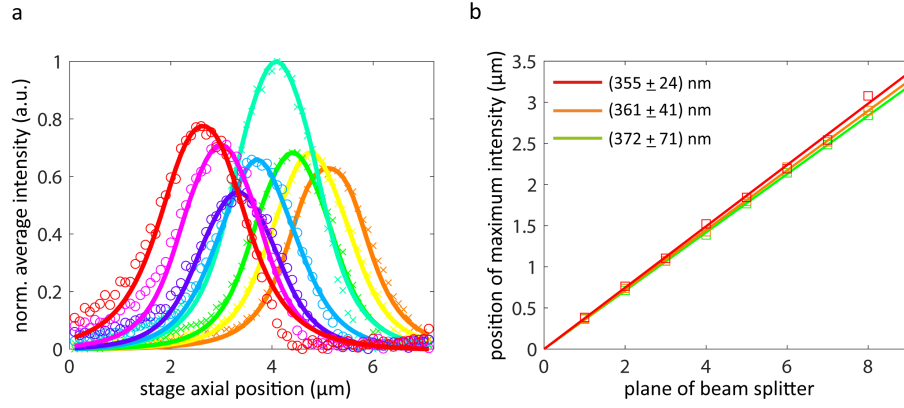


Figure 3.42: Brightness and inter-plane distance calibration of color channels. (a) the normalized average intensity of image planes in the green channel as a function of axial scan position (scan step equals to 100 nm). Solid lines represent Gaussian fits, Crosses (for camera 1), and open circles (for camera 2) indicate measured data. (b) A linear fit of positions of intensity maxima from the brightness calibration of each color channel. The fits deliver an average plus/minus standard deviation of (355 ± 24) nm for the inter-plane distance of green channel, (361 ± 41) nm for orange channel, and (372 ± 71) nm for deep red channel.

90% of the initial acquired imaging volume.

3.4.3.3 Image analysis

All image analysis was performed using a script written in MATLAB. In detail, to make a z-stack for each color channel, neighboring recorded image planes (see colored rows in Fig. 3.41) are cropped, multiplied with the brightness weighting factors obtained by calibration measurement on tetra-spectral beads and ordered planes in height. Image planes are co-registered for each individual color channel based on cross-correlation of image intensities with respect to a reference image plane (see section 3.2.2.6 in Chapter. 1). Drift between corresponding axial planes in color channels is estimated using the same image correlation analysis on tetra spectral calibration data and used to co-align and overlay the color channels.

Each color z-stack is upsampled along z to 35 planes by linear interpolation and then deconvolved in 3D based on pre-calculated aberration-free PSF above a glass surface. 3D PSF is calculated using the full wave-optical theory [103, 104] and the optical parameters of our setup (emission wavelength λ_{peak} of 513 nm for green, λ_{peak} of 580 nm for orange, and λ_{peak} of 680 nm for deep red channel, numerical aperture NA of 1.2, image magnification of $80\times$, principal focal length of objective of 3 mm, and water refractive index of $n_{water} = 1.33$).

3D Deconvolution is performed by ten iterations of 3D Lucy-Richardson

algorithm [112, 113] (deconvlucy function in MATLAB) to enhance resolution and decrease out of plane intensity contributions. Further, image noise is reduced using median filter function (medfilt2 function in MATLAB) applied on a neighborhood of 2×2 pixels in both lateral and axial directions.

Finally, according to the location of the first maximum intensity and full axial range obtained from the calibration measurement, we crop the common imaging volume among color channels to correct for minimal existing axial color aberration.

Next, we validate the volumetric 3-color capability of our system in imaging of fixed cells from the COS-7 cell line with three different fluorescently labeled intra-cellular structures: α -tubulin, vimentin, and F-actin.

3.4.3.4 Immunostaining of cells

Immunostaining: COS-7 (CRL-1651TM) cell line was purchased from American Type Culture Collection. Cells were grown on glass cover slips for 48 h, fixed in 3.6% formaldehyde in PBS for 15 minutes, washed with PBS, permeabilized with 0.5% Triton X – 100 in PBS for 10 minutes, and blocked with 3% BSA in PBS for 30 minutes at room temperature. Then, cells were incubated with mouse monoclonal anti- α -tubulin antibody (T6199, Sigma-Aldrich, 1 : 500) together with rabbit monoclonal anti-vimentin antibody (SP20, Invitrogen, 1 : 500) in 3% BSA in PBS for one hour. Subsequently, cells were washed once with 0.1% Tween20 in PBS and then thrice with PBS. Afterward, cells were incubated with FITC-conjugated goat anti-mouse IgG (F0257, Sigma-Aldrich, 1 : 1000) together with TRITC-conjugated goat anti-rabbit IgG (ab7051, Abcam, 1 : 1000) and phalloidin-Atto 647 (ATTO-TEC GmbH, 100 nM) in 3% BSA in PBS for one hour. After immunostaining, cells were washed once with 0.1% Tween 20 in PBS, thrice with PBS, and rinsed with distilled water. The samples were mounted on glass slides using FluoroshieldTM (F6182, Sigma-Aldrich). Sample preparation was carried out by *Eugenia Butkevich*.

3.4.4 Results

In Fig. 3.43 a, b and c, we present a transverse slice as well as a lateral view of imaging volume, $40 \mu\text{m} \times 40 \mu\text{m} \times 2.5 \mu\text{m}$, corresponding to α -tubulin in green, vimentin in magenta and F-actin in red of a fixed COS-7 cell simultaneously acquired by multi-plane multi-color system. Vimentin is transported along microtubules, which results in their co-localization. This can be clearly observed from their close intensity distribution in Fig. 3.43a , b. Fig. 3.43d indicates an overlay of three color channels in the same view sections as a, b, and c.

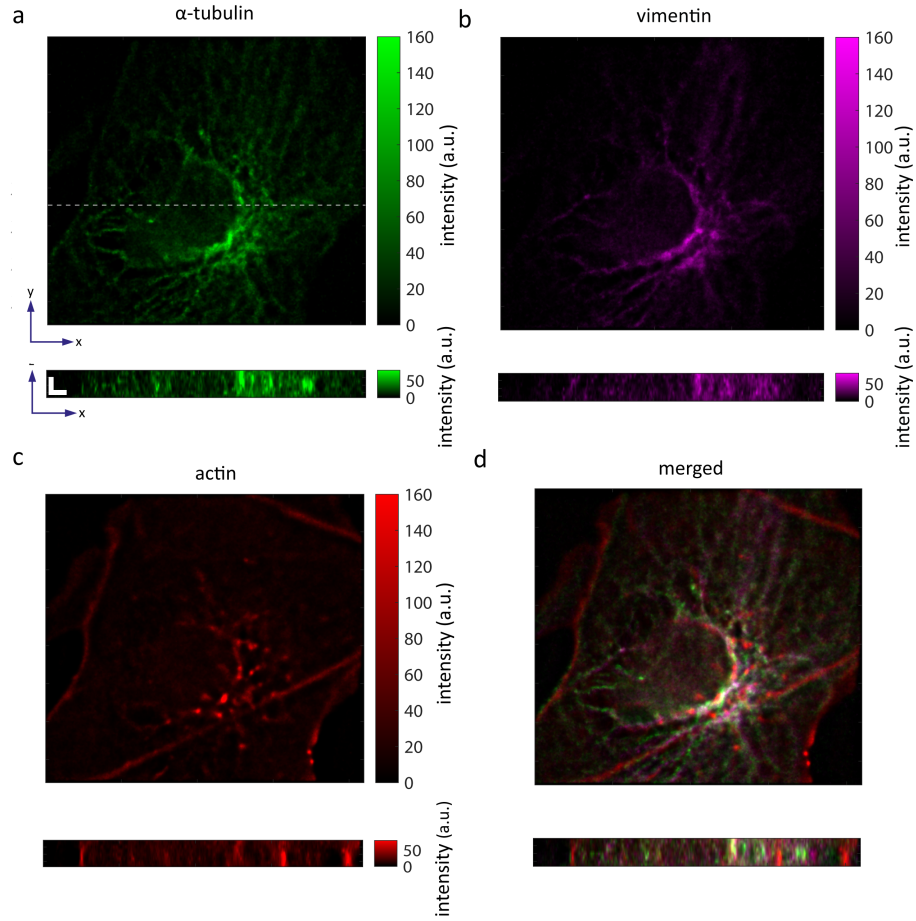


Figure 3.43: Instant 3D 3-color imaging of a fixed COS-7 cell. (a) α -tubulin imaged through the green channel in a xy section (upper image) and a xz section along the white dashed line highlighted in the transverse image (lower image). (b), (c) the same views as (a) for vimentin and F-actin imaged respectively through orange and red channels. (d) overlay of three color channels. Scale bars in lateral view in (a) indicates a length of $2\ \mu\text{m}$ in both x and z directions.

Besides a minimal spectral cross-talk among recorded species, lateral views in Fig. 3.43 indicate the different distribution of each cellular component along the depth of the sample.

In particular, F-actin represents a more flat (2D) distribution compared to α -tubulin and vimentin.

3.4.5 Discussion

We experimentally calibrate and realize an instant volumetric 3-color fluorescence imaging with minimal axial color aberration. Besides state-of-the-art high-quality optical components today, the successful realization of this high throughput microscope is partly due to the smart optical design, particularly ease of implementation and the

low axial color aberration of the multi-plane prism. The temporal resolution of our method is principally restricted only by camera speed. Our system exploits sCMOS cameras more efficiently than existing multi-plane single-color systems [14, 15, 19] since it uses nearly three fourth of all pixels available in both sCMOS cameras.

Moreover, this imaging system significantly simplifies technical demands and required hardware for simultaneous 3D multi-color microscopy compared to the only existing 3D dual-color method [14].

It has been shown that spectral sampling can be enhanced by correlation analysis between intensities of two color channels in a dual-color super-resolution optical fluctuation image (SOFI) where the sample needs to be labeled by blinking fluorophores [164]. Thus, one can aim for both higher spatial resolution and spectral sampling by incorporating our system to imaging multi-labeled samples with photo-switchable fluorophores.

In principle, one can implement deconvolution techniques or combine our method with different super-resolution approaches like SIM, dSTORM, and PALM to further improve spatial resolution. Although this will be either in the cost of time-consuming and complex image processing or lower temporal resolution compared to the proposed imaging system.

The axial range of imaging volume is a function of axial magnification of the imaging system. Thus, for a case-specific application, the volume size can be tuned to deeper or thinner width by a change in magnification. Further, the wavelength range of spectral bands can be easily altered by appropriate selection of multi-band pass dichroic, long-pass, and emission filters. One needs to check the optical performance of dichroic and long-pass filters to avoid significant axial color aberration through spectral channels.

Our method is promising to be implemented in various applications. In particular, it enables volumetric investigation of interactions between multiple species at the same time.

Multi-plane has been also successfully used in super resolution techniques [165]. In 2013, Bassam et al incorporated the grating based multi-plane system in sequential 3D acquisition of two colors in STORM. However, by the combination of a 3-color prism based system with a super resolution method, one can obtain a much simpler technique yet with higher throughput and SNR than the technique mentioned.

DUAL COLOR EPI-FLUORESCENCE LED IMAGE SCANNING MICROSCOPY

The initial goal of this project was the implementation of image scanning microscopy (ISM) with incoherent illumination on a multi-plane microscope to achieve a 3D ISM image with isotropic resolution enhancement in all spatial directions. However, in the midway of theoretical calculations, it turned out that the low coherence of LED light prevents significant axial resolution enhancement.

Nevertheless, we came across a new idea to conduct simultaneous dual-color ISM on a wide-field microscope using an incoherent LED light source. The concept, performance, and advantages of dual-color LED-ISM will be discussed in detail in the following sections. Moreover, we examine the performance and application of our method in biomedical imaging. A manuscript has been written presenting the results of this chapter.

4.1 INTRODUCTION

Different electron microscopy versions permit investigation of ultra-fine structures with extraordinarily high resolution better than 50 nm. However, these methods are mostly applicable only in structural and topographical studies due to the special conditions required for microscope performance like imaging in high vacuum and in environments free of vibration, magnetic, and electric interference.

For instance, usually in scanning electron microscopy (SEM), the sample needs to be coated with conductive materials like gold or carbon to conduct the electron beams. As another example, in transmission electron microscopy (TEM), the sample of interest has to have particular and typically tiny dimensions (< 100 nm of thickness) since electrons need to pass through the sample [166]. These particular conditions impede broad usage of electron microscopes, especially in non-invasive and fast studying of bio-specimens, where a bio-friendly environment is often required.

Among other microscopic techniques, optical microscopy is typically easier to implement, inexpensive, and fits more to bio-conditions.

In SIM, the sample is excited via diffraction-limited periodic patterns in different orientations to extend the cutoff spatial frequencies existing in the recorded images. These patterns are shifted along each orientation to cover the entire sample. Afterward, corresponding recorded emission patterns are imported in a reconstruction software

to obtain a super-resolved image with nearly doubled resolution. [37].

Resolution improvement by a factor of two can be pushed more up to a factor of four, resulting in ≤ 50 nm of spatial resolution when one uses high power excitation light. In this regime, the emission rate of fluorescent molecules does not linearly respond to the excitation power any longer. Thus, resolution enhancement will be experimentally limited only by photo-stability and strength of the emission signal [167]. A good review of various SIM methods and their applications is presented in the Ref [168].

ISM, experimentally presented by Müller and Enderlein [39], is principally close to SIM but it is technically less demanding compared to SIM. It can be experimentally realized on both confocal [40] and epi-fluorescence microscopes [41].

In the confocal-based version, instead of typical 1D stripe patterns in SIM, the sample is excited by stroboscopic illumination through a confocal spinning disk (CSD) microscope, a technique so-called confocal spinning-disk image scanning microscopy (CSDISM) [40]. CSDISM has the core advantage of confocal systems, i.e., optical sectioning capability, but suffers from poor temporal resolution.

In wide-field based systems, sparse and regular 2D multi-point patterns generated via digital micro-mirror device (DMD) illuminates sample [41], initially named as 'multi-focal SIM', which enhances the temporal resolution of the system but intrinsically lacks the optical sectioning capability of CSDISM. However, to some extent, one can obtain the sectioning capability in wide-field ISM by introducing of digital pinholes for emission spots in image analysis software.

Acquisition speed, i.e., temporal resolution in this context, has been further improved maximally up to 100 Hz, in a method so-called 'instant SIM', based on the core idea of rather an optical rendering of ISM image instead of computational post-processing [169]. The idea of an all-optical ISM system was initially configured on a confocal based microscope comprised of a pinhole array for blocking out of plane fluorescence associated with two micro-lens arrays together. One micro-lens array generates multi-spot excitation, whereas the other one demagnifies the fluorescence passed through the pinhole array by a factor of $2x$ and images that onto a camera. A galvo mirror quickly scans the beam to sum it up on the camera. Demagnification is the key to correctly sum up emission signals on camera, which readily provides a super-resolved image and no need to store a lot of data and post-processing. However, many optical elements involved in the detection path make this system costly, expensive to maintain, and trades for the SNR level, which governs the sufficient acquisition speed.

One can enhance the resolution of ISM further by its combination with other super-resolution methods or using nonlinear photo-response

of fluorophores [170]. For example, Tenne and coworkers combined ISM and SOFI by performing of ISM on samples labeled by blinking fluorophores (Quantum dots), which enabled exceeding the typical resolution of ISM experimentally nearly to two-fold [171].

Gregor et al. implemented ISM on a two-photon excitation microscope and obtain a super-resolved image with a penetration depth of 100 μm inside a sample [172].

Very recently, Castello et al. integrated ISM with fluorescence lifetime imaging microscopy (FLIM) by incorporation of a single-photon avalanche diode (SPAD) detection array instead of a typical camera and obtained time-resolved ISM results [173].

In all the existing ISM implementations, typically coherent laser sources are used for excitation which are costly. Moreover, wide-field based ISM microscopes often suffer from speckle noise in their recorded images. More importantly, one can conduct only single color imaging at a time using current laser-based techniques in both confocal and wide-field ISM cases. This is due to the fact that either simultaneous multi-color structured illumination or spectral unmixing in the detection path is not trivial and makes the current setups too complicated. For example, in 'multi-focal SIM', the sample is illuminated in a wide-field fashion only with a single laser color at a time because the grating structure of DMD induces chromatic aberration resulting in different output direction for each excitation wavelength. As another example, in 'instant SIM', the insertion of a spectral unmixing unit into its detection path makes such a system very sophisticated. Overall, despite a considerable effort made to develop ISM, this technique has been limited to the usage of coherent light sources, which inherently induces speckle noise. Secondly, laser sources' exploitation is not affordable for many biomedical applications, whereas, as a general imaging method, ISM is potentially extendible to incoherent and relatively inexpensive light sources. Thirdly, and more importantly, instant multi-color illumination is typically challenging when one employs laser sources. This is due to the fact that the optical phase modulators like SLM and DMD have a grating nature, i.e., coherent beam orientation modulated by these devices is highly wavelength dependent.

In 2013, Dan et al. showed that the exploitation of an incoherent light source in SIM could significantly reduce the cost and complexity of the imaging system and render speckle-noise free images [174, 175].

In this work, we develop an inexpensive simultaneous dual-color ISM system based on LED illumination, which can be easily exploited as a simple, super-resolution add-on to conventional epi-fluorescence microscopes. We examine this system's imaging performance and

resolution in detecting fluorescent beads, calibration Argo-SIM patterns, and fixed Vero cells with two different structures labeled.

4.2 METHODS

4.2.1 DMD-based incoherent ISM setup

Fig. 4.1 illustrates the proposed DMD-based incoherent image scanning system. Structured illumination is performed in a straightforward manner via a fiber-coupled LED light source, an expander lens, DMD, and a collimating lens. Compared to laser-based techniques, undemanding alignment and low number of components involved in our technique significantly alleviates its application and affordability to be used as a simple add-on to a conventional epi-fluorescence microscope.

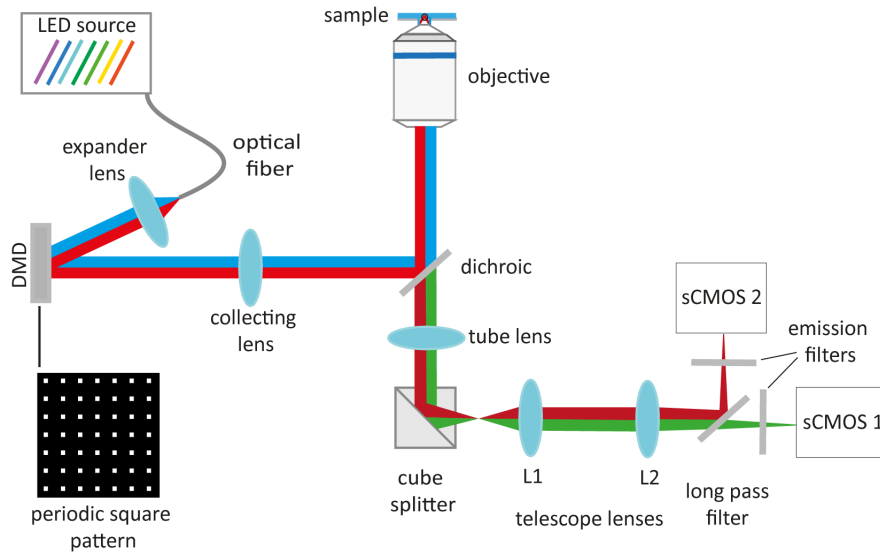


Figure 4.1: Dual-color DMD-based LED image scanning microscopy. The DMD is illuminated with an expanded fiber-coupled LED light with switchable wavelengths. Periodic patterns displayed on DMD are demagnified 100 times using the collimating lens and microscope objective and relayed onto the sample plane. Fluorescence signals are independently detected using two sCMOS cameras. The L1 and L2 denote the lenses of the 4f telescope system with $f_{L1}=150$ mm and $f_{L2}=200$ mm accordingly. Two co-path excitation wavelengths are colored in cyan and red, whereas the corresponding fluorescence wavelengths are colored in green and dark red.

We applied a low coherent LED source (Spectra X light engine, Lumencore) for excitation with seven switchable wavelengths. LED-illumination provides a speckle-noise free light source and benefits

from co-aligned wavelengths in the same path. For an even illumination, the LED light is spatially filtered with coupling to an optical fiber and expanded using a positive lens ($f_e=50$ mm). A collective/-collimating lens with 1.67x magnification, ($f_c=300$ mm), together with a 60x water immersion objective (Olympus), demagnifies the DMD pixels pitch of $7.56\text{ }\mu\text{m}$ on the DMD down to 77 nm projected onto the sample plane which is well below the Nyquist sampling values, i.e., $\lambda_{exc}/4NA$, which corresponds to 98 nm and 133 nm for cyan (470 nm) and red (640 nm) respectively. λ_{exc} and NA denote excitation wavelength and numerical aperture, accordingly. Likewise, for the sampling of the fluorescence signal, the lateral magnification of detection path comprised of objective magnification combined with a telescope system renders $\sim 82\text{ nm}$ effective camera pixel size, which fulfills the detection sampling rates, with $\sim 108\text{ nm}$ and $\sim 144\text{ nm}$, for green and red emission wavelengths correspondingly.

DMD performs like a double state reflector as it can be tilted along its diagonal in two different angles: $+12^\circ$ tilt angle (pixels on) reflects light toward the optical axis and -12° tilt angle (pixels off) reflects light away from the optical axis. We position our DMD (model DLP6500FLQ, Texas Instruments) in a conjugated plane of the sample plane and illuminate it with 12° angle with respect to the optical axis, which, therefore, it can be considered as a typical reflector for normal illumination in all-on pixel status.

Overall, 100 binary square patterns with the same period in each lateral direction are encoded sequentially by DMD software with 100 ms of exposure time and 5 ms time lag between patterns to thoroughly scan the entire sample (see section 4.2.3 for image acquisition). The fluorescence signal is back-reflected through the objective, then passed through a dichroic filter for band-pass separation. Two perpendicularly positioned sCMOS cameras (sCMOS OrcaFlash4 V2, Hamamatsu) are externally triggered as slaves of DMD for image acquisition. Details on setup components can be found in section B.5.

4.2.2 Chromatic aberration check

To check the chromatic aberration, we excited tetra spectral beads of 100 nm diameter ($0.1\text{ }\mu\text{m}$ TetraSpeck micro-spheres, ThermoFisher scientific) with $470/24\text{ nm}$ and $640/30\text{ nm}$ LED lights. Corresponding overlaid emissions in $520/35\text{ nm}$ and $685/75\text{ nm}$ imaged by our proposed system are shown in Fig. 4.2. Negligible chromatic aberration (chromatic shift smaller than one PSF size in FWHM) of the imaging system is observable.

Furthermore, three different and far apart regions (highlighted in yellow boxes) across the image are considered to check how that minimal aberration looks in different regions of FOV. Linearity of the min-

imal color aberration can be readily evidenced throughout the entire FOV when one compares zoomed images shown in the right panel of Fig. 4.2, i.e. up (Fig. 4.2b), middle (Fig. 4.2c) and bottom (Fig. 4.2d) regions in FOV.

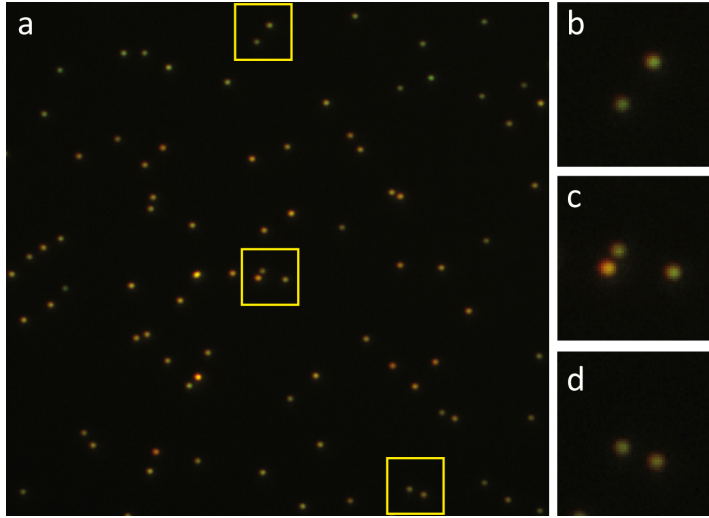


Figure 4.2: Chromatic aberration. The left panel, (a), shows the overlaid image of TetraSpeck fluorescent micro-spheres image emitting in 520/35 nm and 685/75 nm. (b), (c), and (d) are zoomed regions depicted as yellow boxes on top, middle, and bottom of (a) respectively.

4.2.3 Image acquisition

Micro-manager software controls the image acquisition of LED-ISM setup. Concerning precise localization of excitation spots in acquired images, we imaged highly concentrated Atto 488 and Atto 647N dye solutions each individually spin-coated with 4000 rotation per minute on two clean glass coverslides to make a thin and homogeneous reference sample correspondingly for green and red channels. We acquire reference images in order to localize the position of illumination spots precisely.

Fig. 4.3a, b display respectively the amplitude-only pattern encoded on the DMD panel and corresponding diffraction-limited image spots of a homogeneous fluorescence sample (Atto 488) emitting in 520/15 nm. As can be seen, the imaged illumination spots (Fig. 4.3b) are oriented in an angle of 45° with respect to the encoded patterns (Fig. 4.3a) which is due to the 45° angle of the micro-mirrors with respect to the incident light. 10 sequential shift of 'on' pixels are shown in Fig. 4.3a in each lateral dimension provides scanning the whole FOV. In other words, one needs to acquire 100 scan images to cover the whole FOV, which takes nearly ~ 10 seconds. One should note that the homogeneity of the illumination spots in the reference image is important for correctly detecting them via a position detecting software and finally for a homogeneous image reconstruction.

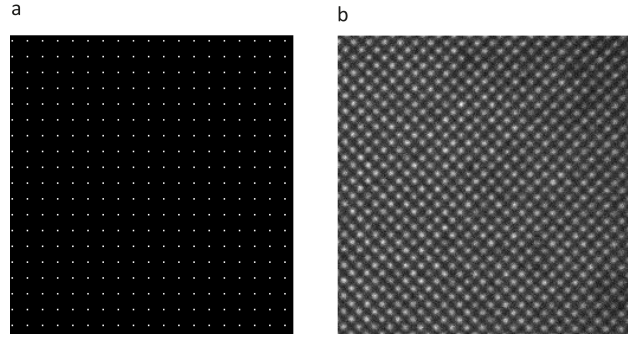


Figure 4.3: Periodic square illumination patterns. (a) An encoded periodic pattern on DMD. (b) The diffraction-limited emission spots corresponding to (a) imaged from a homogeneously spin-coated Atto 488 on a glass coverslip.

Fig. 4.4 represents the convolution of tubulin structure (Fig. 4.4a) with the illumination spots (Fig. 4.4b) which results in a modulated intensity of acquired images shown in Fig. 4.4c. The location of emission spots (highlighted as red dots in Fig. 4.4c) is determined via the 'rapidSTORM' software, which is then used as one input for image reconstruction.

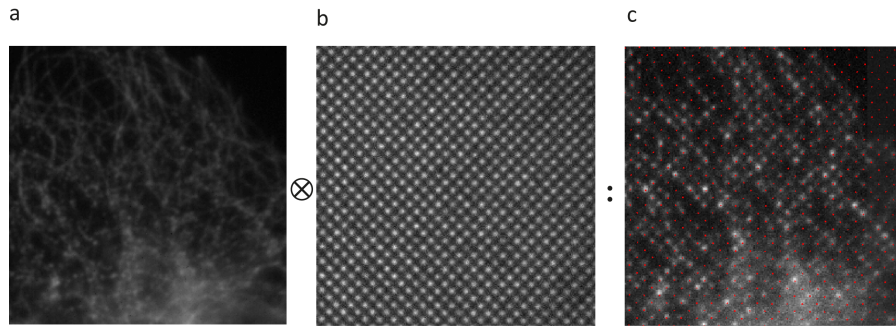


Figure 4.4: Sample intensity modulated with structured illumination. (a) A wide-field image of tubulin structure with emission at 520/25 nm (b) An illumination pattern (c) A tubulin structure illuminated by the periodic pattern. Red dots show the localized position of illumination spots.

4.2.4 Image reconstruction

Our procedure for ISM image reconstruction is described below.

1. Input the raw reference data in a rapidSTORM 3.3 software and set the software parameter for a pixel size equal to 82 nm and a PSF size equal to 375 nm at FWHM in order to detect the position of the excitation spots in reference images.
2. Make an empty image matrix with a size eight times the acquired image.
3. Crop the spots with a position r determined with rapidSTORM

software (shown as red dots in the Fig. 4.4c) and copy them in the position $2r$ in the final image matrix.

4. Repeat the procedure for all the 100 acquired scan frames.
5. Sum the images up and shrink the image size to the normal acquired image size.

The reconstruction process is schematically illustrated in Fig. 4.5. Let us assume we have four emitters, each located close to one corner of a wide-field microscope FOV, with a center located at a position r with respect to the FOV's center where r is smaller than the resolution limit of the exploited wide-field microscope. Secondly, let us suppose that one scans the whole FOV with only four scan images, each containing the PSF of only one emitter (Fig. 4.5a).

One can readily observe that the sum of the scan images, equivalent to an instantly acquired wide-field image, cannot resolve the emitters (Fig. 4.5b).

To reconstruct an ISM image in its simplest form, one needs to first make an empty image matrix with twice the number of pixels in the acquired raw (scan) images. Afterward, copy one single scan image with emitters centered at r and paste it at the position $2r$ in the already created image matrix, i.e., the ISM image. Repeating this process for all acquired scan images will fill in and reconstruct the final ISM image, which resolves the four emitters in the FOV (Fig. 4.5c). Finally, the ISM image should be converted to the physical size, i.e., the same size as the scan images (Fig. 4.5d).

Positioning accuracy of the emission spots is primarily limited to one pixel, which is only ≈ 4 times smaller than the number of pixels that cover a PSF spot. As a result, before the reconstruction, we upsample the number of pixels in raw images by a factor of 8 using `imresize` MATLAB function with 'bilinear' interpolation method to accurately obtain the position of image spots. This is quite important in image reconstruction quality. However, oversampling to a very large factor leads to a time-consuming image reconstruction while having only a minor influence on the localization accuracy. Image reconstruction was conducted using a MATLAB script developed by my colleagues, Jörg Enderlein, Olaf Schulz, and Sebastian Isbaner.

4.2.5 Preparation of fixed vero cells

Immunostaining: Vero cells (kidney cells of African green monkey) was purchased from American Type Culture Collection. Cells were grown on glass cover slips for 48 h, were fixed in 4% paraformaldehyde in PBS for 15 minutes, washed with PBS, permeabilized with 0.5% Triton X – 100 in PBS for 10 minutes, and blocked with 3% (w/v) BSA in PBS for 30 minutes at room temperature. Then, cells were incubated with mouse monoclonal anti-alpha-tubulin antibody (T6199, Sigma-Aldrich, 1 : 200) in 3% (w/v) BSA in PBS contain-

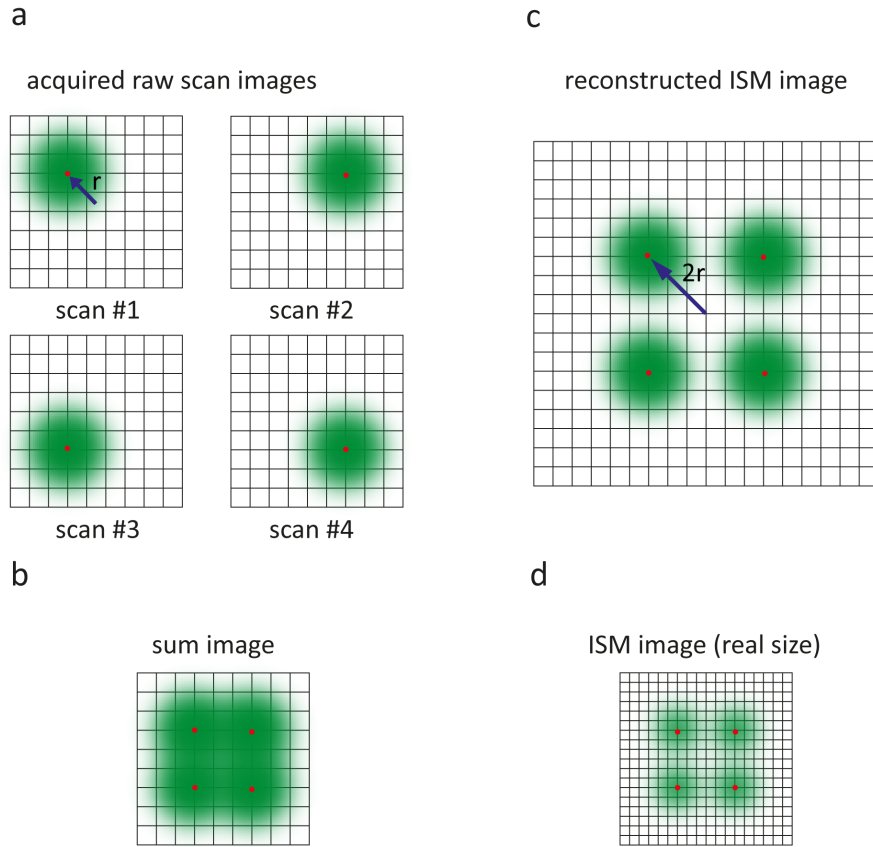


Figure 4.5: Reconstruction procedure of an ISM image. (a) Acquired raw scan images with the emitter centers positioned at r with respect to the image center (b) Sum of scan images (c) Reconstructed ISM image with emitter centers positioned at $2r$ in respect to the image center having a doubled number of pixels compared to the scan images (d) The same image as (c) but with the size of images in (a, b). The center of emitters is indicated with red dots.

ing 0.005% Triton-X 100 for one hour. Subsequently, the cells were washed three times in PBS for 10 minutes each, followed by a 1 h incubation with FITC-conjugated goat anti-mouse IgG (F0257, Sigma-Aldrich) together with Atto 550-phalloidin (AttoTec) diluted in 3% (w/v) BSA-PBS containing 0.005% Triton X-100. After immunostaining, again, cells were rinsed three times in PBS for 10 minutes each and one time with distilled water, and samples were mounted using Fluoroshield with DAPI (F6057, Sigma-Aldrich). *Eugenia Butkevich* carried out the sample preparation.

4.3 RESULTS

4.3.1 Example 1: fluorescent beads

As the first sample for ISM imaging, green and far-red fluorescent beads of 200 nm diameter (FluoSpheresTM Carboxylate Micro-spheres,

0.2 μm , yellow green fluorescent (505/515) and dark red fluorescent (660/680), Thermo Fisher Scientific) are mixed with the same concentration and spin-coated with 2000 r.p.m on a cleaned glass coverslip. We record 100 scan images from the sample and determine the localization of detection spots via *rapidSTORM* software [176]. Reconstruction of ISM images is described in section 4.2.4. The same procedure for image acquisition and reconstruction is implemented for the next two examples.

Fig. 4.6 depicts a comparison between average wide-field, LED-ISM, and deconvolved LED-ISM images of immobilized green and far-red emitting fluorescent beads. The lower panel of Fig. 4.6 exhibits the zoomed view from the region highlighted by the yellow dashed square in Fig. 4.6a. We chose the beads with excitation/emission spectrum far away from each other to check whether we can have homogeneous resolution improvement across a wide range of visible spectrum and check the existence of color aberration. As can be observed in Fig. 4.6b, LED-ISM image clearly shows resolution enhancement when compared to the conventional wide-field image (Fig. 4.6a).

Aberration-free PSF of microscope for each emission wavelength is calculated using the full wave-optical theory [103, 104] and the optical parameters of setup (emission wavelength λ_{peak} of 520 nm for green fluorescent bead, λ_{peak} of 685 nm for deep red fluorescent bead, NA of 1.2, image magnification of 80x, principal objective focal length of 3 mm, and water refractive index of $n_{water} = 1.33$). Using the calculated PSFs, LED-ISM images are deconvolved with ten iterations of Lucy-Richardson algorithm (deconvlucy function). Resolution has been further improved in deconvolved LED-ISM for both colors (Fig. 4.6c).

Moreover, the PSF shape of emitters has been well conserved in LED-ISM and deconvolved LED-ISM for both colors, demonstrating minimal artifact in image reconstruction.

The green and red emission wavelengths are spectrally separated using a long pass (580 nm) filter oriented with an angle of 45° with respect to the optical axis followed by band-pass emission filters for each color channel.

Fig. 4.7a, b are the cross-section plots of the green and far-red beads shown in Fig. 4.6 at FWHM of intensity. The red, blue, and green curves are the Gaussian fits to the measured intensity values (shown as dots with the same color) of wide-field, LED-ISM, and deconvolved LED-ISM correspondingly. Averaged over the width of Gaussian fits for ten beads, we obtained resolution improvement by a factor of ($\sim 1.32x$) for the LED-ISM and ($\sim 1.54x$) for the deconvolved LED-ISM images in the green channel. For the red channel, the corresponding resolution improvement factors are ($\sim 1.34x$) and ($\sim 1.54x$) accordingly for the LED-ISM and deconvolved LED-ISM images compared to the wide-field image.

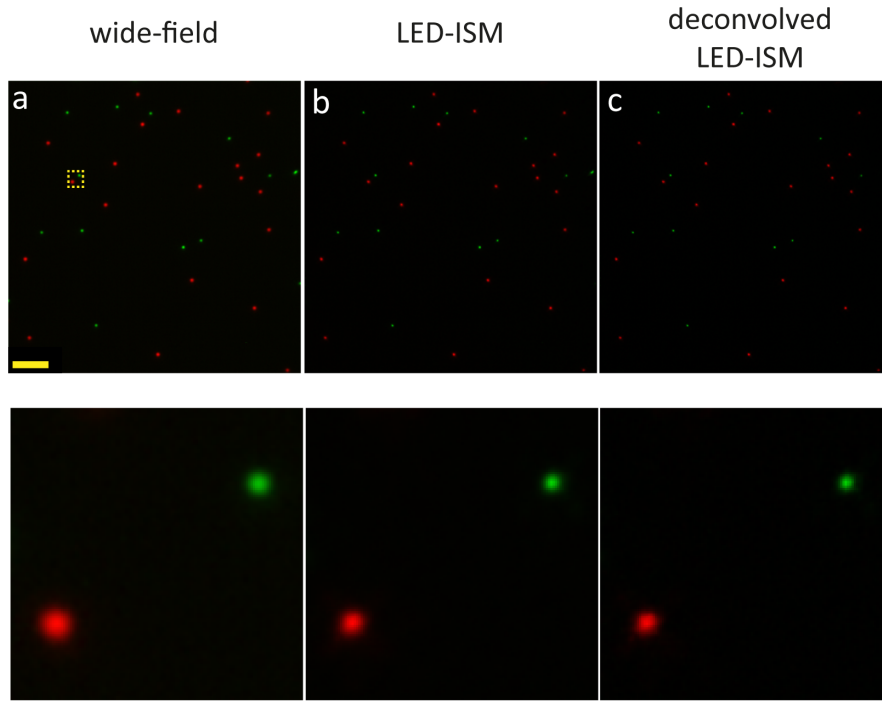


Figure 4.6: LED ISM of fluorescent green and far-red emitting beads of 200 nm diameter. (a) average wide-field image; (b) LED-ISM image; (c) deconvolved LED-ISM. Two single beads highlighted in the yellow square in (a) are zoomed and correspondingly shown below each panel. The scale bar in (a) indicates a length of 5 μm .

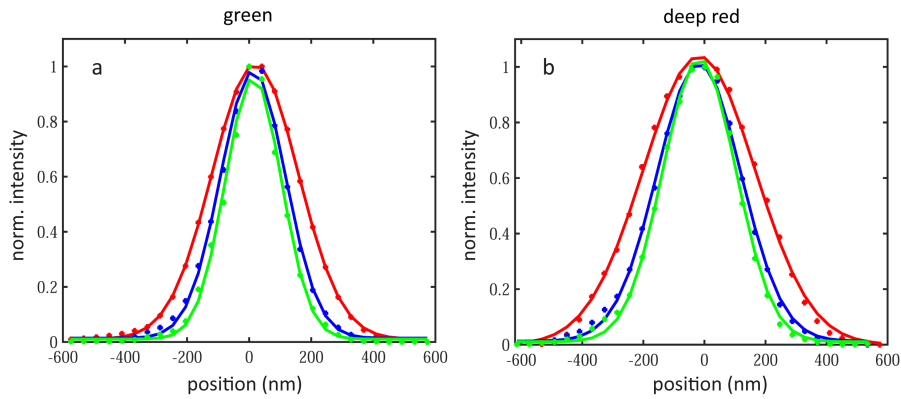


Figure 4.7: Intensity cross-section of (a) green and (b) far-red fluorescent beads shown in Fig. 4.6. Red, blue, and green curves indicate Gaussian fit to intensity data points respectively measured from wide-field, LED-ISM, and deconvolved LED-ISM bead images.

Close factors in both color channels indicate homogeneous resolution improvement across a broad range (~ 170 nm) of the visible spectrum. The improvement factor of 1.34x is close to the theoretical factor of 1.41x. Final experimentally achieved resolution improvement factors of 1.34 and 1.54 correspondingly do not match theoretical factors of $\sqrt{2}$ and 2, which is mainly due to the non-ignorable physical size of camera pixel size. In contrast, in the theory of ISM, detector pixel size

acts as an infinitesimally small pinhole. Further, in the case of deconvolved ISM, deviation from the ideal factor could also be because of limited SNR, the imperfection of optics, and the calculated PSF used in deconvolution from the ideal one. Last but not least, imaging of tetra spectral beads through color channels of our imaging system demonstrates its minimal chromatic aberration (see section 4.2.2).

4.3.2 Example 2: Argo SIM pattern 'E'

We imaged calibration fluorescence slide, typically used for SIM, so-called 'Argo-SIM' (Argolight), in particular the pattern E, which is made of parallel line pairs $\sim 36 \mu\text{m}$ long with gradually increasing distance between each line pair. Structured patterns are extensively used to assess the resolution and contrast of an imaging system due to their prior known size and geometry. Each column in Fig. 4.8 represents the image of pattern E as well as the corresponding zoomed region indicated in the yellow dashed square shown in Fig. 4.8a.

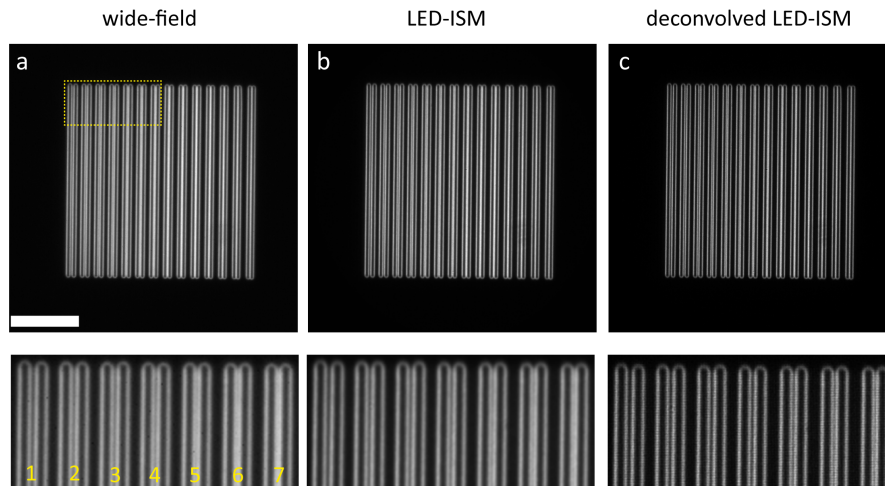


Figure 4.8: LED-ISM imaging of Argo-SIM pattern 'E'. (a) wide-field image from an array of pair doubled lines with gradually decreasing distance between doubled lines from left to right. (b, c) the same structure obtained by LED-ISM and deconvolved LED-ISM, respectively. Below each panel is the zoomed view from the corresponding region indicated in the yellow square in (a). The first seven pairs of the pattern are numbered below the panel (a).

Fig. 4.8a shows the wide-field image, whereas Fig. 4.8b, c are LED-ISM and deconvolved LED-ISM images, respectively. It is evident that contrast and resolution have improved in LED-ISM and further in deconvolved LED-ISM compared to the wide-field. Note that distance between pair structures (numbered in the bottom panel of Fig. 4.8a) is decreasing from left to right, which results in increasingly not resolving inner lines for pair structures as one move more toward the pair lines in the right of the pattern. For instance, in the bottom panel, one can observe that inner lines in pair number '5' are resolved in the

LED-ISM image compared to the same pair in the wide-field image. Likewise, the deconvolved LED-ISM can resolve even the inner lines of pair number '6' due to its higher resolution.

4.3.3 Example 3: fixed cells from the vero cell line

We examine the application of LED-ISM in simultaneous dual-color imaging of fixed Vero cells. Alpha-tubulin and actin structures of cells are labeled respectively with fluorescein isothiocyanate (FITC) and Atto 550 (see also section 4.2.5). We excited FITC by 470 nm and Atto 550 by 550 nm LED light. The sample is illuminated using 100 scan patterns, each with 100 ms exposure time, which renders total acquisition time of ≈ 10 seconds. Fig. 4.9a represents the wide-field image for the overlay of two color channels, i.e., alpha-tubulin in green (band-pass emission of 520 nm) and actin in red (band-pass emission filter of 585). Panel b in the same figure shows the corresponding LED-ISM image, which delivers higher contrast and resolution for both emission wavelengths than the wide-field image.

Fig. 4.9c exhibits the result of deconvolved LED-ISM. As can be observed in the upper panel and the corresponding zoomed region (indicated in a dashed yellow square) below each image, the image contrast and details increasingly improve from wide-field to ISM to deconvolved LED-ISM image.

Furthermore, in all three examples presented, one can observe a decent SNR, which demonstrates an appropriate number of photons collected in a typical exposure time of 100 ms. Moreover, images are free of speckle-noise as one of the significant advantages of using a LED light source compared to lasers. Further, LED-ISM is surprisingly affordable, and it significantly simplifies demands required for simultaneous multi-color super-resolution imaging as one can illuminate amplitude-only spatial light modulators simultaneously with different incoherent wavelengths.

4.4 CONCLUSION

In this work, the implementation of LED-ISM on a conventional epifluorescence microscope is proposed. Besides the speckle-noise free property of LED-ISM image, the overall resolution enhancement of 1.54x for deconvolved LED-ISM compared to a wide-field image was achieved. Simultaneous dual-color imaging in green and red emission wavelengths is performed with an acquisition speed of 0.1 Hz, which is almost more than five times faster than two sequential color acquisition by typical CSD-ISM with the same exposure time and FOV size.

LED-ISM can be regarded as one of the most inexpensive and straightforward ways to implement SRM techniques both in hardware and

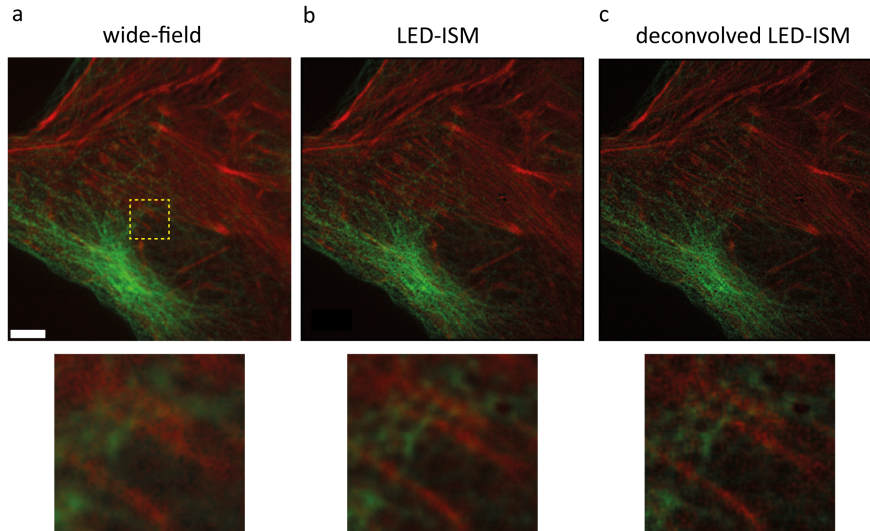


Figure 4.9: Comparison of dual-color wide-field, LED-ISM, and deconvolved LED-ISM image of alpha-tubulin and actin in a fixed cell from the *vero* cell line. (a) overlaid wide-field image of alpha-tubulin in green and actin in red, (b, c) same structures as (a) but correspondingly obtained from LED-ISM and deconvolved LED-ISM. The region highlighted in dashed yellow square in (a) is zoomed into and respectively shown in each lower panel result. The scale bar in (a) indicates a length of 5 μm .

software, which facilitates its application in conventional wide-field microscopes. Concerning the intrinsic property of ISM in enhancing resolution in all spatial dimensions, one can upgrade LED-ISM to 3D imaging by z-scanning sample or smart definition of illumination spots using a phase-only spatial light modulator (SLM). Compared to a DMD, SLM has one more degree of freedom in encoding information by phase patterns. Potentially, the encoded phase patterns generated by a SLM should contain the information about both the diffraction-limited 3D PSF of illumination spots as well as defined mask function for digital pinholes to provide optical sectioning.

CONCLUSION

In this thesis we realized four core methods: multi-plane phase-contrast microscopy, 3-color multi-plane fluorescence microscopy, multi-plane μ -particle tracking velocimetry, and dual-color LED wide-field image scanning microscopy.

In the first section of chapter 3, we showed how a multi-plane phase-contrast microscope allows performing long-time measurement of rapid dynamics of label-free living specimens in three spatial dimensions with an acquisition speed only limited to camera read-out. The combination of the phase contrast and multi-plane is synergistic because, firstly, the photobleaching issue like those in fluorescence methods is absent, which allows for long time imaging. Secondly, the common drawback of low SNR in multi-plane imaging systems is often less of concern in the optical-phase based methods than the fluorescence ones resulting in proper signal to noise ratio. In particular, we applied this microscope in real-time imaging of isolated *Chlamydomonas* axonemes swimming in the vicinity of a surface with a beating frequency of more than 70 Hz. This fruitfully resulted in the observation of non-zero torsion values in the axonemal motion, where the torsion exhibits a negative sign at the basal end, and it gradually changes its sign along the axonemal contour towards the distal end where it shows a positive sign.

Principally, using different imaging magnifications, one can exploit such a system as a robust and versatile tool in a non-invasive investigation of various unstained living specimens with a diverse range of physical dimensions. Using this imaging system together with the image processing presented, one can similarly investigate the rapid dynamics and behavior of sperm cells since they mostly have a rod-like shape close to *Chlamydomonas* axoneme in morphology which offers to implement alike PSF and a non-complex available deconvolution method like those used in this work.

In the second section, we demonstrate a suitable and promising application for a fluorescence multi-plane microscope, which is indeed 3D particle tracking velocimetry in a micro-scale regime. One can employ this method in monitoring in studying fluid flow and in the rapid protein dynamics research occurring in the millisecond regime.

In the third section, we experimentally presented how to straightforwardly enhance the specificity of a multi-plane fluorescence mi-

croscope by equipping that with a spectral unmixing unit providing three-color emission outputs with a minimal and correctable axial color aberration. We demonstrated the capability of such a system in instant 3-color imaging of fixed COS-7 cells in 3D. This method encompasses much broader applications where the understanding of the interaction between multiple components is desired. As an example, one can rapidly investigate in 3D the dynamics among nucleus, axon segments, and dendrites of a neuron, each labeled with a particular fluorophore.

Multi-plane imaging is still young, so there still exists enough room for extension of its applicability. One should wisely choose the application for multi-plane imaging. Although one can adjust and find a trade-off between spatial and temporal resolution simply by a change in camera exposure, an application which requires a sufficient spatial resolution in 3D but relatively high temporal resolution better matches to the nature and the principal concept behind this technique.

In chapter 4, we propose an easy-to-implement super-resolution add-on to a conventional wide-field microscope. Besides the speckle-noise free images, dual-color LED-ISM facilitates an instant structured illumination for multiple wavelengths, which is typically challenging for coherent lights because of chromatic aberration arisen from the grating nature of spatial light modulators. Further, a homogeneous resolution improvement factor of ~ 1.54 has been obtained for green and red emissions of a deconvolved LED-ISM image compared to a conventional wide-field image. We applied this imaging system in simultaneous dual-color imaging of fixed *vero* cells labeled with two different fluorophores.

Altogether, we hope that these techniques could pave the way for many researchers and accelerate plenty of new findings.

OTHER CONTRIBUTION

Besides my Ph.D projects, I have participated in another joint project. Here, I describe the adjustment and performance of a previously introduced infra-red based auto-focus system, so-called 'pgFocus', that I implemented that as an add-on to a Metal Induced Energy Transfer (MIET) microscope [177, 178] in order for automatic stabilization of a TIRF objective's focus during data acquisition. In particular, the main aim of the focus-stabilizer system is to assist the MIET microscope in measuring the dynamics of DNA hairpins summarized in the last section of this chapter.

Focus stabilization was controlled by a device so-called pgFocus (Biomedical Imaging Group, (pgFocus) [179]). The link mentioned provides detailed information about the hardware design and software of the stabilizer device. PgFocus is an open-source and open hardware focus stabilization device that autonomously adjusts a piezo-positioned objective in response to the positional change of a reflected NIR laser beam. PgFocus is able to modify and pass on piezo control signals from other devices, which allows pgFocus to identify the expected focus position and adjust accordingly. PgFocus operates at 30 Hz with ± 3 nm accuracy and integrates with μ Manager software.

A.1 AXIAL DRIFT CORRECTION USING INFRA-RED BASED FOCUS STABILIZER FOR MIET

Stabilization of a light microscope focus is necessary for optical bio-imaging, particularly when one requires to perform time-lapse imaging of living cells or in SMLM techniques where in-focus excitation light is critical to collect emission photons during acquisition efficiently. However, it is common that mechanical or thermal drift in the medium or small motion of components in the sample itself results in a drift in the objective's location with respect to the sample, which enormously degrades the quality of acquired data. Drift is often more pronounced along the optical axis than the lateral dimension. Moreover, any small axial drift leads to a significantly out-of-focus image when one uses a high NA objective with a short depth of field. Therefore, it is necessary to maintain the focal plane in a fixed position with respect to the sample throughout the experiment.

The setup implemented to this end is shown in Fig. A.1. A Near Infra-Red (NIR) diode laser is focused at the back focal plane of an oil immersion TIRF objective (NA 1.49, 100x) using a NIR convex

lens (AC254-400-B-ML, 650 - 1050 nm, Thorlabs) with a focal length of 400 mm. A dichroic mirror with a cutoff at 750 nm (FF750-SDi02-25x36, Semrock) is adjusted in a 45° with respect to the incident beam to direct the NIR laser to the edge of the objective pupil (back focal plane) so that the beam is back-reflected from the coverslide surface into the objective through total internal reflection (TIR).

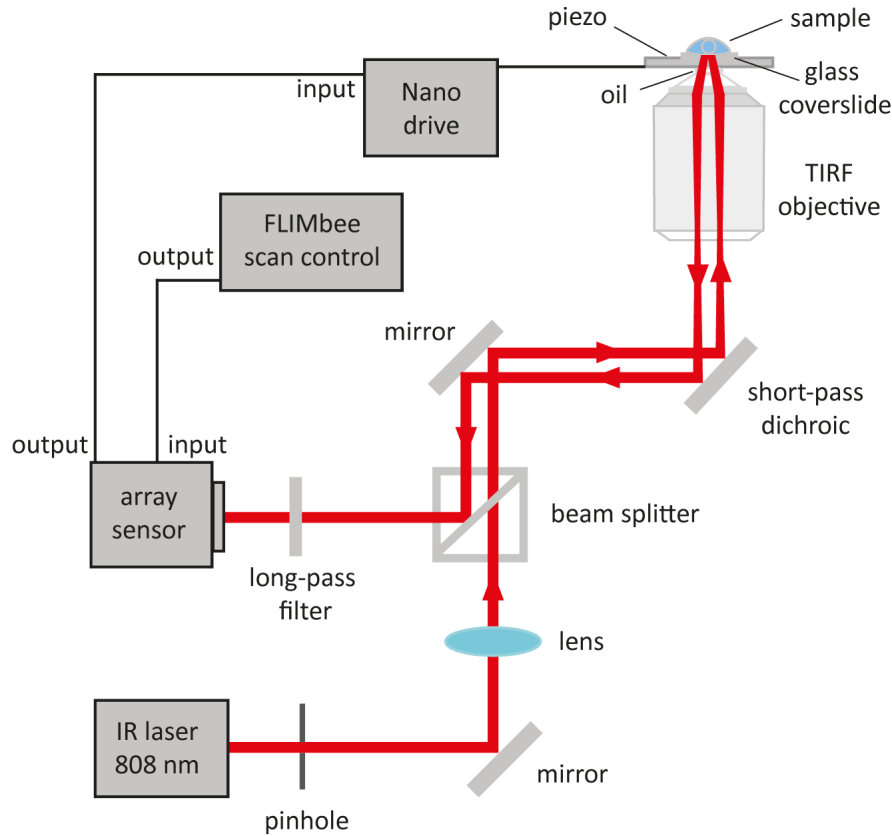


Figure A.1: NIR total internal reflection-based focus stabilizer. A NIR laser (with 808 nm wavelength) is focused at the back focal plane of a TIRF objective. This beam is back-reflected through the objective due to the high incidence angle and total internal reflection at the surface of the glass coverslide. The back-reflected light is directed to an array sensor. Any out-of-focus movement of the back-reflected light translates into a horizontal movement along the pixels of the array sensor. The initial in-focus position of the back-reflected light is set as the reference for the array sensor, which controls the axial position of the Nano drive piezo stage. The FLIMbee scanner is connected to the input of the array sensor to send the axial position information of the stage to the array sensor in case of a z-scan process. Two NIR mirrors, together with a dichroic mirror (with a cutoff at 750 nm) are used to align the beam path. A pinhole adjusts the beam size, and a long-pass filter with a cut-off at 800 nm blocks any fluorescence wavelength from the sample. The NIR beam-splitter separates the path of the incident and back-reflected beams.

Because the samples of interest are typically in an aqueous medium, one should do the alignment in the presence of a water droplet dripped onto the glass coverslip. More importantly, according to the *Snell's* law, total internal reflection depends on the refractive index of the sample's medium and the input beam's position on the objective's pupil, i.e., where the beam illuminates the rear plane. This law finds the refraction angle of light at the interface of two mediums with different refractive indices n_1 and n_2 . In case the incident light propagates from a medium with refractive index of n_1 to a medium with refractive index of n_2 where $n_2 < n_1$, the *Snell's* law implies that $\theta_{critical} = \sin^{-1}(\frac{n_2}{n_1})$ where $\theta_{critical}$ is a particular angle for the incident beam, which corresponds to the propagation of beam parallel to the interface between two mediums. Any angle larger than the critical angle leads to TIR at the interface between the glass coverslide and sample as depicted in Fig. A.1.

In detail, considering an equal refractive index for oil and glass (1.52), the critical angle for the aqueous and air medium is accordingly $\sim 61^\circ$ and $\sim 41^\circ$, which determine different objective pupil area for an incident beam. As already mentioned, the edge of the objective pupil is illuminated to ensure TIR. The back-reflected light is directed to a NIR beam-splitter, which reflects the beam towards an array sensor (pgFocus).

A long-pass filter with a cutoff wavelength at 800 nm (FEL0800, Thorlabs) passes only the NIR back-reflected light towards the array sensor. The reflected signal should be aligned at the center of the array sensor. As the beam is out of focus (microscope objective is displaced by the microscope knob with respect to the in-focus sample), one should observe a horizontal movement or sweep of the back-reflected light along the pixels of the array sensor. Receiving a voltage signal from the array sensor, the FLIMbee scan device (FLIMbee Galvo Scanner, PicoQuant) controls the axial position of the automated microscope stage (Nano-drive, single-axis MCL). The axial working distance of the array sensor is 20 μm with respect to the focal plane with ~ 5 nm localization precision. Two NIR mirrors (BB1-E03, 750 - 1100 nm, Thorlabs) are used for the beam alignment. An iris diaphragm with a dynamic aperture adjusts the beam size.

Fig. A.2 presents a photo of the illumination and detection block of the auto-focus system, which is positioned as a compact setup behind an IX73 microscope body (Olympus).

A.1.1 Some points about running the Auto-focus system

- The laser wavelength and the cutoff of the short-pass are selected to be far from those used typically as excitation/emis-

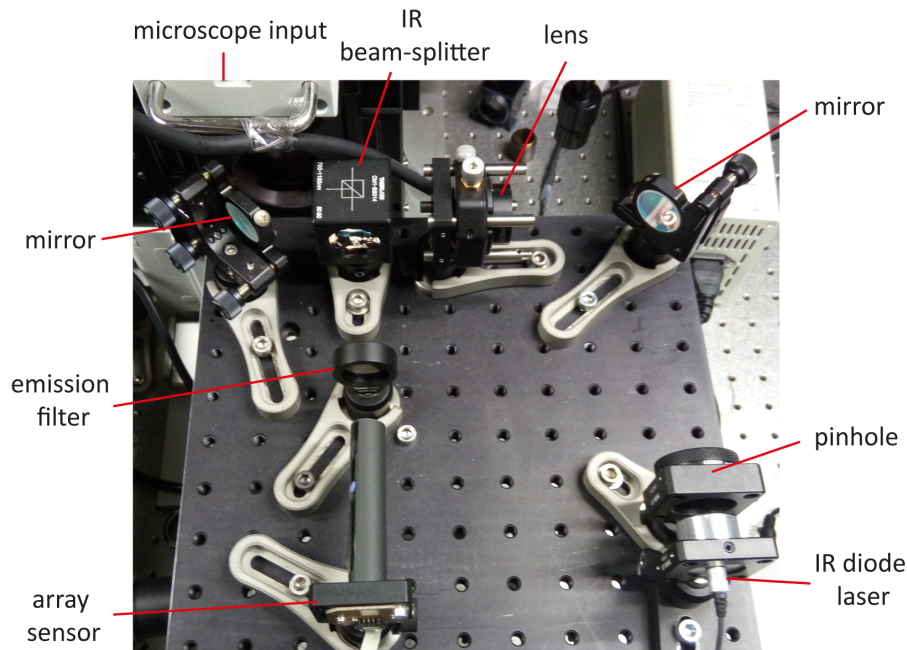


Figure A.2: Photo of the auto-focus setup.

sion wavelengths in SMLM or fluorescence microscopy. Thus, normally, the NIR laser light should not contribute or interfere with the emission signal collected by microscope cameras. However, one should exploit emission filters to ensure further minimizing the transmission of the NIR light.

- The auto-focus system has been calibrated for an aqueous medium on top of the glass coverslip with a thickness of 0.17 mm.
- The NIR laser and the array sensor should be kept on. When the message 'Cant find focus' pops up in the stabilization dialogue, one requires to recalibrate the system which is due to one the cases below: - The NIR laser path is blocked. - The TIRF objective is removed. - The microscope stage adapter (sample holders) are replaced - The axial position of the TIRF objective is shifted more than 20 μm .
- How to calibrate the auto-focus system? 1- Find the focus. 2- Run the pgFocus application installed on the computer running the microscope and z-scan drivers. 3- Navigate to Tools: serial Monitor. 4- Type 'f' in its tab above the window and press 'Enter'. This should readily switch OFF the auto-focus system. 5- Type 'c' and press 'Enter' to calibrate. One should observe that the focus profile keeps changing until the calibration process is finished. The changing intensity profile is due to the auto-focus system's serial commands to the piezo to scan the focus along the optical axis. The maximum intensity of the back-reflected NIR light on the array sensor has been defined as the intensity

of the in-focus position. 6- Type 'f' to switch ON the auto-focus system. Typically, the calibration process is done in less than ~ 30 s.

How to quickly check whether it works or not? Turn the microscope z-knob slowly in a small range (within -10 to $+10$ μm) to defocus. One should immediately see a spring-like movement of the focus, which corresponds to scanning around the focal plane while the auto-focus system is bringing the piezo back to the focal plane through an iterative loop.

A.2 DYNAMIET

In MIET and Graphene Induced Energy Transfer (GIET) [180], not only the fluorescence lifetime varies monotonously with distance, but also fluorescence intensity or brightness of the fluorophore is modulated. Fluctuations in fluorescence intensity due to quenching by the metal or graphene layer can be utilized for the quantitative investigation of dynamic processes in polymer chains as done in FCS. For this purpose, we combine scanning-FCS and MIET / GIET. This approach allows us to scan immobilized molecules tagged with a dye on a metal or graphene layer to extract various timescales of ongoing conformational dynamics. Currently, we implement this method to study the dynamics of DNA hairpins using MIET as the proof-of-concept.

The technique is called as dynamics using MIET or dynaMIET. Briefly, we use a DNA hairpin loop with its 5' end labeled with Atto 647N. The loop is attached to a dsDNA stalk and embedded into a DNA origami platform. This custom-designed origami platform is functionally immobilized on a passivated silicon dioxide spacer with a thin gold film beneath. Excitation and detection of fluorescence light are done through the substrate. The position of the fluorophore with respect to the gold layer changes due to the hairpin loop's opening and closing dynamics, hence modulating the fluorescence intensity. With dynaMIET, we simultaneously probe the two-state switching dynamics of the hairpin loop, which is in the order of ~ 1 ms, as well as the vertical diffusion of the DNA chain in its 'opened' state, which has been previously shown to occur in the order of hundreds of nanoseconds.

Till date, sm-FRET remains the technique of choice for probing chain dynamics. However, with FRET, the distance range one can probe is ≤ 10 nm due to the nature of dipole-dipole interactions. Furthermore, dynamics in the scale of nanoseconds can only be quantified with rigorous FRET-FCS measurements. Low yields of doubly-labeled samples in FRET is another challenging task. DynaMIET, which requires a single fluorophore labeled molecule has a working distance of ~ 150 nm, and can be efficiently utilized for probing chain dynamics

in any timescale slower than the fluorescence lifetime of the dye. We believe dynaMIET will find more suitable applications, especially for probing chain dynamics of intrinsically disordered proteins (IDPs), nucleic acids, and other polymers.

APPENDIX

B.1 ALIGNEMENT OF KÖHLER ILLUMINATION

Köhler illumination is adjusted to optimally defocus the light source for evenly exposing a sample across the entire FOV. Here, I briefly outline the workflow how to align a *Köhler* illumination followed by a phase-contrast imaging adjustment.

Step 1: Adjust the white light power to a low amount and open up both the condenser diaphragm and the field diaphragm to provide a large field of view with a non-intensive light.

Step 2: Focus on a sample using a low magnification objective while looking through the ocular to find the microscope's focal plane.

Step 3: Reduce the field diaphragm's opening and find it through the centering telescope lens of the observation tube. (this lens is indicated as 'CT' on the ocular turret in the Olympus IX71 microscope, which images the objective exit pupil).

Step 4: Change the axial position of the condenser lens until a sharp image of the field diaphragm is created. This ensures coinciding with the condenser focal plane to the objective's focal plane.

Step 5: Position the field diaphragm image in the middle of the FOV by the alignment of the lateral position of the condenser. This ensures the on-axis alignment of the illumination column with the optical axis of the objective.

Step 6- Increase the opening of the field diaphragm until the light covers the whole FOV as the last step of the *Köhler* illumination.

Step 7- Substitute the air objective with a high NA (60X/100X) phase objective and place the corresponding phase annulus (PH3) in the phase contrast turret.

Step 8- Look through the CT mode of ocular and adjust the phase annulus's lateral position in the center of FOV using the positioning screws of the phase annulus holder to obtain a phase image with the maximum contrast.

B.2 SPECIFICATIONS OF MULTI-PLANE PHASE-CONTRAST MICRO-SCOPE COMPONENTS

Component	Details
white light source	100W 12V Halogen Lamp U-LH100L-3, Olympus, peak wavelength ~ 585 nm
phase annulus	IX-PH3, 35 mm diameter, Olympus
condenser lens	IX2-LWUCD Universal Condenser, Olympus, NA 0.55, WD 27 mm
microscope stage	ES107IX2, Prior scientific instruments, 115 mm \times 77 mm travel range, 1 μ m step size resolution, OptiScan ES107 Controller
phase objective	UPLFLN 60XOIPH, 0.65 – 1.25 NA, Olympus
tube lens	$f_{TL} = 180$ mm, Olympus
field aperture	SP 40 slit, Owis
telescope lenses	$f_{L1} = 150$ mm, $f_{L2} = 200$ mm, achromatic doublets, AC254-150-A-ML, AC254-200-A-ML, Thorlabs
prism	Corning C-7980, $n_D = 1.458$, Abbe number $\nu = 67.8$, see section '6.2' in SI of Ref. [19]
camera	ORCA-Flash 4.0 V2, Hamamatsu, pixel size = 6.5 μ m

Table B.1: Specifications of components incorporated into the multi-plane phase-contrast microscope.

B.3 HARDWARE CONFIGURATION OF MULTI-PLANE PHASE-CONTRAST
MICROSCOPE

... installed on a computer is connected to two Hamamatsu camera (DCAM1 and DCAM2) which record image synchronously through Multi-camera option defined in Micro-Manager. In addition, a piezo z-scan stage model E753 is initialized in configuration occasional depth scan in case of system calibration.

SerialManager
Utilities, Multi Camera
HamamatsuHam-DCAM1
HamamatsuHam-DCAM2
PI-GCS-2, E-753

Table B.2: Hardware configuration devices for multi-plane imaging. Two cameras DCAM1 and DCAM2 synchronized by Multi-camera option together with a piezo z-scan stage model E753 are defined in configuration. COM6 indicates port number of computer.

COM6	AnswerTimeout	1000
COM6	BaudRate	115200
COM6	DelayBetweenCharsMs	0
COM6	Handshaking	Off
COM6	Parity	None
COM6	StopBits	1
COM6	Verbose	1
E-753	Port	COM6
PIZStage	Axis	1
PIZStage	Controller Name	E-753
PIZStage	Invert travel range	0
PIZStage	Limit-um	100
PIZStage	Stage	DEFAULT-STAGE

Table B.3: Initial setting parameters of configured devices in Micro-Manager for multi-plane imaging.

B.4 SPECIFICATIONS OF 3-COLOR MULTI-PLANE MICROSCOPE COMPONENTS

Component	Details
cyan laser	473 nm, 100 mW, CNI
green laser	561 nm, 200 mW, CNI
red laser	637 nm, 140 mW, Coherent, Obis
$7 \times$ broadband dielectric mirrors	BB1-E02, Thorlabs
long-pass dichroic beam-splitter	495 nm edge, Semrock
long-pass dichroic beamsplitter	593 nm edge, Semrock
diaphragm optical beam Shutter with controller	SHB1T- $\phi 1''$, Throlabs
objective	10 x, NA0.25
pinhole	diameter of $20\mu m$
collimating lens	$f_1 = 200$ mm, AC254-200-A-ML, Thorlabs
microscope stage	ES107IX2, Prior scientific instruments, $115\text{ mm} \times 77\text{ mm}$ travel range, $1\mu m$ step size resolution, OptiScan ES107 Controller
60 x fluorescence objective	UPLSAPO60XW, 1.2 NA, Olympus
Quad-band dichroic	Quad Line Beam-splitter R405/488/561/635 $\lambda/5$, Semrock
tube lens	$f_{TL} = 180$ mm, Olympus
field aperture	SP 40 slit, Owis
telescope lenses	$f_{L1} = 150$ mm, $f_{L2} = 200$ mm, achromatic doublets, AC254-150-A-ML, AC254-200-A-ML, Thorlabs
long-pass dichroic mirror	580 nm edge, Semrock
long-pass dichroic mirror	624 nm edge, Semrock
dichroic mirror 4	MGP01-(350-700) nm-25 x 36, Semrock
dichroic mirror 5	MGP01-(650-1300) nm-25 x 36, Semrock
$2 \times$ broadband dielectric mirrors	400-750 nm, Thorlabs
prism	Corning C-7980, $n_D = 1.458$, Abbe number $\nu = 67.8$, see section '6.2' in SI of Ref. [19]
camera	ORCA-Flash 4.0 V2, Hamamatsu, pixel size = $6.5\mu m$

Table B.4: Specifications of components incorporated into the 3-color multi-plane fluorescence microscope.

B.5 LED-ISM SETUP SPECIFICATIONS

Component	Details
Light source	lumencor SPECTRA X light engine, Input: 24 V at 5.0 A
Wavelengths	395, 440, 470, 510, 550, 575 and 640 nm
DMD	DLP6500FLQ, Texas Instruments
Expander lens	$f=50$ mm
Collecting lens	AC508-300-A-ML, $f=300$ mm, Thorlabs
Microscope stage	ES107IX2, 115 x 77 mm travel range, 1 μm step size resolution, OptiScan ES107 Controller (Prior scientific instruments)
Dichroic filter	AHF Analysentechnik, 446/523/600/677 HC Quadband Emitter
Tube lens	$f_{TL}=180$ mm, Olympus
Telescope lenses	$f_{L1}=150$ mm, $f_{L2}=200$ mm, achromatic doublets ARC: 400-700 nm, (AC254-150-A-ML, AC254-200-A-ML), Thorlabs
Camera	Orca Flash 4.0 (Hamamatsu), pixel size = 6.5 μm

Table B.5: Specifications of components incorporated into the LED-ISM setup.

BIBLIOGRAPHY

- [1] Juan Carlos Stockert and Alfonso Blázquez-Castro. *Fluorescence microscopy in life sciences*. Bentham Science Publishers, 2017.
- [2] Natan T Shaked, Zeev Zalevsky, and Lisa L Satterwhite. *Biomedical optical phase microscopy and nanoscopy*. Academic Press, 2012.
- [3] Tsung-Li Liu, Srigokul Upadhyayula, Daniel E Milkie, Ved Singh, Kai Wang, Ian A Swinburne, Kishore R Mosaliganti, Zach M Collins, Tom W Hiscock, Jamien Shea, et al. "Observing the cell in its native state: Imaging subcellular dynamics in multicellular organisms." In: *Science* 360.6386 (2018).
- [4] Yan-Jun Liu, Maël Le Berre, Franziska Lautenschlaeger, Paolo Maiuri, Andrew Callan-Jones, Mélina Heuzé, Tohru Takaki, Raphaël Voituriez, and Matthieu Piel. "Confinement and low adhesion induce fast amoeboid migration of slow mesenchymal cells." In: *Cell* 160.4 (2015), pp. 659–672.
- [5] Marco Polin, Idan Tuval, Knut Drescher, Jerry P Gollub, and Raymond E Goldstein. "Chlamydomonas swims with two "gears" in a eukaryotic version of run-and-tumble locomotion." In: *Science* 325.5939 (2009), pp. 487–490.
- [6] Misha B Ahrens, Michael B Orger, Drew N Robson, Jennifer M Li, and Philipp J Keller. "Whole-brain functional imaging at cellular resolution using light-sheet microscopy." In: *Nature methods* 10.5 (2013), pp. 413–420.
- [7] Dennis Gabor. "A new microscopic principle." In: *Nature* 161.4098 (1948), pp. 777–778.
- [8] Emil Wolf. "Determination of the amplitude and the phase of scattered fields by holography." In: *JOSA* 60.1 (1970), pp. 18–20.
- [9] Etienne Cuche, Frédéric Bevilacqua, and Christian Depeursinge. "Digital holography for quantitative phase-contrast imaging." In: *Opt. Lett.* 24.5 (1999), pp. 291–293.
- [10] Takahiro Ikeda, Gabriel Popescu, Ramachandra R Dasari, and Michael S Feld. "Hilbert phase microscopy for investigating fast dynamics in transparent systems." In: *Opt. Lett.* 30.10 (2005), pp. 1165–1167.
- [11] Yan Hu, Qian Chen, Shijie Feng, Tianyang Tao, Anand Asundi, and Chao Zuo. "A new microscopic telecentric stereo vision system-calibration, rectification, and three-dimensional reconstruction." In: *Optics and Lasers in Engineering* 113 (2019), pp. 14–22.
- [12] Marc Levoy, Ren Ng, Andrew Adams, Matthew Footer, and Mark Horowitz. "Light field microscopy." In: *ACM Trans. Graphics (TOG)* 25.3 (2006), pp. 924–934.

- [13] Jiamin Wu, Zhi Lu, Hui Qiao, Xu Zhang, Karl Zhanghao, Hao Xie, Tao Yan, Guoxun Zhang, Xiaoxu Li, Zheng Jiang, et al. "3D observation of large-scale subcellular dynamics in vivo at the millisecond scale." In: *bioRxiv* (2019), p. 672584.
- [14] Sara Abrahamsson, Jiji Chen, Bassam Hajj, Sjoerd Stallinga, Alexander Y Katsov, Jan Wisniewski, Gaku Mizuguchi, Pierre Soule, Florian Mueller, Claire Dugast Darzacq, et al. "Fast multicolor 3D imaging using aberration-corrected multifocus microscopy." In: *Nat. Methods* 10.1 (2013), p. 60.
- [15] Stefan Geissbuehler, Azat Sharipov, Aurélien Godinat, Noelia L Bocchio, Patrick A Sandoz, Anja Huss, Nickels A Jensen, Stefan Jakobs, Jörg Enderlein, F Gisou Van Der Goot, et al. "Live-cell multiplane three-dimensional super-resolution optical fluctuation imaging." In: *Nat. Communications* 5 (2014), p. 5830.
- [16] Michelle S Itano, Marina Bleck, Daniel S Johnson, and Sanford M Simon. "Readily accessible multiplane microscopy: 3D tracking the HIV-1 genome in living cells." In: *Traffic* 17.2 (2016), pp. 179–186.
- [17] Benjamin J Walker and Richard J Wheeler. "High-speed multifocal plane fluorescence microscopy for three-dimensional visualisation of beating flagella." In: *J. Cell Sci.* 132.16 (2019), jcs231795.
- [18] Erdal Toprak, Hamza Balci, Benjamin H Blehm, and Paul R Selvin. "Three-dimensional particle tracking via bifocal imaging." In: *Nano letters* 7.7 (2007), pp. 2043–2045.
- [19] A. Descloux et al. "Combined multi-plane phase retrieval and super-resolution optical fluctuation imaging for 4D cell microscopy." In: *Nat. Photonics* 12.3 (Feb. 2018), pp. 165–172.
- [20] Rolf Erni, Marta D Rossell, Christian Kisielowski, and Ulrich Dahmen. "Atomic-resolution imaging with a sub-50-pm electron probe." In: *Physical review letters* 102.9 (2009), p. 096101.
- [21] Weilun Chao, Bruce D Harteneck, J Alexander Liddle, Erik H Anderson, and David T Attwood. "Soft X-ray microscopy at a spatial resolution better than 15 nm." In: *Nature* 435.7046 (2005), pp. 1210–1213.
- [22] August Koehler. "New method of illumination for photomicrographical purposes." In: *JR Microscopical Soc* 14 (1894), pp. 261–262.
- [23] Patrick Michael Whelan and Michael John Hodgson. *Essential Principles Of Physics*. London, 1987.
- [24] David F Gruber, Hung-Teh Kao, Stephen Janoschka, Julia Tsai, and Vincent A Pieribone. "Patterns of fluorescent protein expression in scleractinian corals." In: *The Biological Bulletin* 215.2 (2008), pp. 143–154.
- [25] Dmitry A Shagin, Ekaterina V Barsova, Yurii G Yanushevich, Arkady F Fradkov, Konstantin A Lukyanov, Yulii A Labas, Tatiana N Semenova, Juan A Ugalde, Ann Meyers, Jose M Nunez, et al. "GFP-like proteins as ubiquitous metazoan superfamily: evolution of functional features and structural complexity." In: *Molecular biology and evolution* 21.5 (2004), pp. 841–850.

- [26] Carlos Taboada, Andrés E Brunetti, Federico N Pedron, Fausto Carnevale Neto, Dario A Estrin, Sara E Bari, Lucia B Chemes, Norberto Peporine Lopes, Maria G Lagorio, and Julián Faivovich. "Naturally occurring fluorescence in frogs." In: *Proceedings of the National Academy of Sciences* 114.14 (2017), pp. 3672–3677.
- [27] Osamu Shimomura, Frank H Johnson, and Yo Saiga. "Extraction, purification and properties of aequorin, a bioluminescent protein from the luminous hydromedusan, Aequorea." In: *Journal of cellular and comparative physiology* 59.3 (1962), pp. 223–239.
- [28] James G Morin and J Woodland Hastings. "Energy transfer in a bioluminescent system." In: *Journal of cellular physiology* 77.3 (1971), pp. 313–318.
- [29] Jörg Enderlein. "Advanced fluorescence microscopy." In: *Comprehensive Biomedical Physics* 4 (2014), pp. 111–151.
- [30] Prashant Prabhat, Sripad Ram, E Sally Ward, and Raimund J Ober. "Simultaneous imaging of different focal planes in fluorescence microscopy for the study of cellular dynamics in three dimensions." In: *IEEE Trans. Nanobiosci.* 3.4 (2004), pp. 237–242.
- [31] Jan N Hansen, An Gong, Dagmar Wachten, Rene Pascal, Alex Turpin, Jan F Jikeli, U Benjamin Kaupp, and Luis Alvarez. "Multifocal imaging for precise, label-free tracking of fast biological processes in 3D." In: *bioRxiv* (2020).
- [32] William J Shain, Nicholas A Vickers, Bennett B Goldberg, Thomas Bifano, and Jerome Mertz. "Extended depth-of-field microscopy with a high-speed deformable mirror." In: *Optics letters* 42.5 (2017), pp. 995–998.
- [33] J. F. Jikeli, R. Pascal, L. Alvarez, and R. Honnef. *Patent 102010049751*. 2010.
- [34] Stefan W Hell and Jan Wichmann. "Breaking the diffraction resolution limit by stimulated emission: stimulated-emission-depletion fluorescence microscopy." In: *Optics letters* 19.11 (1994), pp. 780–782.
- [35] Steffen J Sahl, Stefan W Hell, and Stefan Jakobs. "Fluorescence nanoscopy in cell biology." In: *Nature reviews Molecular cell biology* 18.11 (2017), p. 685.
- [36] Yaron M Sigal, Ruobo Zhou, and Xiaowei Zhuang. "Visualizing and discovering cellular structures with super-resolution microscopy." In: *Science* 361.6405 (2018), pp. 880–887.
- [37] Mats GL Gustafsson. "Surpassing the lateral resolution limit by a factor of two using structured illumination microscopy." In: *Journal of microscopy* 198.2 (2000), pp. 82–87.
- [38] CJ R SHEPPARD. "Super-resolution in confocal imaging." In: *Optik (Stuttgart)* 80.2 (1988), pp. 53–54.
- [39] Claus B Müller and Jörg Enderlein. "Image scanning microscopy." In: *Physical review letters* 104.19 (2010), p. 198101.

- [40] Olaf Schulz, Christoph Pieper, Michaela Clever, Janine Pfaff, Aike Ruhlandt, Ralph H Kehlenbach, Fred S Wouters, Jörg Großhans, Gertrude Bunt, and Jörg Enderlein. "Resolution doubling in fluorescence microscopy with confocal spinning-disk image scanning microscopy." In: *Proceedings of the National Academy of Sciences* 110.52 (2013), pp. 21000–21005.
- [41] Andrew G York, Sapun H Parekh, Damian Dalle Nogare, Robert S Fischer, Kelsey Temprine, Marina Mione, Ajay B Chitnis, Christian A Combs, and Hari Shroff. "Resolution doubling in live, multicellular organisms via multifocal structured illumination microscopy." In: *Nature methods* 9.7 (2012), pp. 749–754.
- [42] Azat Sharipov. *Multi-plane super-resolution microscopy*. Tech. rep. EPFL, 2017.
- [43] David L Ringo. "Flagellar motion and fine structure of the flagellar apparatus in *Chlamydomonas*." In: *The Journal of Cell Biology* 33.3 (1967), pp. 543–571.
- [44] Peter Satir and Søren Tvorup Christensen. "Overview of structure and function of mammalian cilia." In: *Annu. Rev. Physiol.* 69 (2007), pp. 377–400.
- [45] Khanh Huy Bui, Toshiki Yagi, Ryosuke Yamamoto, Ritsu Kamiya, and Takashi Ishikawa. "Polarity and asymmetry in the arrangement of dynein and related structures in the *Chlamydomonas* axoneme." In: *J. Cell Biol.* 198.5 (2012), pp. 913–925.
- [46] Jianfeng Lin and Daniela Nicastro. "Asymmetric distribution and spatial switching of dynein activity generates ciliary motility." In: *Science* 360.6387 (2018), eaar1968.
- [47] C. J. Brokaw and R Kamiya. "Bending patterns of *Chlamydomonas* flagella: IV. Mutants with defects in inner and outer dynein arms indicate differences in dynein arm function." In: *Cell Motil. Cytoskeleton* 8.1 (1987), pp. 68–75.
- [48] Jonathon Howard et al. "Mechanics of motor proteins and the cytoskeleton." In: (2001).
- [49] Adam Wanner, Matthias Salathé, and Thomas G O’Riordan. "Mucociliary clearance in the airways." In: *American journal of respiratory and critical care medicine* 154.6 (1996), pp. 1868–1902.
- [50] Eric R Brooks and John B Wallingford. "Multiciliated cells." In: *Curr. Biology* 24.19 (2014), R973–R982.
- [51] Ximena M Bustamante-Marin and Lawrence E Ostrowski. "Cilia and mucociliary clearance." In: *Cold Spring Harbor perspectives in biology* 9.4 (2017), a028241.
- [52] Regina Faubel, Christian Westendorf, Eberhard Bodenschatz, and Gregor Eichele. "Cilia-based flow network in the brain ventricles." In: *Science* 353.6295 (2016), pp. 176–178.

- [53] Nicola Pellicciotta, Evelyn Hamilton, Jurij Kotar, Marion Faucourt, Nathalie Degehyr, Nathalie Spassky, and Pietro Cicuta. "Synchronization of mammalian motile cilia in the brain with hydrodynamic forces." In: *bioRxiv* (2019), p. 668459.
- [54] Nobutaka Hirokawa, Yosuke Tanaka, Yasushi Okada, and Sen Takeda. "Nodal flow and the generation of left-right asymmetry." In: *Cell* 125.1 (2006), pp. 33–45.
- [55] David J Smith, Thomas D Montenegro-Johnson, and Susana S Lopes. "Symmetry-breaking cilia-driven flow in embryogenesis." In: *Annu. Rev. Fluid Mech.* 51 (2019), pp. 105–128.
- [56] CB Lindemann and KS Kanous. "Regulation of mammalian sperm motility." In: *Archives of andrology* 23.1 (1989), pp. 1–22.
- [57] Manabu Yoshida and Kaoru Yoshida. "Sperm chemotaxis and regulation of flagellar movement by Ca^{2+} ." In: *MHR: Basic science of reproductive medicine* 17.8 (2011), pp. 457–465.
- [58] Kazuo Inaba. "Sperm flagella: comparative and phylogenetic perspectives of protein components." In: *MHR: Basic science of reproductive medicine* 17.8 (2011), pp. 524–538.
- [59] Elizabeth H Harris. "Chlamydomonas as a model organism." In: *Annual review of plant biology* 52.1 (2001), pp. 363–406.
- [60] Veikko Geyer. "Characterization of the flagellar beat of the single cell green alga *Chlamydomonas reinhardtii*." PhD thesis. Sächsische Landesbibliothek-Staats-und Universitätsbibliothek Dresden, 2013.
- [61] Nathan L Hendel, Matthew Thomson, and Wallace F Marshall. "Diffusion as a ruler: modeling kinesin diffusion as a length sensor for intraflagellar transport." In: *Biophys. J.* 114.3 (2018), pp. 663–674.
- [62] Ron Orbach and Jonathon Howard. "The dynamic and structural properties of axonemal tubulins support the high length stability of cilia." In: *Nat. Communications* 10.1 (2019), p. 1838.
- [63] Mathieu Bottier, Kyle A Thomas, Susan K Dutcher, and Philip V Bayly. "How does cilium length affect beating?" In: *Biophys. J.* 116.7 (2019), pp. 1292–1304.
- [64] Giulia Bonente, Sara Pippa, Stefania Castellano, Roberto Bassi, and Matteo Ballottari. "Acclimation of *Chlamydomonas reinhardtii* to Different Growth Irradiances." In: *Journal of Biological Chemistry* 287.8 (Dec. 2011), pp. 5833–5847.
- [65] Nicoletta Liguori, Laura M. Roy, Milena Opacic, Grégory Durand, and Roberta Croce. "Regulation of Light Harvesting in the Green Alga *Chlamydomonas reinhardtii*: The C-Terminus of LHCSR Is the Knob of a Dimmer Switch." In: *Journal of the American Chemical Society* 135.49 (Nov. 2013), pp. 18339–18342.
- [66] Robert L Stavis and Rona Hirschberg. "Phototaxis in *Chlamydomonas reinhardtii*." In: *The Journal of cell biology* 59.2 (1973), pp. 367–377.

- [67] Sujeet Kumar Choudhary, Aparna Baskaran, and Prerna Sharma. "Reentrant efficiency of phototaxis in *Chlamydomonas reinhardtii* cells." In: *Biophysical journal* 117.8 (2019), pp. 1508–1513.
- [68] Jeffrey S Guasto, Karl A Johnson, and Jerry P Gollub. "Oscillatory flows induced by microorganisms swimming in two dimensions." In: *Phys. Rev. Lett.* 105.16 (2010), p. 168102.
- [69] T Cavalier-Smith. "Basal body and flagellar development during the vegetative cell cycle and the sexual cycle of *Chlamydomonas reinhardtii*." In: *Journal of cell science* 16.3 (1974), pp. 529–556.
- [70] Elizabeth H Harris, David B Stern, and George B Witman. *The chlamydomonas sourcebook*. Vol. 2. Academic Press San Diego, 1989.
- [71] Ursula Rüffer and Wilhelm Nultsch. "High-speed cinematographic analysis of the movement of *Chlamydomonas*." In: *Cell Motility* 5.3 (1985), pp. 251–263.
- [72] Dan Eshel and Charles J Brokaw. "New evidence for a "biased baseline" mechanism for calcium-regulated asymmetry of flagellar bending." In: *Cell motility and the cytoskeleton* 7.2 (1987), pp. 160–168.
- [73] Veikko F Geyer, Pablo Sartori, Benjamin M Friedrich, Frank Jülicher, and Jonathon Howard. "Independent control of the static and dynamic components of the *Chlamydomonas* flagellar beat." In: *Current Biology* 26.8 (2016), pp. 1098–1103.
- [74] Pablo Sartori, Veikko F Geyer, Andre Scholich, Frank Jülicher, and Jonathon Howard. "Dynamic curvature regulation accounts for the symmetric and asymmetric beats of *Chlamydomonas* flagella." In: *eLife* 5 (May 2016).
- [75] Kirsty Y Wan and Raymond E Goldstein. "Rhythmicity, recurrence, and recovery of flagellar beating." In: *Phys. Rev. Lett.* 113.23 (2014), p. 238103.
- [76] Susan K Dutcher. "Asymmetries in the cilia of *Chlamydomonas*." In: *Phil. Trans. Royal Soc. B* 375.1792 (2020), p. 20190153.
- [77] Raymond E Goldstein, Marco Polin, and Idan Tuval. "Noise and synchronization in pairs of beating eukaryotic flagella." In: *Phys. Rev. Lett.* 103.16 (2009), p. 168103.
- [78] Marco Polin, Idan Tuval, Knut Drescher, J. P. Gollub, and Raymond E. Goldstein. "*Chlamydomonas* swims with Two "Gears" in a Eukaryotic Version of Run-and-Tumble Locomotion." In: *Science* 325.5939 (July 2009), pp. 487–490.
- [79] Sumio Ishijima, Shigeru Oshio, and Hideo Mohri. "Flagellar movement of human spermatozoa." In: *Gamete Res.* 13.3 (1986), pp. 185–197.
- [80] Hermes Gadêlha, Paul Hernández-Herrera, Fernando Montoya, Alberto Darszon, and Gabriel Corkidi. "The human sperm beats anisotropically and asymmetrically in 3D." In: *bioRxiv* (2019), p. 795245.
- [81] Alon Greenbaum, Wei Luo, Ting-Wei Su, Zoltán Göröcs, Liang Xue, Serhan O Isikman, Ahmet F Coskun, Onur Mudanyali, and Aydogan Ozcan. "Imaging without lenses: achievements and remaining challenges of wide-field on-chip microscopy." In: *Nat. Methods* 9.9 (2012), p. 889.

- [82] Ting-Wei Su, Liang Xue, and Aydogan Ozcan. "High-throughput lensfree 3D tracking of human sperms reveals rare statistics of helical trajectories." In: *Proc. Nat. Acad. Sci. USA* 109.40 (2012), pp. 16018–16022.
- [83] F Merola, L Miccio, P Memmolo, G Di Caprio, A Galli, R Puglisi, D Balduzzi, G Coppola, P Netti, and P Ferraro. "Digital holography as a method for 3D imaging and estimating the biovolume of motile cells." In: *Lab on a Chip* 13.23 (2013), pp. 4512–4516.
- [84] Mustafa Ugur Daloglu and Aydogan Ozcan. "Computational imaging of sperm locomotion." In: *Biol. Reprod.* 97.2 (2017), pp. 182–188.
- [85] Jan F Jikeli, Luis Alvarez, Benjamin M Friedrich, Laurence G Wilson, René Pascal, Remy Colin, Magdalena Pichlo, Andreas Rennhack, Christoph Brenker, and U Benjamin Kaupp. "Sperm navigation along helical paths in 3D chemoattractant landscapes." In: *Nat. Communications* 6 (2015), p. 7985.
- [86] An Gong, Sebastian Rode, Ulrich Benjamin Kaupp, Gerhard Gompper, Jens Elgeti, Benjamin M Friedrich, and Luis Alvarez. "The steering gaits of sperm." In: *Phil. Trans. Royal Soc. B* 375.1792 (2020), p. 20190149.
- [87] Massimiliano Rossi, Giancarlo Cicconofri, Alfred Beran, Giovanni Noselli, and Antonio DeSimone. "Kinematics of flagellar swimming in *Euglena gracilis*: Helical trajectories and flagellar shapes." In: *Proc. Nat. Acad. Sci. USA* 114.50 (2017), pp. 13085–13090.
- [88] Laurence G Wilson, Lucy M Carter, and Sarah E Reece. "High-speed holographic microscopy of malaria parasites reveals ambidextrous flagellar waveforms." In: *Proc. Nat. Acad. Sci. USA* 110.47 (2013), pp. 18769–18774.
- [89] M Hines and JJ Blum. "Three-dimensional mechanics of eukaryotic flagella." In: *Biophys. J.* 41.1 (1983), pp. 67–79.
- [90] M E J Holwill, Howard J Cohen, and Peter Satir. "A sliding microtubule model incorporating axonemal twist and compatible with three-dimensional ciliary bending." In: *J. Exp. Biol.* 78.1 (1979), pp. 265–280.
- [91] Charles J Brokaw. "Computer simulation of flagellar movement VIII: coordination of dynein by local curvature control can generate helical bending waves." In: *Cell motility and the cytoskeleton* 53.2 (2002), pp. 103–124.
- [92] Jens Elgeti, U Benjamin Kaupp, and Gerhard Gompper. "Hydrodynamics of sperm cells near surfaces." In: *Biophys. J.* 99.4 (2010), pp. 1018–1026.
- [93] Pablo Sartori, Veikko F. Geyer, Jonathon Howard, and Frank Jülicher. "Curvature regulation of the ciliary beat through axonemal twist." In: *Physical Review E* 94.4 (Oct. 2016).
- [94] Emil Wolf. "Three-dimensional structure determination of semi-transparent objects from holographic data." In: *Opt. Commun.* 1.4 (1969), pp. 153–156.
- [95] Wenbo Xu, M H Jericho, I A Meinertzhagen, and H J Kreuzer. "Digital inline holography for biological applications." In: *Proc. Nat. Acad. Sci. USA* 98.20 (2001), pp. 11301–11305.
- [96] Vincent Lauer. "New approach to optical diffraction tomography yielding a vector equation of diffraction tomography and a novel tomographic microscope." In: *J. Microsc.* 205.2 (2002), pp. 165–176.

- [97] Wonshik Choi, Christopher Fang-Yen, Kamran Badizadegan, Seungeun Oh, Niyom Lue, Ramachandra R Dasari, and Michael S Feld. "Tomographic phase microscopy." In: *Nat. Methods* 4.9 (2007), p. 717.
- [98] Zhuo Wang, Larry Millet, Mustafa Mir, Huaifeng Ding, Sakulsuk Unaruntai, John Rogers, Martha U Gillette, and Gabriel Popescu. "Spatial light interference microscopy (SLIM)." In: *Opt. Express* 19.2 (2011), pp. 1016–1026.
- [99] Michael Reed Teague. "Deterministic phase retrieval: a Green's function solution." In: *JOSA* 73.11 (1983), pp. 1434–1441.
- [100] Timur E Gureyev and Keith A Nugent. "Rapid quantitative phase imaging using the transport of intensity equation." In: *Opt. Commun.* 133.1-6 (1997), pp. 339–346.
- [101] Chao Zuo, Qian Chen, Yingjie Yu, and Anand Asundi. "Transport-of-intensity phase imaging using Savitzky-Golay differentiation filter-theory and applications." In: *Opt. Express* 21.5 (2013), pp. 5346–5362.
- [102] Xing Lin, Jiamin Wu, Guoan Zheng, and Qionghai Dai. "Camera array based light field microscopy." In: *Biomed. Opt. Express* 6.9 (2015), pp. 3179–3189.
- [103] Emil Wolf. "Electromagnetic diffraction in optical systems-I. An integral representation of the image field." In: *Proceedings of the Royal Society of London. Series A. Mathematical and Physical Sciences* 253.1274 (1959), pp. 349–357.
- [104] B Richards and E Wolf. "Electromagnetic diffraction in optical systems, II. Structure of the image field in an aplanatic system." In: *Proceedings of the Royal Society of London. Series A. Mathematical and Physical Sciences* 253.1274 (1959), pp. 358–379.
- [105] Claude Elwood Shannon. "Communication in the presence of noise." In: *Proceedings of the IRE* 37.1 (1949), pp. 10–21.
- [106] Branch Craige, Jason M Brown, and George B Witman. "Isolation of *Chlamydomonas* flagella." In: *Curr. Prot. Cell Biology* 59.1 (2013), pp. 3–41.
- [107] George B Witman. "[28] Isolation of *Chlamydomonas* flagella and flagellar axonemes." In: *Methods in enzymology*. Vol. 134. Elsevier, 1986, pp. 280–290.
- [108] Matthew Bessen, Rose B Fay, and George B Witman. "Calcium control of waveform in isolated flagellar axonemes of *Chlamydomonas*." In: *J. Cell Biol.* 86.2 (1980), pp. 446–455.
- [109] Joshua Alper, Veikko Geyer, Vikram Mukundan, and Jonathon Howard. "Reconstitution of flagellar sliding." In: *Methods in enzymology*. Vol. 524. Elsevier, 2013, pp. 343–369.
- [110] *Micro-Manager home page*. <https://micro-manager.org/>. Accessed: 2020-03-08.
- [111] Simon C Stein, Anja Huss, Dirk Hähnel, Ingo Gregor, and Jörg Enderlein. "Fourier interpolation stochastic optical fluctuation imaging." In: *Optics express* 23.12 (2015), pp. 16154–16163.

- [112] William Hadley Richardson. "Bayesian-based iterative method of image restoration." In: *JoSA* 62.1 (1972), pp. 55–59.
- [113] Leon B Lucy. "An iterative technique for the rectification of observed distributions." In: *The astronomical journal* 79 (1974), p. 745.
- [114] Chenyang Xu and Jerry L Prince. "Gradient vector flow: A new external force for snakes." In: *IEEE Proc. CVPR*. IEEE. July 1997, pp. 66–71.
- [115] Chenyang Xu, Jerry L Prince, et al. "Snakes, shapes, and gradient vector flow." In: *IEEE Trans. Image Proc.* 7.3 (1998), pp. 359–369.
- [116] Manfredo P Do Carmo. *Differential geometry of curves and surfaces: revised and updated second edition*. Courier Dover Publications, 2016.
- [117] James Lighthill. "Flagellar hydrodynamics." In: *SIAM review* 18.2 (1976), pp. 161–230.
- [118] JEREMY S Hyams and Gary G Borisy. "Isolated flagellar apparatus of *Chlamydomonas*: characterization of forward swimming and alteration of waveform and reversal of motion by calcium ions in vitro." In: *Journal of Cell Science* 33.1 (1978), pp. 235–253.
- [119] Jianfeng Lin, Kyoko Okada, Milen Raytchev, Maria C Smith, and Daniela Nicastro. "Structural mechanism of the dynein power stroke." In: *Nature cell biology* 16.5 (2014), pp. 479–485.
- [120] David M Woolley and Geraint G Vernon. "Alternating torsions in a living '9+ 2' flagellum." In: *Proc. Roy. Soc. London B: Biol. Sci.* 266.1425 (1999), pp. 1271–1275.
- [121] IR Gibbons. "The molecular basis of flagellar motility in sea urchin spermatozoa." In: *Society of General Physiologists series* 30 (1975), p. 207.
- [122] DM Woolley and GG Vernon. "A study of helical and planar waves on sea urchin sperm flagella, with a theory of how they are generated." In: *J. Exp. Biol.* 204.7 (2001), pp. 1333–1345.
- [123] Charlotte K Omoto and Ching Kung. "Rotation and twist of the central-pair microtubules in the cilia of *Paramecium*." In: *J. Cell Biol.* 87.1 (1980), pp. 33–46.
- [124] David R Mitchell. "Orientation of the central pair complex during flagellar bend formation in *Chlamydomonas*." In: *Cell Motil. Cytoskeleton* 56.2 (2003), pp. 120–129.
- [125] Shin Yamaguchi, Kei Saito, Miki Sutoh, Takayuki Nishizaka, Yoko Y Toyoshima, and Junichiro Yajima. "Torque generation by axonemal outer-arm dynein." In: *Biophys. J.* 108.4 (2015), pp. 872–879.
- [126] Ronald D Vale and Yoko Yano Toyoshima. "Rotation and translocation of microtubules in vitro induced by dyneins from *Tetrahymena* cilia." In: *Cell* 52.3 (1988), pp. 459–469.
- [127] Christian Cibert and Jean-Vivien Heck. "Geometry drives the "deviated-bending" of the bi-tubular structures of the 9+ 2 axoneme in the flagellum." In: *Cell Motil. Cytoskeleton* 59.3 (2004), pp. 153–168.

- [128] Sandor Kasas, András Kis, Beat Michel Riederer, László Forró, Giovanni Dietler, and Stefan Catsicas. "Mechanical properties of microtubules explored using the finite elements method." In: *ChemPhysChem* 5.2 (2004), pp. 252–257.
- [129] Y_ Yeh and HZ Cummins. "Localized fluid flow measurements with an He–Ne laser spectrometer." In: *Applied Physics Letters* 4.10 (1964), pp. 176–178.
- [130] Juan G Santiago, Steve T Wereley, Carl D Meinhart, DJ Beebe, and Ronald J Adrian. "A particle image velocimetry system for microfluidics." In: *Experiments in fluids* 25.4 (1998), pp. 316–319.
- [131] Carl D Meinhart, Steve T Wereley, and Juan G Santiago. "PIV measurements of a microchannel flow." In: *Experiments in fluids* 27.5 (1999), pp. 414–419.
- [132] Derek C Tretheway and Carl D Meinhart. "Apparent fluid slip at hydrophobic microchannel walls." In: *Physics of fluids* 14.3 (2002), pp. L9–L12.
- [133] Zhijun Wu, Zhiyong Zhu, and Zhen Huang. "An experimental study on the spray structure of oxygenated fuel using laser-based visualization and particle image velocimetry." In: *Fuel* 85.10–11 (2006), pp. 1458–1464.
- [134] Peter Vennemann, Kenneth T Kiger, Ralph Lindken, Bianca CW Groenendijk, Sandra Stekelenburg-de Vos, Timo LM ten Hagen, Nicolette TC Ursem, Rob E Poelmann, Jerry Westerweel, and Beerend P Hierck. "In vivo micro particle image velocimetry measurements of blood-plasma in the embryonic avian heart." In: *Journal of biomechanics* 39.7 (2006), pp. 1191–1200.
- [135] Jay R Hove, Reinhard W Köster, Arian S Forouhar, Gabriel Acevedo-Bolton, Scott E Fraser, and Morteza Gharib. "Intracardiac fluid forces are an essential epigenetic factor for embryonic cardiogenesis." In: *Nature* 421.6919 (2003), pp. 172–177.
- [136] Steven T Wereley and Carl D Meinhart. "Recent advances in micro-particle image velocimetry." In: *Annual Review of Fluid Mechanics* 42 (2010), pp. 557–576.
- [137] Ralph Lindken, Massimiliano Rossi, Sebastian Große, and Jerry Westerweel. "Micro-particle image velocimetry (μ PIV): recent developments, applications, and guidelines." In: *Lab on a Chip* 9.17 (2009), pp. 2551–2567.
- [138] Reza Sadr, Haifeng Li, and Minami Yoda. "Impact of hindered Brownian diffusion on the accuracy of particle-image velocimetry using evanescent-wave illumination." In: *Experiments in fluids* 38.1 (2005), pp. 90–98.
- [139] Ralph Lindken, Jerry Westerweel, and Bernhard Wieneke. "Stereoscopic micro particle image velocimetry." In: *Experiments in Fluids* 41.2 (2006), pp. 161–171.
- [140] William H Snyder and JL Lumley. "Some measurements of particle velocity autocorrelation functions in a turbulent flow." In: *Journal of Fluid Mechanics* 48.1 (1971), pp. 41–71.

- [141] Michael G Olsen and Ronald J Adrian. "Brownian motion and correlation in particle image velocimetry." In: *Optics & Laser Technology* 32.7-8 (2000), pp. 621–627.
- [142] LE Scriven and CV Sternling. "The marangoni effects." In: *Nature* 187.4733 (1960), pp. 186–188.
- [143] Hyungsoo Kim, François Boulogne, Eujin Um, Ian Jacobi, Ernie Button, and Howard A Stone. "Controlled uniform coating from the interplay of Marangoni flows and surface-adsorbed macromolecules." In: *Physical review letters* 116.12 (2016), p. 124501.
- [144] KC Mills, BJ Keene, RF Brooks, and A Shirali. "Marangoni effects in welding." In: *Philosophical Transactions of the Royal Society of London. Series A: Mathematical, Physical and Engineering Sciences* 356.1739 (1998), pp. 911–925.
- [145] D Schwabe and A Scharmann. "Some evidence for the existence and magnitude of a critical Marangoni number for the onset of oscillatory flow in crystal growth melts." In: *Journal of Crystal Growth* 46.1 (1979), pp. 125–131.
- [146] Hyungsoo Kim, Koen Muller, Orest Shardt, Shahriar Afkhami, and Howard A Stone. "Solutal Marangoni flows of miscible liquids drive transport without surface contamination." In: *Nature Physics* 13.11 (2017), pp. 1105–1110.
- [147] Stefan Karpitschka, Ferenc Liebigh, and Hans Riegler. "Marangoni contraction of evaporating sessile droplets of binary mixtures." In: *Langmuir* 33.19 (2017), pp. 4682–4687.
- [148] Yaxing Li, Christian Diddens, Pengyu Lv, Herman Wijshoff, Michel Versluis, and Detlef Lohse. "Gravitational effect in evaporating binary microdroplets." In: *Physical review letters* 122.11 (2019), p. 114501.
- [149] Stefan Karpitschka and Hans Riegler. "Quantitative experimental study on the transition between fast and delayed coalescence of sessile droplets with different but completely miscible liquids." In: *Langmuir* 26.14 (2010), pp. 11823–11829.
- [150] Simon Christoph Stein and Jan Thiart. "TrackNTrace: A simple and extendable open-source framework for developing single-molecule localization and tracking algorithms." In: *Scientific reports* 6.1 (2016), pp. 1–7.
- [151] Bernd Rieger and Sjoerd Stallinga. "The Lateral and Axial Localization Uncertainty in Super-Resolution Light Microscopy." In: *ChemPhysChem* 15.4 (2014), pp. 664–670.
- [152] Mark Kreizer, David Ratner, and Alex Liberzon. "Real-time image processing for particle tracking velocimetry." In: *Experiments in fluids* 48.1 (2010), pp. 105–110.
- [153] Yoshinori Hamamoto, John RE Christy, and Khellil Sefiane. "Order-of-magnitude increase in flow velocity driven by mass conservation during the evaporation of sessile drops." In: *Physical Review E* 83.5 (2011), p. 051602.

- [154] Eran Hershko, Lucien E Weiss, Tomer Michaeli, and Yoav Shechtman. "Multicolor localization microscopy and point-spread-function engineering by deep learning." In: *Optics express* 27.5 (2019), pp. 6158–6183.
- [155] Philippe IH Bastiaens and Anthony Squire. "Fluorescence lifetime imaging microscopy: spatial resolution of biochemical processes in the cell." In: *Trends in cell biology* 9.2 (1999), pp. 48–52.
- [156] M Elangovan, RN Day, and A Periasamy. "Nanosecond fluorescence resonance energy transfer-fluorescence lifetime imaging microscopy to localize the protein interactions in a single living cell." In: *Journal of microscopy* 205.1 (2002), pp. 3–14.
- [157] Ingo Gregor and Matthias Patting. "Pattern-based linear unmixing for efficient and reliable analysis of multicomponent TCSPC data." In: *Advanced Photon Counting*. Springer, 2014, pp. 241–263.
- [158] Marek Liyanage, Allen Coleman, Stan du Manoir, Tim Veldman, Stephen McCormack, Robert B Dickson, Carolee Barlow, Anthony Wynshaw-Boris, Siegfried Janz, Johannes Wienberg, et al. "Multicolour spectral karyotyping of mouse chromosomes." In: *Nature genetics* 14.3 (1996), pp. 312–315.
- [159] Hiromichi Tsurui, Hiroyuki Nishimura, Susumu Hattori, Sachiko Hirose, Ko Okumura, and Toshikazu Shirai. "Seven-color fluorescence imaging of tissue samples based on Fourier spectroscopy and singular value decomposition." In: *Journal of Histochemistry & Cytochemistry* 48.5 (2000), pp. 653–662.
- [160] Alex M Valm, Sarah Cohen, Wesley R Legant, Justin Melunis, Uri Hershberg, Eric Wait, Andrew R Cohen, Michael W Davidson, Eric Betzig, and Jennifer Lippincott-Schwartz. "Applying systems-level spectral imaging and analysis to reveal the organelle interactome." In: *Nature* 546.7656 (2017), pp. 162–167.
- [161] Tao Huang, Carey Phelps, Jing Wang, Li-Jung Lin, Amy Bittel, Zubenelgenubi Scott, Steven Jacques, Summer L Gibbs, Joe W Gray, and Xiaolin Nan. "Simultaneous multicolor single-molecule tracking with single-laser excitation via spectral imaging." In: *Biophysical journal* 114.2 (2018), pp. 301–310.
- [162] Philip Tinnefeld, Dirk-Peter Herten, and Markus Sauer. "Photophysical dynamics of single molecules studied by spectrally-resolved fluorescence lifetime imaging microscopy (SFLIM)." In: *The Journal of Physical Chemistry A* 105.34 (2001), pp. 7989–8003.
- [163] Thomas Niehörster, Anna Löschberger, Ingo Gregor, Benedikt Krämer, Hans-Jürgen Rahn, Matthias Patting, Felix Koberling, Jörg Enderlein, and Markus Sauer. "Multi-target spectrally resolved fluorescence lifetime imaging microscopy." In: *Nature methods* 13.3 (2016), pp. 257–262.
- [164] Kristin S Großmayer, Stefan Geissbuehler, Adrien Descloux, Tomas Lukes, Marcel Leutenegger, Aleksandra Radenovic, and Theo Lasser. "Spectral cross-cumulants for multicolor super-resolved SOFI imaging." In: *Nature Communications* 11.1 (2020), pp. 1–8.

- [165] Bassam Hajj, Jan Wisniewski, Mohamed El Beheiry, Jiji Chen, Andrey Revyakin, Carl Wu, and Maxime Dahan. "Whole-cell, multicolor superresolution imaging using volumetric multifocus microscopy." In: *Proceedings of the National Academy of Sciences* 111.49 (2014), pp. 17480–17485.
- [166] ZL Wang. *Transmission electron microscopy of shape-controlled nanocrystals and their assemblies*. 2000.
- [167] Mats GL Gustafsson. "Nonlinear structured-illumination microscopy: wide-field fluorescence imaging with theoretically unlimited resolution." In: *Proceedings of the National Academy of Sciences* 102.37 (2005), pp. 13081–13086.
- [168] Rainer Heintzmann and Thomas Huser. "Super-resolution structured illumination microscopy." In: *Chemical reviews* 117.23 (2017), pp. 13890–13908.
- [169] Andrew G York, Panagiotis Chandris, Damian Dalle Nogare, Jeffrey Head, Peter Wawrzusin, Robert S Fischer, Ajay Chitnis, and Hari Shroff. "Instant super-resolution imaging in live cells and embryos via analog image processing." In: *Nature methods* 10.11 (2013), p. 1122.
- [170] Grégoire PJ Laporte, Nicolino Stasio, Colin JR Sheppard, and Demetri Psaltis. "Resolution enhancement in nonlinear scanning microscopy through post-detection digital computation." In: *Optica* 1.6 (2014), pp. 455–460.
- [171] Ron Tenne, Uri Rossman, Batel Rephael, Yonatan Israel, Alexander Krupinski-Ptaszek, Radek Lapkiewicz, Yaron Silberberg, and Dan Oron. "Super-resolution enhancement by quantum image scanning microscopy." In: *Nature Photonics* 13.2 (2019), pp. 116–122.
- [172] Ingo Gregor, Martin Spiecker, Roman Petrovsky, Jörg Großhans, Robert Ros, and Jörg Enderlein. "Rapid nonlinear image scanning microscopy." In: *Nature methods* 14.11 (2017), p. 1087.
- [173] Marco Castello, Giorgio Tortarolo, Mauro Buttafava, Takahiro Deguchi, Federica Villa, Sami Koho, Luca Pesce, Michele Oneto, Simone Pelicci, Luca Lanzañó, et al. "A robust and versatile platform for image scanning microscopy enabling super-resolution FLIM." In: *Nature methods* 16.2 (2019), pp. 175–178.
- [174] Dan Dan, Ming Lei, Baoli Yao, Wen Wang, Martin Winterhalder, Andreas Zumbusch, Yujiao Qi, Liang Xia, Shaohui Yan, Yanlong Yang, et al. "DMD-based LED-illumination super-resolution and optical sectioning microscopy." In: *Scientific reports* 3 (2013), p. 1116.
- [175] Jia Qian, Ming Lei, Dan Dan, Baoli Yao, Xing Zhou, Yanlong Yang, Shaohui Yan, Junwei Min, and Xianghua Yu. "Full-color structured illumination optical sectioning microscopy." In: *Scientific reports* 5 (2015), p. 14513.
- [176] Steve Wolter, Anna Löschberger, Thorge Holm, Sarah Aufmkolk, Marie-Christine Dabauvalle, Sebastian Van De Linde, and Markus Sauer. "rapid STORM: accurate, fast open-source software for localization microscopy." In: *Nature methods* 9.11 (2012), pp. 1040–1041.

- [177] Alexey I Chizhik, Jan Rother, Ingo Gregor, Andreas Janshoff, and Jörg Enderlein. "Metal-induced energy transfer for live cell nanoscopy." In: *Nature Photonics* 8.2 (2014), pp. 124–127.
- [178] Narain Karedla, Alexey I Chizhik, Ingo Gregor, Anna M Chizhik, Olaf Schulz, and Jörg Enderlein. "Single-Molecule Metal-Induced Energy Transfer (smMIET): Resolving Nanometer Distances at the Single-Molecule Level." In: *ChemPhysChem* 15.4 (2014), pp. 705–711.
- [179] *pgFocus-wiki*. <http://big.umassmed.edu/wiki/index.php/PgFocus>.
- [180] Arindam Ghosh, Akshita Sharma, Alexey I Chizhik, Sebastian Isbaner, Daja Ruhlandt, Roman Tsukanov, Ingo Gregor, Narain Karedla, and Jörg Enderlein. "Graphene-based metal-induced energy transfer for sub-nanometre optical localization." In: *Nature Photonics* 13.12 (2019), pp. 860–865.

ACKNOWLEDGMENTS

I acknowledge the financial support from H2020 European Union Funding for Research and Innovation (ITN Be-Optical project) as well as SFB 889 (DFG).

This thesis is a summary of more than four years of adventure with a bunch of bittersweet memories. I doubt I can forget the moments in my first journey from Iran to Germany when I wrote “new opportunity, new challenge” while looking from the window to a gray sky. Without the help and support of many people, this thesis would not have been possible.

I wish to express my deepest gratitude to my supervisor, Professor *Jörg Endelein*, for his trust and unfailing help and support. I admire him for his deep comprehension, uncountable ideas for troubleshooting, and preciseness.

I want to pay my special regards to Doctor *Ingo Gregor* for his consult and assistance, particularly in the first stages of my work. The one who gently pushed me forward to pave the way of deep comprehension with his precious advice. I highly appreciate his consideration and time for proof-reading my thesis.

I am truly grateful to all our group members, in particular: *Arindam Ghosh*, *Steffen Mühle*, *Sebastian Isbaner*, and *Narain Karedla*, for their remarkable and continued presence in ups and downs throughout my Ph.D. I am going to miss our high voltage table soccer matches as well as our home cinemas. My friends, without a doubt, I would have been alone and overflowed in my lab without your delightful companion. Our friendship became a priceless asset to me.

Special thanks to *Thomas Geiling*, *Dieter Hille*, *Markus Schoenekess* in the computer, mechanics, and electronics workshops to provide a high-speed and dedicated work.

I appreciate the unstoppable efforts of the coordinators in IMPRS-PBCS office: *Frauke Bergmann* and *Antje Erdmann*. Without their generous support, neither a well-organized event nor paperwork would have been doable.

I would like to thank Professor *Kishan Dholakia*, the head of the optical manipulation group at the University of St Andrews, for giving me the opportunity to do my first secondment. I thank Doctor *Jonathan Nylk*, Doctor *Mingzhou Chen*, and Doctor *Zhengyi Yang*, for their guidance and input during my internship at the University of St Andrews.

It was a great pleasure to have Professor *Fred Wouters* and Professor *Andreas Neef* in my thesis advisory committee as well. I thank both of you for devoting your precious time as well as your input during our meetings. I highly appreciate Professor *Timo Betz*, Professor *Holger Stark*, and Professor *Alexander Egner* for accepting to be members

of my thesis examination board.

I am cordially grateful to my wife, *Samira*, for her patience, companionship, and unconditional love throughout my Ph.D.

Last but far from least, I am indebted to my family, particularly my mother *Ezzat* and my late father *Mohsen* for their love and sacrifice. I cannot put my gratitude in words. May *GOD* protect and bless you.

CURRICULUM VITAE

SOHEIL MOJIRI

Date of birth: 27.05.1989

Place of birth: Isfahan

Nationality: Iranian

ACADEMICAL BACKGROUND

2016 – <i>present</i>	Doctoral Dissertation Thesis: <i>Advances in enhanced multi-plane 3D imaging and image scanning microscopy</i> Georg-August University of Göttingen, Göttingen
2012 – 2015	Master of Science in Photonics Thesis: <i>Generation and investigation of circular Airy beams</i> Institute for Advanced Studies in Basic Sciences (IASBS), Zanzan
2007 – 2012	Bachelor of Science in Physics Thesis: <i>Investigation of quantum dot lasers design</i> University of Isfahan, Isfahan
2003 – 2007	High school Mathematics and Physics Ebne Sina high school, Isfahan

MEMBERSHIPS, TEAM WORK EXPERIENCES AND EXECUTIVE ACTIVITIES

2019	<p>Secondment as a visiting Ph.D. in PicoQuant Company, Berlin</p> <ul style="list-style-type: none"> - Hands on time-resolved microscopy including FLIM and FCS - Course on company related topics: innovation management, product development, and marketing
2017	<p>Secondment as a visiting Ph.D. in Optical Manipulation Group, School of Physics and Astronomy, University of St Andrews, St Andrews</p> <ul style="list-style-type: none"> - Experimental implementation and characterization of two photon Airy light sheet microscope - Experimental generation and propagation analysis of circular Airy beams
2015-2016	<p>Research assistant in Optical Integrated Circuits Lab, Laser and Electro-optics Industry of Isfahan, Iran</p> <ul style="list-style-type: none"> - Generation and Characterization of waveguides using proton exchange and titanium diffusion methods
2013-2015	<p>Research assistant in Femtosecond Laser Lab, Laser and Electro-optics Industry of Isfahan</p> <ul style="list-style-type: none"> - Generation and simulation of Mathieu-Gauss beams using phase only patterns and liquid crystal display for coupling in optical tweezers.
2012-2015	<p>Member of Non-diffracting Beams Research Group, Light Bullets and Non-Diffracting Optical Beams Lab, IASBS, Zanjan</p> <ul style="list-style-type: none"> - Generation and propagation of circular Airy beams through scattering media - Generation of Bessel, doughnut, 1D, 2D, and circular Airy beams using phase only patterns and liquid crystal display

Computer skills	Matlab, Office, Imagej, Illustrator, Latex, Familiar with Oslo
Language	Persian (maternal), English (full proficieny), Greman (basic)
Hobbies	Woodworking with thin plywood Persian calligraphy Books (History, Novel) Sport (Gymnastics, Volleyball)

PUBLICATIONS

2020	Soheil Mojiri , Sebastian Isbaner, Steffen Mühle, Hongje Jang, Albert J. Bae, Ingo Gregor, Azam Gholami, and Jörg Enderlein Three dimensional beating dynamics of <i>Chlamydomonas</i> flagella, bioRxiv, (link)
2015	Soheil Mojiri , Mostafa Aakhte, Daryoush Abdollahpour Experimental investigation of abruptly autofocusing beams propagation in scattering medium, The Annual Physics Conference of Iran 2015, Ferdosi University, Mashhad, Iran, (link)

PRESENTATIONS

Talks

2018	Biophysics by the Sea, Alcudia <i>Multi-plane phase-contrast (MPC) imaging</i> 24th International Workshop on Single Molecule Spectroscopy and Super-resolution Microscopy in the Life Sciences, PicoQuant, Berlin <i>Three dimensional localization of single molecules using sm-MIET and defocused imaging</i>
2017	Biophysics by the Sea, Alcudia <i>Advances in biomedical imaging: multi-plane 3D SOFI and two photon Airy light-sheet imaging</i> Optical Manipulation Group, School of Physics and Astronomy, University of St Andrews, St Andrews <i>Circular Airy beams and multi-plane 3D SOFI</i>

Posters

2020	Third Infinity Conference, Göttingen <i>Out of plane bending components in Chlamydomonas flagella observed with multi-plane phase-contrast imaging</i>
2017	23th International Workshop on Single Molecule Spectroscopy and Super-resolution Microscopy, PicoQuant, Berlin <i>Multi-plane 3D super-resolution optical fluctuation imaging (SOFI)</i> International Light-sheet Fluorescence Microscopy (LSFM) Conference, NUS, Singapore <i>Multi-plane 3D super-resolution optical fluctuation imaging (SOFI)</i>

TEACHING

2018	Tutor for Practical course on ND:YAG laser with frequency doubling Göttingen University Tutor for Experimental Physics II: Electromagnetism Göttingen University
2017	Tutor for Practical course on ND:YAG laser with frequency doubling Göttingen University

OTHER PROFESSIONAL ACTIVITIES

2018	Co-organizer of 'Quantitative Bio Imaging (QBI)', Göttingen
2017	Co-organizer of Science Museum 'Seeing life through a new light', Manchester Museum of Science and Industry, Manchester